Into the Rainbow: Kinetics of the Bacterial Reaction Center Using Broadband Two-Dimensional Electronic Spectroscopy

by

Riley Sechrist

A dissertation submitted in partial fulfillment
of the requirements for the degree of
Doctor of Philosophy
(Physics)
in the University of Michigan
2021

Doctoral Committee:

Professor Jennifer P. Ogilvie, Chair
Professor Steven T. Cundiff
Professor Eitan Geva
Professor Roseanne J. Sension

Riley Sechrist

rsechris@umich.edu

ORCID iD: 0000-0002-3796-8467

Acknowledgements

There's a common myth that a doctoral thesis is primarily an independent project. This is, of course, absurd. Between the beginning and the end of this project, there were a thousand times when I might have stopped. A thousand times when I might have just decided to give up, or to spend my time and energy elsewhere. But I have been overwhelmingly lucky to be surrounded by friends, family, coworkers, and mentors who were always there to provide support and encouragement when I needed it. Completing a Ph.D. is not a matter of intelligence or will or strength of character. At least not for me. It's a matter of building and sustaining a community that will hold you close through the rough times and give you the strength and courage to push your own limits. Of course, it is impossible to recognize everyone who supported me along the way and made this thesis possible. I'll just do the best I can here.

With that in mind, I'd like to start by thanking the people who were most closely involved with the intellectual and technical work of this project. My PI, Jennifer Ogilvie, has been an incredibly supportive and understanding mentor and advisor. She has worked with me to find ways of keeping my research on track through every obstacle while consistently prioritizing my well-being over arbitrary measures of progress. Dr. Yin Song and Dr. Orko Konar contributed significantly to large portions of the work discussed in this thesis and taught me much of what I know about optics and spectroscopy. I'd especially like to thank former group members Dr. Veronica Policht and Dr. Libby Maret for welcoming me into the group, teaching me experimental techniques, and explaining concepts I was too nervous to ask anyone else

about. Push-up club will forever be one of my favorite grad school memories! The current Ogilvie group is an incredibly resilient and brilliant bunch who not only discussed many of the results in this thesis with me, but also kept the lab running through a pandemic. I'm particularly grateful to Rhiannon and Ariba – your friendship has meant so much to me, and your excellent research skills repeatedly inspire me to push myself to become a better scientist.

I'd like to thank my parents for valuing and supporting my education throughout my entire life, and for providing me with the stable support I needed to complete a PhD. Thanks to my brother Joey and my friend Brey for always being just a text or a phone call away, even if we haven't talked in months. My extended family has also been incredibly supportive of my goals, even if pursuing those goals meant missing family events sometimes. It means so much to have cousins, aunts, and uncles who support my goals and want me to succeed, and of course, thanks to Grandma Claire for bringing us all together over and over again. I also want to thank my Grandpa Dick who was always supportive of my education. I know you'd be proud of me. My Aunt Laura and Uncle Scott have also been so invested in my life – I owe much of my success in undergrad to their support, encouragement, and reminders to take breaks and have fun.

Speaking of undergrad, I want to thank my professors and classmates at Denison University who gave me the confidence and skills to study physics in graduate school.

I also want to thank the people who made the space where I did so much of my PhD possible. The University of Michigan is based on land stewarded by Niswi Ishkodewan Anishinaabeg: The Three Fires People who are Ojibwe, Odawa, and Potawatomi along with their neighbors the Seneca, Delaware, Shawnee, and Wyandot nations. I hope that the

University of Michigan will honor this history while working toward a future in which the University accepts accountability for the harm caused by settler colonialism and continually works to reduce ongoing harm. The physics building where I did much of my work is maintained by the labor of janitorial staff, several of whom have made the extra effort of providing encouragement on days when I was working late. I'd also like to thank Paul Thurmond and the Physical Plant Staff for maintaining the building and lab environments. The physics department itself would almost certainly not function at all without the effort of the administrative staff, and in particular, the wonderful people in the Student Services Office who have helped me resolve so many issues throughout my time in the program.

A number of formal organizations and groups have had an incredible impact on my ability to succeed throughout graduate school. Of these, I'd first like to thank the Graduate Employees' Organization (GEO), which is responsible not only for the free healthcare package and pay raises that enable many graduate students to complete their degrees, but also for the more specific and sometimes even lifesaving benefits of coverage of many transition-related medical expenses and mental healthcare copay caps. On a more personal level, the organizers of GEO are lovely people who are genuinely invested in their work both as graduate employees and as community organizers. I am so lucky to have connected with and learned from several of them.

Next, I'd like to thank the Society for Women in Physics (SWIP) which was one of the first groups I connected with at Michigan and in many ways enabled the many friendships and connections that supported me through my PhD. SWIP gave me the space to develop valuable skills in a supportive and friendly environment, and I am so grateful to everyone who has

contributed (or continues to contribute) to building that community. The last official group I'd like to recognize is Graduates out in STEM (GoSTEM). It has been absolutely incredible to see this group grow from a few dedicated grad students into a vibrant and active community over the course of my PhD. In the past year, this group has been the source of so much kindness and joy in my life, not to mention inspiration for my thesis title. I want to thank all the former and current graduate students who have made groups like this possible, and who have worked, either through intentional activism or by simply taking up space, to make the University of Michigan and the physics department more welcoming places so that I could safely and comfortably work on my research here.

An incredible number of friends have supported me in my PhD work, and I can only thank a fraction of them here. Thanks to the many and overlapping friend groups who helped me relax and recharge: my Star Trek friends, my D&D friends, my queer friends, my board game and movie night friends. A special thanks to the current and former denizens of Physics House for stepping up in a big way when I really needed it. Thanks to Ansel, Chelsea, Meryl, Jessie, Nicole, Vidhya, and Ceren for being such unique and wonderful people, and for connecting with me in the ways that work best for us. Thanks to Chanese for keeping me focused on my thesis on Monday afternoons. Thanks to Anh for the beautiful photos and kind words, and for seeing me as the person I want to be. Thanks to my cat, Bernadette, for keeping me rigorously on schedule and reminding me (loudly) to take breaks. And finally, in no particular order, thanks to Enrique, Morgan, and Liz for their unrelenting support and validation. To Enrique for being my pandemic survival buddy and for being there literally every day to help me through various crises. To Morgan for seeing me for who I am at every moment and for teaching me critical

survival skills like how to dye my hair. To Liz, for sticking with me through so much, even the hard parts, and for coaxing me through countless pomodoros even though you didn't have to. This thesis wouldn't exist without you.

Table of Contents

List of Figures

List of Appendices

Abstract

Photosynthesis is a process by which light is converted to chemical energy, and which is responsible for nearly all life on Earth. A more complete understanding of the mechanisms behind photosynthesis, particularly the initial energy conversion steps, could inform the design of more efficient future photovoltaic devices. The bacterial reaction center (BRC) has been an important model system for understanding the mechanism of photosynthetic charge separation due to its well characterized structure and the distinct absorption features of its constituent pigments. Two-dimensional electronic spectroscopy (2DES) has recently emerged as a valuable tool for studying the electronic structure and dynamics of photosynthetic systems. 2DES can reveal electronic coupling and the ultrafast processes of energy transfer and charge separation. In this thesis, two-color and broadband 2DES are used to probe the electronic structure of the BRC, allowing us to identify the Q_X exciton locations and characterize the charge separated intermediates across a wide spectral range spanning the Q_Y and Q_X transitions.

The spectral features and kinetics of the BRC at 77K are discussed qualitatively based on the results of a two-color 2DES experiment using a near-IR pump covering the BRC Q_Y transitions and visible probe covering the Q_X band. Strong excited state absorption (ESA) features present in the Q_X region were fit and subtracted out to reveal the underlying ground state bleach (GSB) structure. A rich network of cross peaks in the resulting spectra indicates the presence of a common ground state between the Q_X and Q_Y transitions. It also strengthens our previous assignment of the energy of the upper exciton state of the special pair which has been

highly controversial due to its weak transition strength. This work demonstrates that two-color 2DES can be used to provide valuable information about the electronic structure and coupling of the BRC by accessing regions in which different degrees of spectral overlap provide complementary information to one-color studies.

A more quantitative analysis is performed using broadband 2DES data that extends the detection axis from the near-IR into the visible regime, covering both the Q_Y and Q_X bands. The multiexcitation global kinetic analysis was adapted from earlier work by Niedringhaus et al. that compares models of charge separation in the Q_Y band.[1] In this scheme, a kinetic model is constrained by prior knowledge of the system and used to fit both the 2DES and linear absorption spectra simultaneously. The spectral signature of the charge separated state is calculated by linear least squares and relevant physical parameters such as exciton energies are extracted from the optimized fit. This analysis was extended to model broadband data covering both the Q_X and Q_Y bands, including the ESA contributions which had previously been neglected. Using this approach, the spectral signatures of the charge separation intermediates were characterized over the broadband detection axis. The major features of the 2DES data are replicated, although some discrepancies between the fit and measured data persist.

Future work will consider additional approaches to account for excited state absorption and inhomogeneity to better reproduce the observed 2DES spectral features. The broadband 2DES data presented in this thesis, as well as future polarization-dependent 2DES studies, will provide an extensive data set for simulations that can test and refine exciton and charge separation models of the BRC.

Chapter 1 Introduction

Widespread policy change is necessary to adequately address the global threat of climate change. However, technological advancements that improve the efficiency of clean energy sources may lower the barrier to moving away from fossil fuels as a society. Over billions of years of evolution, photosynthesis has become a highly effective process for converting light to usable energy.[2] One of the key steps in this process, which involves the creation of a charge separated state, occurs with near unity quantum efficiency. A more complete understanding of this charge separation process, as well as photosynthesis in general, could inform future artificial light harvesting technology.[3]–[5] In this context, it is important to develop a complete understanding of the mechanisms involved in photosynthesis. However, photosynthesis is a complex process in which the primary energy conversion steps occur on a timescale of femtoseconds to picoseconds. In order to study such a system, it is therefore necessary to use a technique that can access ultrafast timescales. Ultrafast spectroscopy is an ideal tool for this task, as it can be used to track energy conversion over these extremely fast timescales. This thesis will discuss an investigation of the photosynthetic bacterial reaction center using two-color two-dimensional electronic spectroscopy on ultrafast timescales.

Section 1.1 Introduction to photosynthesis

Photosynthesis is a process by which energy from light is converted into chemical energy, which can be stored and used to fuel the various reactions that are necessary for

maintaining life. Because photosynthesis, and other related processes such as the carbon and nitrogen cycles, are central to the life cycle of plants, people have likely sought to understand this process in some form for nearly as long as plants have been cultivated for food. In fact, as early as several thousand years ago, indigenous people in Central and South America discovered the benefits of growing maize, beans, and corn together in an arrangement that relies on aspects of photosynthesis and nitrogen fixation to maximize the success of all three crops.[6] However, it was not until the seventeenth century that western scientists began to isolate and quantify the various components of photosynthesis. Over the course of several centuries, and through the contributions of many individuals, the scientific community developed the overall balanced equation for oxygenic photosynthesis that we use today [3]:

$$6\,CO_2 + 6\,H_2O \;\rightarrow\; C_6H_{12}O_6 + 6\,O_2 \qquad (1.1)$$

Although this is the equation for photosynthesis that many people are familiar with, photosynthetic organisms are very diverse, encompassing many species of plants, algae, and bacteria that evolved in a wide range of environments. Although most plants produce oxygen as a byproduct of photosynthesis, a variety of organisms perform photosynthesis in environments that are devoid of oxygen and produce other products. In this case, other molecules, such as H_2S, replace oxygen as the reducing agent. More generally, then, we can write:

$$CO_2 + 2\,H_2A \;\rightarrow\; CH_2O + 2A + H_2O \qquad (1.2)$$

This equation gives a general picture of the overall scheme of photosynthesis, but glosses over the complex multi-step mechanisms involved. In fact, many pigment-protein complexes are necessary to collect solar energy and funnel it to a Reaction Center (RC). To

achieve this, antenna complexes are arranged around the RCs (Figure 1.1a). High energy light absorbed by antennas can be passed "downhill" in energy among the various pigments within a single complex, and between different types of antennas, ultimately reaching the RC (Figure 1.1b). In this way, solar energy spanning a broad spectral range is passed to the RC where it can be used to produce a charge separated state to drive the later chemical stages of photosynthesis.[7]

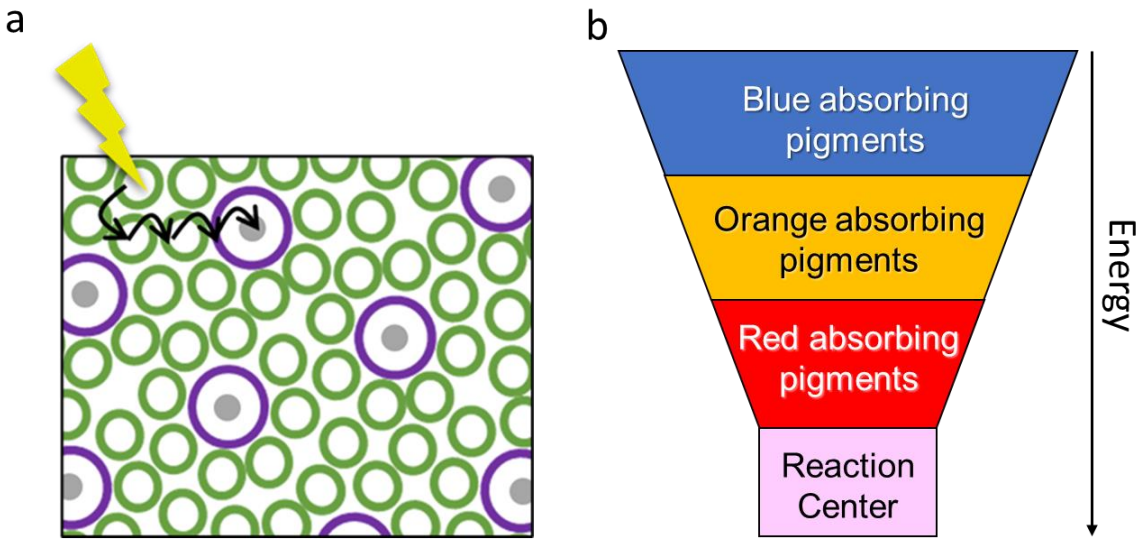

Figure 1.1 a) A cartoon showing the spatial arrangement of antenna complexes in purple bacteria. The small green circles are light harvesting II complexes, and the large purple circles are light harvesting I complexes which contain the RCs, indicated by the grey. The lightning bold and arrows signify the initial excitation and funneling of energy to a central RC. Figure adapted from [8]. b) Energy diagram showing how energy is passed from antenna complexes to RC. Figure adapted from [3].

The pigments involved in this process depend on the species in question. Many plants and algae contain chlorophyll while some bacteria, such as purple bacteria, contain bacteriochlorophyll instead. Both pigments consist of a chlorin ring with a metal center and an acetyl group. While the overall structure is similar, bacteriochlorophyll has a different acetyl group and less conjugation of the chlorin ring compared to chlorophyll, changing the absorption

properties and symmetry of the molecule. Even among purple bacteria, different species contain different pigments, which changes their absorption properties. *Blastochloris viridis*, the first purple bacteria species to have a high-resolution X-ray structure characterized, contains the pigments bacteriochlorophyll *b* and bacteriopheophytin *b*. Bacteriopheophytin is similar to bacteriochlorophyll, but lacks the metal center. Another commonly studied purple bacteria species, *Rhodobacter sphaeroides*, contains bacteriochlorophyll *a* and bacteriopheophytin *a*. Bacteriochlorophyll *a* is very similar to bacteriochlorophyll *b*, but it lacks a double bond on the outside of the bacteriochlorin ring and therefore absorbs at higher energies. *Rhodobacter capsulatus* is the species used in the experiments described in this thesis due to the availability of the desired M250V mutant, which is discussed further below. Rhodobacter capsulatus contains bacteriochlorophyll *a* and bacteriopheophytin *a* and is spectroscopically very similar to *Rhodobacter sphaeroides*. The structural differences of these various pigments tune them to absorb at different frequencies, making them useful to different organisms depending on the light quality of their environment. This also has the benefit of making them identifiable in spectroscopy experiments. These pigments and their spectral properties play a critical role in the investigation of energy transfer and charge separation in photosynthetic antenna and reaction centers.[3]

Section 1.2 Structure of the Bacterial Reaction Center

The reaction center that we will discuss in this thesis is the Bacterial Reaction Center (BRC) found in purple bacteria. The BRC contains several pigments held in place by a protein scaffolding. The pigments are arranged in a nearly symmetric structure consisting of two branches, labelled A and B (Figure 1.2). The two branches are joined by a pair of strongly

coupled bacteriochlorophyll molecules, called the “special pair” (P). On each side of the special pair is another bacteriochlorophyll *a* (B) molecule followed by a bacteriopheophytin (H). A quinone (Q) is positioned at the end of each branch.[9]

These pigments give rise to absorption features in several spectral regimes. In the lowest energy Q_Y band, the contributions from the P, B, and H pigments are clearly visible as three distinct peaks. The bacteriopheophytin absorbs at a higher frequency than the bacteriochlorophyll, and the strong coupling of the special pair produces a strong, red-shifted absorption peak. The contributions from the bacteriochlorophylls in the Q_X band are overlapping, but the bacteriopheophytin appears as a distinct feature (Figure 1.2b). At even higher energies, another transition gives rise to the Soret band. These transitions can be understood by considering the Gouterman four-orbital model for porphyrins.[10], [11] In this model, porphyrins have an a_{1u} HOMO orbital, an a_{2u} HOMO orbital, and two e_g LUMO orbitals. Mixing these orbitals results in two ^1E_u orbitals, one at higher energy corresponding that gives rise to the Soret band, and one at lower energy that gives rise to the Q_X and Q_Y bands. For the

pigments in the BRC, which are less symmetric than porphyrins, the Q_X and Q_Y transitions are split as well.

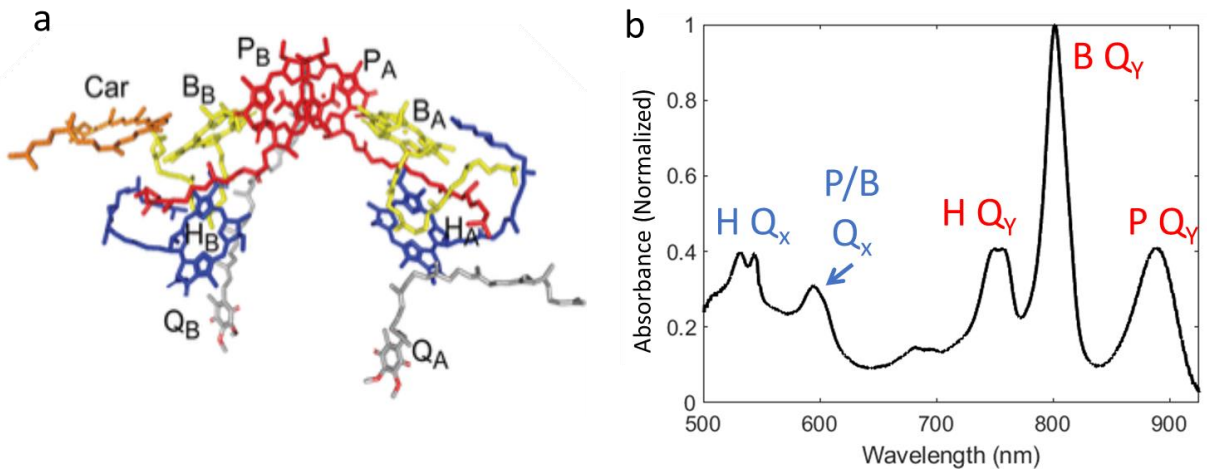

Figure 1.2 a) Pigments in the BRC. The surrounding protein structure has been omitted. Based on the structure by [9]. Figure from [12]. b) Linear absorption spectrum of the BRC at 77K with peaks labelled according to the pigments that contribute most strongly.

The energy levels of each of these molecules could be represented in the site basis, in which each pigment has its own ground and excited states that are influenced by the local protein environment. However, in the case of strong coupling between pigments, such as for the two bacteriochlorophyll *a* molecules that make up the special pair, the energy levels can be more appropriately described by the eigenstates of the coupled system. These eigenstates are referred to as molecular excitons. In the excitonic basis, the electronic excitations are delocalized over the contributing pigments. In 2001, Jordanides and coworkers quantified the contributions of each of the BRC pigments to the states of the excitonic basis.[13] They estimated the electronic coupling of the special pair pigments to be 395 cm^{-1} at room temperature (or 49.0 in units of meV), significantly stronger than the coupling between any of the other pigments. This strong coupling produces the upper (P_+) and lower (P_-) excitonic states, which consist of linear combinations of excitations of the P_A and P_B pigments. The relative

orientation of the special pair transition dipoles results in significant dipole strength for P_-, while P_+ is weak and has therefore been historically difficult to detect.[1], [13]–[17] Technically, the full energetic system of the BRC can be viewed in the excitonic basis with all the pigments coupled to varying degrees and the strongest coupling between the pigments of the special pair. The relevance of this representation depends on the coupling strength of the pigments and the sensitivity of the measurement to this coupling.

Section 1.3 Spectroscopic studies of the BRC

The BRC has been the subject of many spectroscopic studies over the years. A very small sample of that work can be found in the references here.[17]–[19] The focus on the BRC is in large part due to its low spectral congestion compared to similar reaction centers from other organisms. Contributions from each pigment can be easily discerned by the three well-separated peaks in the near-IR regime. In other systems, such as photosystem II, these contributions are overlapping and much more difficult to distinguish.[20] Additionally, crystal structures for the BRC from several species have long been available, providing a clear picture of the physical arrangement of the pigments and proteins which aids in interpreting spectroscopic data.[9], [21], [22] These factors have made the BRC a model system for understanding the energy conversion process in reaction centers.

In complement to spectroscopic studies, a variety of interesting mutants of the BRC have been developed and have served to provide both additional tools for spectroscopy experiments as well as independent insights into energy conversion in BRCs. For example, an interesting feature of the wild type BRC is that despite the near symmetry of the A and B branches, charge separation occurs nearly exclusively along the A branch. However, several

mutants have been developed that allow charge separation to proceed along the B branch to varying degrees, with a recent result showing 90% transfer along the B branch.[23] This work has revealed insight into the mechanism of charge separation as well as produced an interesting new sample for further experiments. In this thesis, we use the M250V mutant of *Rhodobacter capsulatus*, in which charge separation occurs along the A branch as in the wild type, but lacks the A branch quinone.[24] This prevents formation of the final charge separated state, $P^+Q_A^-$, which would otherwise interfere with experiments using our 1 kHz repetition rate regenerative amplifier.

This previous work to understand energy conversion in the BRC has contributed to the development of a picture of the kinetic pathway of energy conversion in the BRC (Figure 1.3). The overall scheme begins with an excitation of the special pair, which then generates a charge separated state with positive charge localized on the special pair and negative charge on the A branch bacteriopheophytin. The electron transfer then continues along the A branch, forming $P^+Q_A^-$, which can exist for over a millisecond. The charge is then transferred to the B branch quinone, where it forms the relatively stable $P^+Q_B^-$ state that persists until a second excitation event results in a second reduction of Q_B. The B branch quinone then separates from the BRC and initiates the next step of the electron transport chain so that the photosynthetic reaction

can proceed.[3], [25]

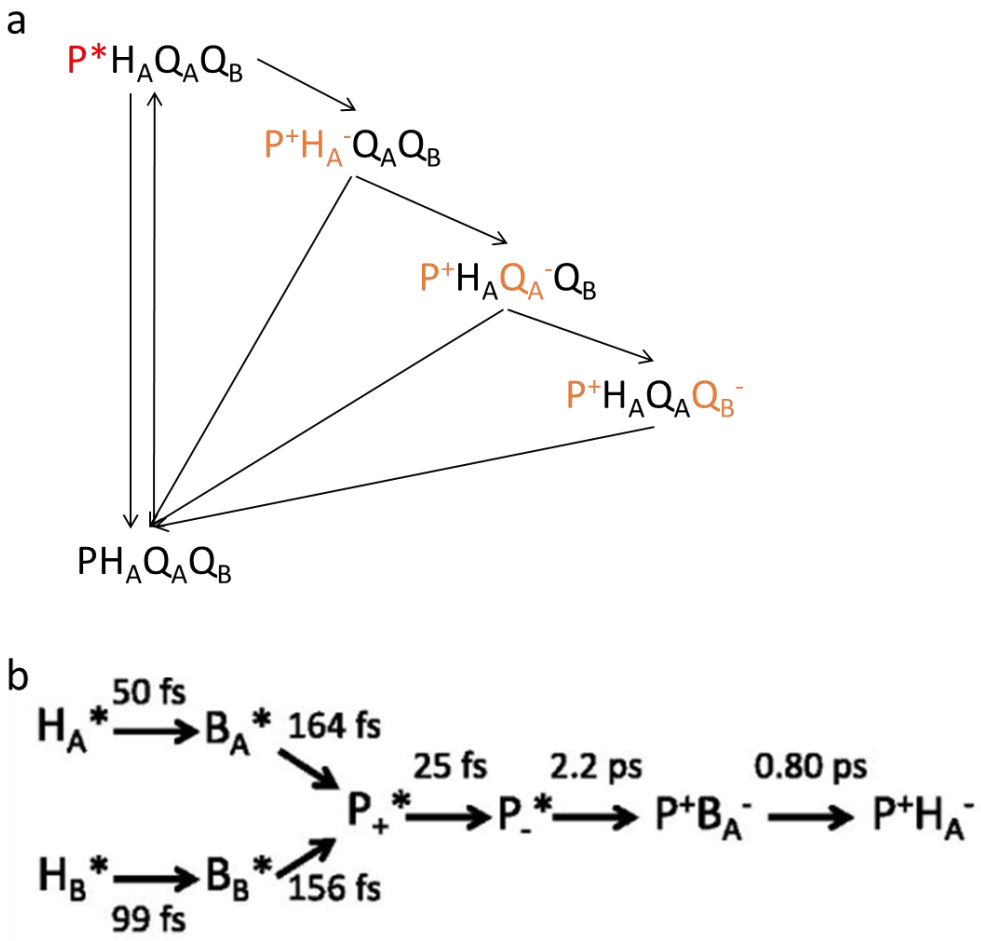

Figure 1.3 a) Overall scheme of charge separation in the BRC. b) Kinetic scheme determined in [1].

Several conflicting models have been suggested to describe how the $P^+H_A^-$ charge separated state forms.[26]–[30] By simultaneous global fitting of the 2DES data and linear absorption spectrum of the BRC in the Q_Y region, we were able to test models of the kinetics of charge separation in the BRC.[1] We found that a single charge separation pathway was sufficient and that the data was well described by the kinetic scheme shown in Figure 1.3b. In this model, when the BRC is excited on either the bacteriopheophytin or the bacteriochlorophyll of the A or B branch, the excitation is rapidly transferred to the lower P

exciton of the special pair. The subsequent charge separation occurs in a step-wise process along the A branch as negative charge is first transferred from the special pair to B_A to form the $P^+B_A^-$ intermediate on the order of picoseconds. From there, the $P^+H_A^-$ state forms in less than a picosecond. In this thesis, expand the spectroscopic window beyond the Q_Y region to investigate the kinetics of primary charge separation and obtain the broadband spectral signatures of the charge separation intermediates.

Chapter 2 Two-Dimensional Electronic Spectroscopy Theory

Section 2.1 Calculating the third order response function

The theoretical formalism most commonly used to describe nonlinear spectroscopy was developed by Mukamel.[31] Since then, several other useful references have further described and summarized that approach.[32], [33] Here, we will discuss the basics of this formalism as a way of introducing 2D spectroscopy and informing the interpretation of 2D spectra. Anyone seeking additional background information or a more complete understanding of the mathematical nuances involved in this discussion is encouraged to consult the references noted above.

In order to connect our theoretical discussion to a physical interpretation of 2D spectra, we ultimately want to calculate a third order response function. We will begin with several formulations of the linear polarization which are hopefully familiar to the reader. In terms of the susceptibility in the frequency domain, the polarization created within a material upon interacting with electric field $E(\omega)$ is given by

$$P(\omega) = \epsilon\, \chi(\omega)\, E(\omega) \tag{2.1}$$

where, ϵ is the vacuum permittivity and $\chi(\omega)$ is the susceptibility. The polarization can also be written in terms of the response function in the time domain

$$P(t) = \int_0^\infty d\tau\, R(\tau) E(t-\tau) \tag{2.2}$$

In terms of the density matrix,

$$P(t) = Tr\big(\mu\rho(t)\big) = \langle\mu\rho(t)\rangle \tag{2.3}$$

Here, the brackets indicate the expectation value, μ is the dipole operator, and ρ(t) is the density operator in the time domain. Nonlinear spectroscopy explores higher order interactions between the external electric field and the system. Within the approximation that the external fields are sufficiently weak, a perturbative approach is appropriate, wherein the polarization is expanded to higher orders in the electric field:

$$P = \epsilon_0\big(\chi^{(1)} \cdot E + \chi^{(2)} \cdot E \cdot E + \chi^{(3)} \cdot E \cdot E \cdot E + \cdots\big) \tag{2.4}$$

where $\chi^{(2)}$ and $\chi^{(3)}$ are the respective second and third order susceptibilities and are tensor quantities. Here we omit the vector and tensor notation for simplicity.

Two-dimensional spectroscopy probes the third order response function via the generation of the third order polarization arising from the interaction of the system with three time-ordered fields. In the time domain, this polarization can be expressed as

$$P^{(3)}(t) = \int_0^\infty d\tau_3 \int_0^\infty d\tau_2 \int_0^\infty d\tau_1 \, R^{(3)}(\tau_3, \tau_2, \tau_1) E_1(t - \tau_3 - \tau_2 - \tau_1) E_2(t - \tau_3 - \tau_2) E_3(t - \tau_3) \tag{2.5}$$

Looking at the third order polarization, we can see how it describes time-ordered interactions with the electric field, as shown on the time axis in Figure 2.1.

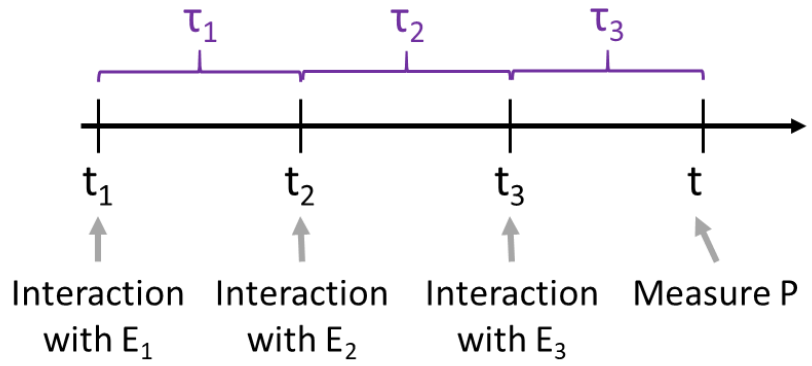

Figure 2.1 A timeline showing the time intervals and pulse interactions described mathematically.

In the density matrix formalism, we can write the polarization instead as

$$P^{(3)}(t) = Tr\left(\mu\rho^{(3)}\right) \tag{2.6}$$

Here, $\rho^{(3)}$ is the third order expansion of the density matrix, which corresponds to three interactions with the external electromagnetic field. The field can be treated classically.

$$V(t) = -\vec{\mu}\cdot\vec{E} \tag{2.7}$$

So, a single field interaction can be represented as:

$$\rho^{(1)} = \frac{-i}{\hbar^3}\int_{-\infty}^{t} dt_1\,[V(t_1),\rho_0] \tag{2.8}$$

where ρ_0 describes the initial state of the system. Upon three sequential field interactions the third order expansion of the density matrix is given by

$$\rho^{(3)} = \frac{-i}{\hbar^3}\int_{-\infty}^{t} dt_3\int_{-\infty}^{t_3} dt_2\int_{-\infty}^{t_2} dt_1\left[V(t_3),[V(t_2),[V(t_1),\rho_0]]\right] \tag{2.9}$$

We can then write out the third order polarization as

$$P^{(3)}(t) = Tr\left(\mu\frac{-i}{\hbar^3}\int_{-\infty}^{t} dt_3\int_{-\infty}^{t_3} dt_2\int_{-\infty}^{t_2} dt_1\left[V(t_3),[V(t_2),[V(t_1),\rho_0]]\right]\right) \tag{2.10}$$

Making several rearrangements and substitutions, we can rewrite equation 10 in a similar form to equation 5. We apply the change of variables $t_1 = t - \tau_1 - \tau_2 - \tau_3,\ t_2 = t - \tau_2 - \tau_3$, and $t_3 = t - \tau_3$ and enforce the time ordering $0 \leq t_1 \leq t_2 \leq t_3$. When the dust settles, the result is:

$$P^{(3)}(t) = \frac{-i}{\hbar}\int_0^\infty d\tau_3 \int_0^\infty d\tau_2 \int_0^\infty d\tau_1\, E_3\,(t-\tau_3)E_2(t-\tau_3-\tau_2)E_1(t-\tau_3-\tau_2-\tau_1)$$
$$Tr\left(\left[\left[\left[\mu(\tau_3+\tau_2+\tau_1),\mu(\tau_2+\tau_1)\right],\mu(\tau_1)\right],\mu(0)\right]\rho_0\right) \quad (2.11)$$

Now, we can compare equations 5 and 10 to write out the third order response function:

$$R^{(3)}(\tau_1,\tau_2,\tau_3) = \frac{-i}{\hbar^3}\theta(\tau_1)\theta(\tau_2)\theta(\tau_3)\,Tr\left(\left[\left[\left[\mu(\tau_3+\tau_2+\tau_1),\mu(\tau_2+\tau_1)\right],\mu(\tau_1)\right],\mu(0)\right]\rho_0\right) \quad (2.12)$$

where $\theta(\tau)$ is the Heaviside step function. This formulation of the response function can be used to understand the diagrammatic representation of signals in two-dimensional spectroscopy data, as described in the next section.

Section 2.2 Double sided Feynman diagrams

We can use the response function and polarization from the previous section to describe the interactions that lead to signals in two-dimensional spectra. A useful tool for making this connection is double sided Feynman diagrams. These diagrams are visual representations of the correlation functions from the third order response function that can be interpreted as showing the various energetic pathways enabled by the three light-matter interactions involved in producing two dimensional spectra. They are also useful for keeping track of the phase and sign accumulated by the sequential interactions.

The response function contains a series of correlation functions that describe every possible series of interactions between the field and the system described by the density

matrix. It is useful to write out these correlation functions separately in terms of the intermediate states of the density matrix.

$$R_1 = \sum_{a,b,c,d} \langle \mu_{ad}(\tau_1+\tau_2+\tau_3)\mu_{dc}(\tau_1+\tau_2)\mu_{cb}(\tau_1)\mu_{ba}(0)\rho_0 \rangle$$

$$R_2 = \sum_{a,b,c,d} \langle \mu_{ad}(0)\mu_{dc}(\tau_1+\tau_2)\mu_{cb}(\tau_1+\tau_2+\tau_3)\mu_{ba}(\tau_1)\rho_0 \rangle$$

$$R_3 = \sum_{a,b,c,d} \langle \mu_{ad}(0)\mu_{dc}(\tau_1)\mu_{cb}(\tau_1+\tau_2+\tau_3)\mu_{ba}(\tau_1+\tau_2)\rho_0 \rangle$$

$$R_4 = \sum_{a,b,c,d} \langle \mu_{ad}(\tau_1)\mu_{dc}(\tau_1+\tau_2)\mu_{cb}(\tau_1+\tau_2+\tau_3)\mu_{ba}(0)\rho_0 \rangle \quad (2.13)$$

The sum over a, b, c, and d represents a sum over the possible intermediate states. The subscripts on the dipole operators indicate the intermediate states they are associated with, so μ_{ba} will act on the bra side of the density matrix by transforming it from state a to state b. Note that there are actually eight different correlation functions, but half of them are complex conjugates of the others, so we omit them here. Each of these terms can be rearranged such that the dipole operators interact sequentially on either the bra or ket side of the density matrix. As an example, let's consider a simpler case from the 2nd order response function.

$$\langle \mu_{ac}(\tau_1+\tau_2)\mu_{cb}(\tau_1)\mu_{ba}(0)\rho_0 \rangle$$

$$\left\langle U^\dagger(\tau_1)U^\dagger(\tau_2)\mu_{ac}U(\tau_2)U(\tau_1)U^\dagger(\tau_1)\mu_{cb}U(\tau_1)\mu_{ba}\rho_0 \right\rangle$$

$$\left\langle \mu_{ac}U(\tau_2)\mu_{cb}U(\tau_1)\mu_{ba}\rho_0 U^\dagger(\tau_1)U^\dagger(\tau_2) \right\rangle \quad (2.14)$$

Where U is the time evolution operator, which has the effect of evolving the system in time, and U^+ is its inverse. In the last step we have used the fact that the trace in invariant for cyclic permutation to arrange the term so that all the U^+terms are on the right hand side and all the U terms are on the left hand side. Now, we can clearly see that each density operator will

interact with the ket of the density matrix, and are thus considered ket interactions for the purpose of constructing Feynman diagrams. An example diagram for a third order interaction is shown in Figure 2.2. Time increases moving up the vertical lines of the Feynman diagram, with the arrows indicating interactions with the field. The state of the system is often shown in the density matrix representation in the center. Ket interactions are represented by an arrow on the left side of the Feynman diagram and bra interactions are represented by an arrow on the right side of the Feynman diagram. Conventionally, the final trace is necessarily a ket interaction and can be interpretated as the measurement of the system. Arrows pointing to the left add a phase of $\exp(-i\boldsymbol{k}\cdot\boldsymbol{r}+i\omega t)$ while arrows pointing to the right add a phase of $\exp(+i\boldsymbol{k}\cdot\boldsymbol{r}-i\omega t)$. Arrows on either side pointing toward the center will move the system to a higher state while arrows pointing away from the center move the system to a lower state. Each diagram will contribute a signal with a sign $(-1)^n$ where n is the number of bra interactions. The resulting diagrams can be grouped according to their phase. Those with the phase matching condition $\boldsymbol{k}_2-\boldsymbol{k}_1+\boldsymbol{k}_3$ are referred to as rephasing diagrams while those with the phase matching condition $\boldsymbol{k}_1-\boldsymbol{k}_2+\boldsymbol{k}_3$ are referred to as non-rephasing diagrams. These different phase-matching conditions give rise to distinct signals that contain different information about the system. By combining rephasing and non-rephasing signals, we can produce real absorptive spectra that are more physically intuitive than the separate rephasing or non-rephasing spectra.

Figure 2.2 shows Feynman diagrams that give rise to three types of signal typical in 2D spectra. The ground state bleach signal has a positive sign and is produced by the correlation function term:

$$\sum_{a,b,c,d} \langle \mu_{ad}(0)\mu_{dc}(\tau_1)\mu_{cb}(\tau_1+\tau_2+\tau_3)\mu_{ba}(\tau_1+\tau_2)\rho_0 \rangle \tag{2.15}$$

The excited state absorption signal has an overall negative sign and the excited state emission signal has an overall positive sign.

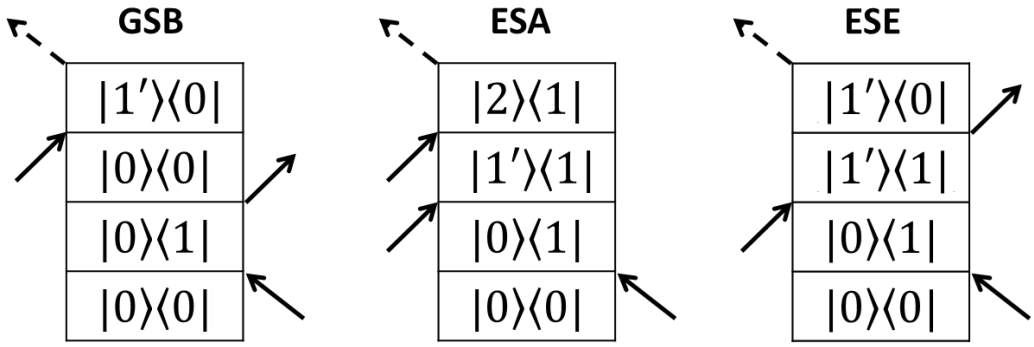

Figure 2.2 Double sided Feynman diagrams showing representative rephasing pathways giving rise to ground state bleach (left), excited state absorption (center) and excited state emission (right).

Section 2.3 Advantages of two-dimensional spectroscopy

The pulse sequence used to generate two-dimensional spectra is shown in Figure 2.3. Two pump pulses, delayed by a time t_1, interact with the sample, exciting the density matrix of section 2.2 into a population state. This state is then allowed to evolve during a waiting time T before interacting with a probe pulse which puts the system into a coherent superposition of states. The signal is retrieved after a time t_3. In practice, the final time delay t_3 is usually measured in the frequency domain by sending the signal to a spectrometer. The waiting time is typically controlled with a delay stage. The t_1 time delay is scanned over a series of values and then converted to the frequency domain by a Fourier transform. The resulting 2D spectra for a fixed waiting time can be plotted on both excitation frequency (corresponding to t_1) and detection frequency (corresponding to t_3) axes, as shown in Figure 2.3. Note that because the t_1 axis is produced by delaying the pump pulses relative to each other, the resolution of the

frequency axis is set by the maximum t_1 delay, while the time resolution is set by the width of the pump pulses in time. In this way, 2D measurements enable high frequency resolution without sacrificing the high time resolution afforded by ultrashort pulses.[34]

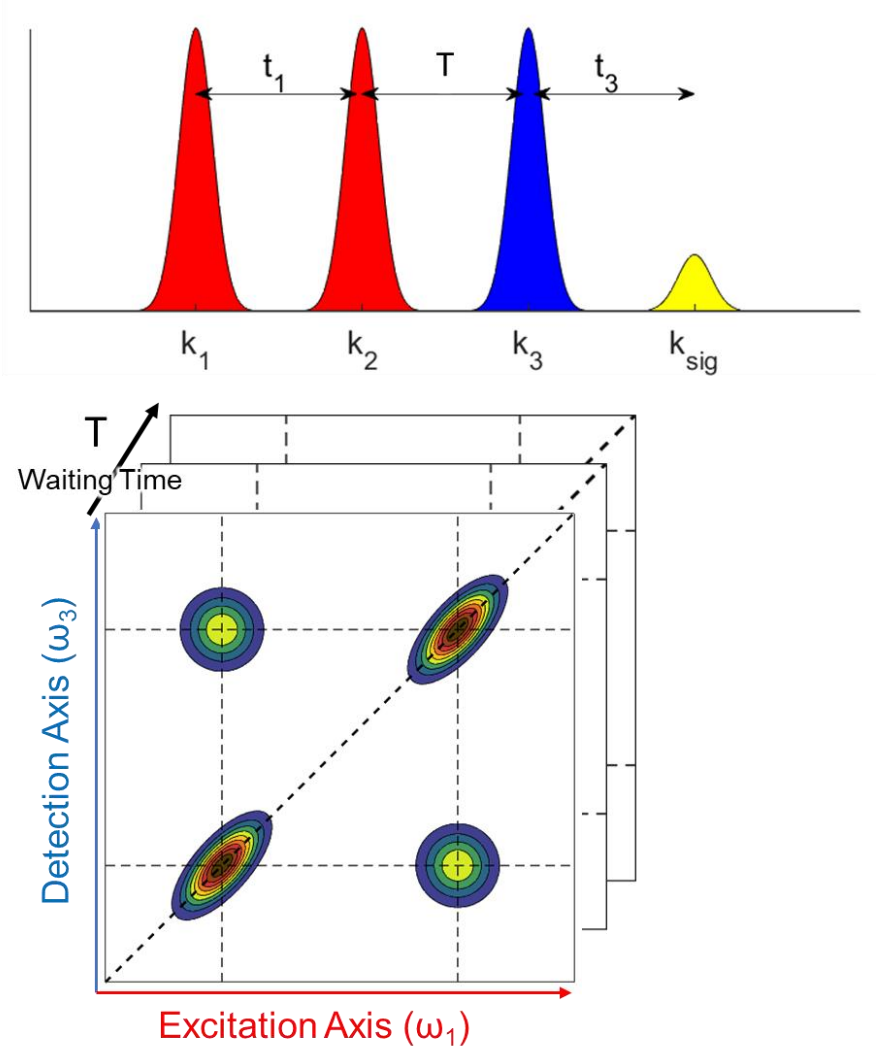

Figure 2.3 (top) The typical pulse sequence used for 2DES consists of two pump pulses (red) followed by a probe pulse (blue) which then generates the measured signal (yellow). (bottom) The fourier transform of the time delays t1 and t3 are used to create the excitation and detection axes for each T point.

This approach conveys several advantages. By spreading the signal across both the detection and excitation axes, we can distinguish features that appear at different detection or excitation frequencies that would be overlapped in linear spectroscopies. One clear example of

this is the ability to distinguish homogeneous and inhomogeneous broadening. Homogeneous broadening, which is due to the fundamental linewidth of a transition appears as broadening of the signal on the antidiagonal. Inhomogeneous broadening by contrast is due to the distribution of transition energies within the sample being measured, and appears as broadening along the diagonal (Figure 2.4). In photosynthetic systems, inhomogeneous broadening is common due to distinct local protein environments of chemically identical light-absorbing pigments. In linear spectroscopy these different sources of broadening are indistinguishable. In 2D spectra, at longer T times, as the individual systems within the sample experience different local environments, the diagonal elongation of the signal becomes less pronounced. This occurs because over time, a system that was excited at a given excitation frequency will experience fluctuations in its transition frequency and can therefore be measured at a range of different detection frequencies. On a macroscopic level, this appears as a rounding out of the 2D signal (Figure 2.4c).[34]–[36]

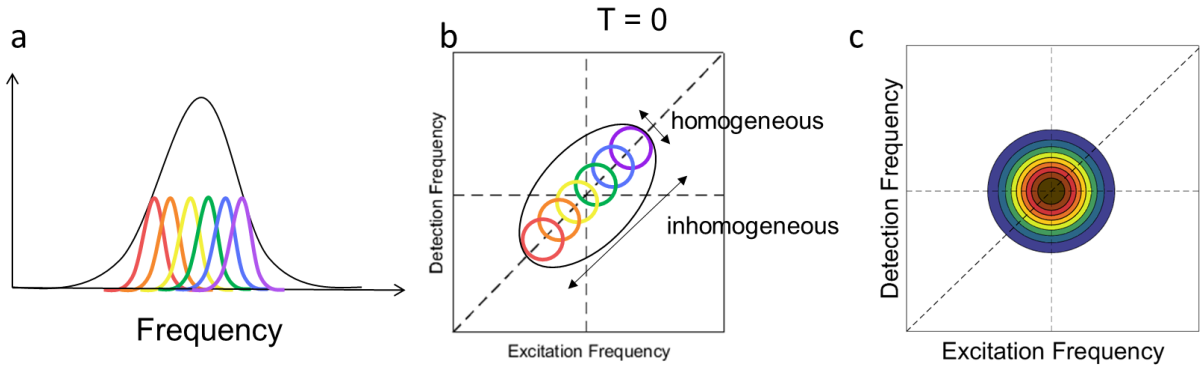

Figure 2.4 a) In linear spectroscopy, inhomogeneity appears as a single broad feature. b) In 2D spectroscopy, homogeneous broadening appears along the anti-diagonal while inhomogeneous broading appears along the diagonal. c) For T >> 0, spectral diffusion occurs and the elongation along the diagonal is lost.

Two-dimensional electronic spectra can provide further information about the electronic structure of the system being studied. Due to the presence of off-diagonal cross peaks, weakly and strongly coupled systems can be distinguished. Strongly coupled systems will have a shared ground state and therefore, excitation to either state at T = 0 will affect the population excited to the strongly coupled state. Therefore, off-diagonal cross peaks will appear even at T = 0. In weakly coupled systems, off-diagonal features can appear when population is transferred from one state to another, but because there is no shared ground state, this will only occur at later times (Figure 2.5). 2D spectra contain a wealth of information that is unavailable in linear spectra and can often be used to better understand complicated systems.

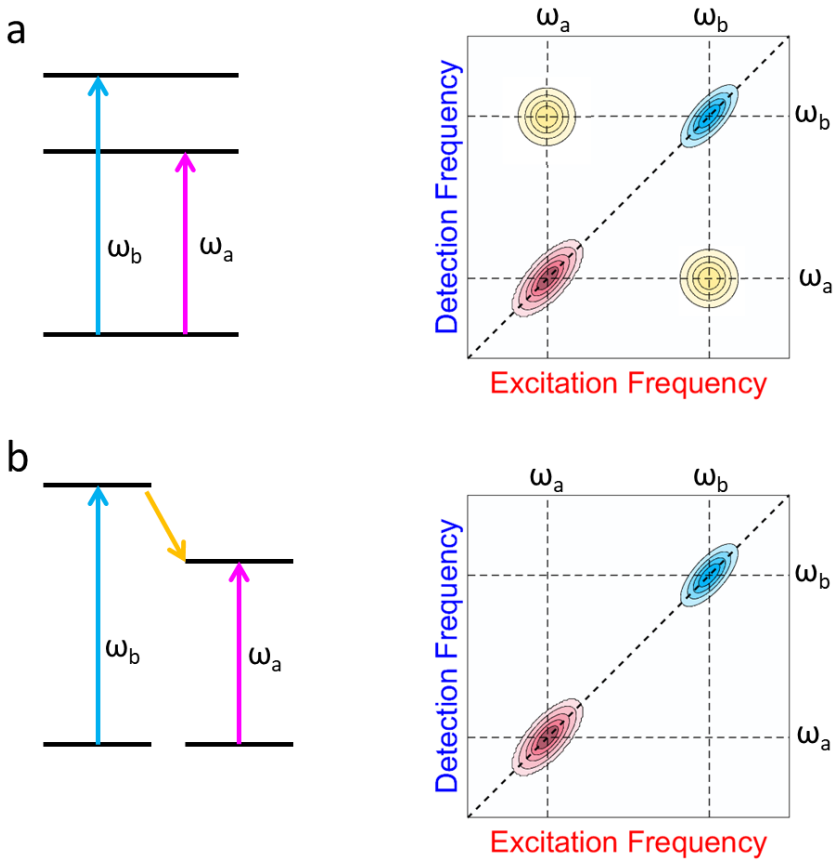

Figure 2.5 a) Transitions with a shared ground state give rise to off-diagonal features at T = 0. The shared ground state is caused by the strong coupling between the states, which perturbs their energies. This system can be considered in the excitonic basis in which the transitions are delocalized over the individual sites. b) Weakly coupled transitions only show off-diagonal features at T > 0 and can be represented intuitively in the site basis.

Section 2.4 Experimental Geometries and Phase Cycling

There are several different experimental geometries that can be used to collect 2D spectra.[36] One of the most widespread of these methods is the fully noncollinear BOXCARS geometry. In the BOXCARS geometry, the three pulses (two pump, one probe) propagate along different paths as if from three of the four corners of a box to intersect with the sample. The signal then propagates along a path toward the fourth corner according to the phase matching conditions. The signal is measured by heterodyning with a local oscillator that travels in the

same direction. However, this heterodyne detection introduces a phase ambiguity due to the unknown relative phase between the signal and the local oscillator. Solutions to this phase problem have been discussed previously in the literature.[37]

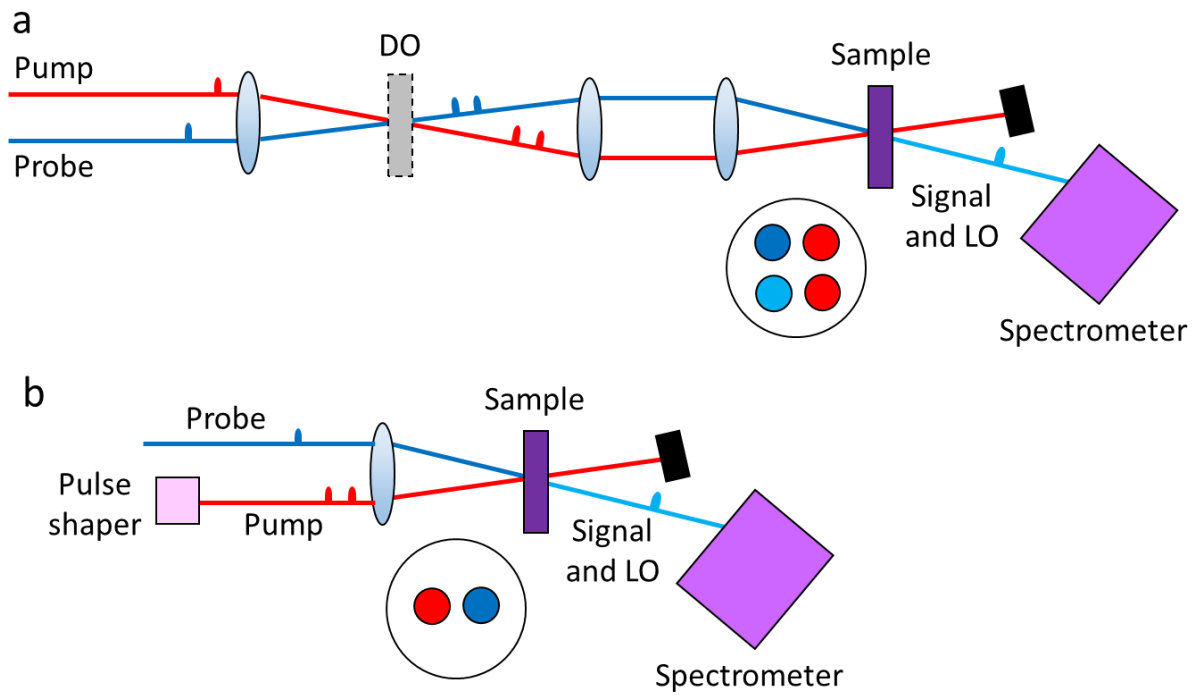

Figure 2.6 a) Diagram of BOXCARS geometry using a diffractive optic (DO) to generate the pulse pairs. b) Diagram of pump-probe geometry using a pulse shaper to generate the pulse pairs. The circle inset shows the arrangement of pulses just before the sample. The pump is red, probe is blue, and local oscillator (LO) is light blue.

The ordering of the pulses in the BOXCARS geometry gives rise to different phase matching conditions that in turn produce different spectra. These different phase matching conditions are represented in Figure 2.7 below. The rephasing and non-rephasing spectra can be combined to produce the physically intuitive real absorptive spectrum.

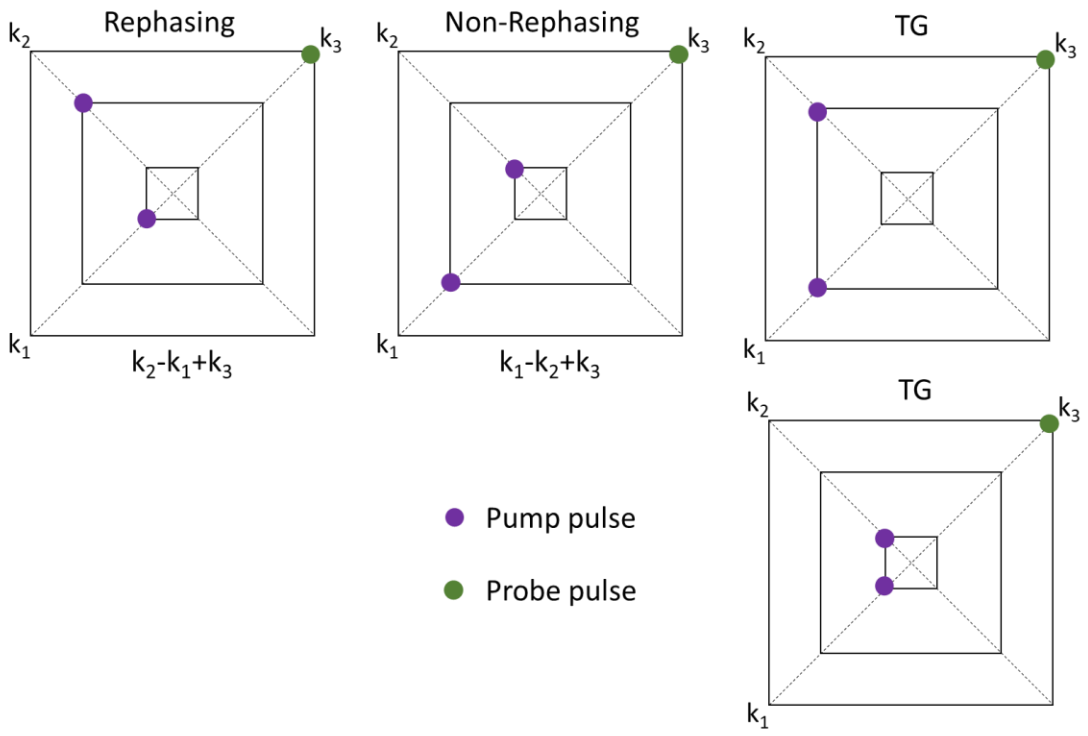

Figure 2.7 Diagrams showing the phase matching conditions for rephasing, non-rephasing, and transient grating signals for the BOXCARS geometry. Each corner of the square corresponds to a different k vector, and pulses on the same concentric square have the same phase. Pulses closest to the center interact with the sample first.

The BOXCARS geometry provides a number of advantages, perhaps most significantly, the ability to optimize the signal to noise due to the background free detection of the signal. However, for broadband and two-color experiments such as those discussed in this thesis, a partially colinear geometry such as the pump-probe geometry is significantly easier to align and implement.[37]–[41] In the pump-probe geometry, the pump pulses propagate along the same path and intersect with the probe pulse at the sample. The resulting signal then co-propagates with the probe which acts as a local oscillator (Figure 2.6b). As a result, the probe light must be attenuated to avoid saturating the camera. However, this implementation avoids the phasing ambiguity of the BOXCARS geometry entirely, and real absorptive spectra are collected directly. When a pulse shaper is used to produce a time-delayed pump-pulse pair, separate rephasing

and non-rephasing spectra can be produced by collecting data with the phase-cycling scheme described by Myers et al.[39] Pulse shapers enable a number of other techniques such as using the rotating frame to sample under the Nyquist frequency and subtracting background scatter from the data.[42]

Section 2.5 Two-color and broadband probe two-dimensional spectroscopy

Most 2DES experiments are performed using the same frequency light for the pump and probe pulses. However, two-color experiments, in which different frequency light is used for the pump and probe beam, are also possible, as is the use of a continuum probe.[43] By pumping and probing a sample in different spectral regimes, we can learn about transitions that are far apart in energy. Transitions between these states will appear as features in the 2D spectra that are far from the diagonal. This is especially useful for photosynthetic reaction centers, which have transitions in bands across the visible spectrum (Figure 2.8). For example, by pumping in the Q_X region of the spectrum and probing in the Q_Y region of the BRC, we can gain additional information about couplings and the dynamical processes such as energy transfer and charge separation. Because each pigment of the BRC contributes to transitions in multiple spectral regions, the information that we gain in two-color experiments will complement the results from one-color experiments. For example, in the Q_X band, the P and B peaks are overlapping, but the H_A and H_B transitions are well separated, while the reverse is true in the Q_Y band. By incorporating data from both of these spectral regions, we can create a more complete picture of the energetics of the BRC.

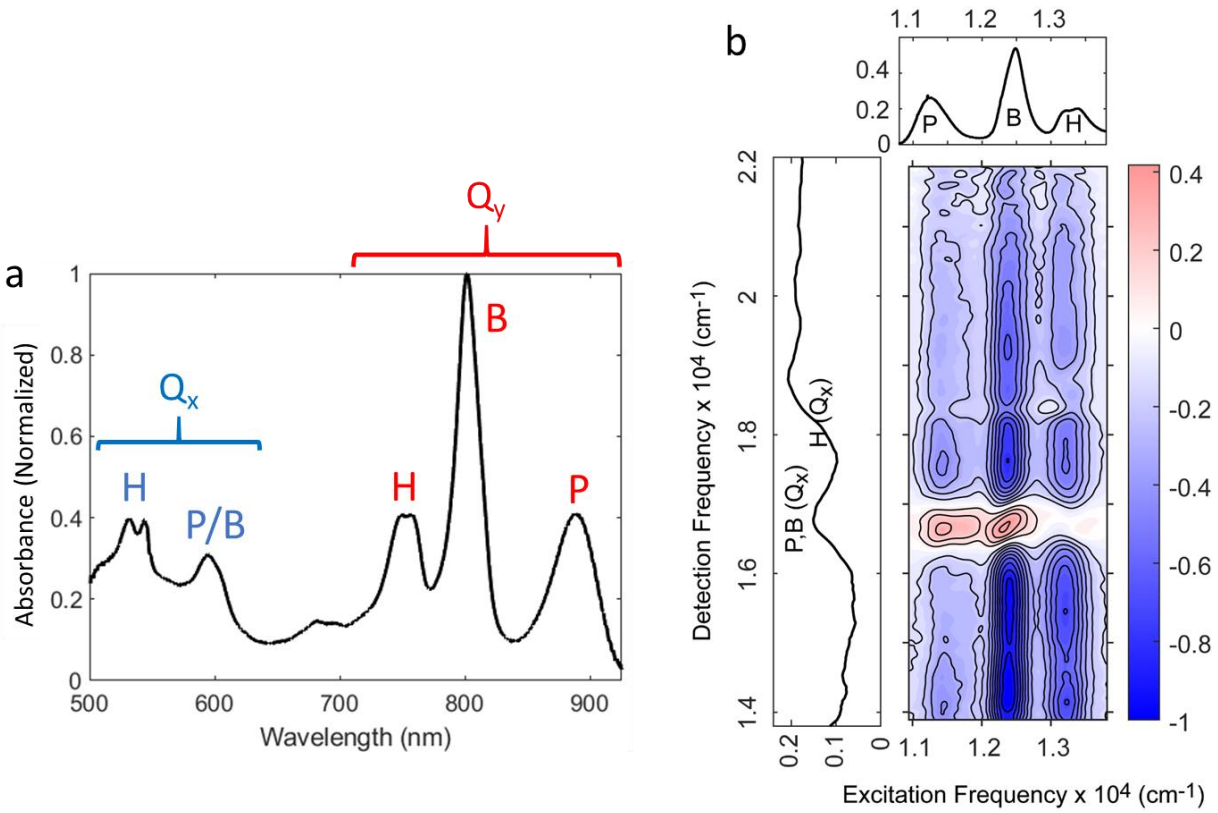

Figure 2.8 a) A linear absorption spectrum of the BRC, showing the Q_X and Q_Y bands in the visible and near-IR regimes. b) A two-color 2DES spectrum obtained by probing in the Q_Y and detecting in the Q_X of the BRC. The linear spectra at the top and left show the relevant region of the BRC linear absorption spectrum.

Previous experiments have taken advantage of two-color 2D to investigate a variety of different systems.[39], [44], [45] A conceptually related development in 2D spectroscopy has been the use of 2D electronic-vibrational spectroscopy (2DEV) and 2D vibrational electronic spectroscopy 2DVE. In contrast to two-color 2DES, 2DEV excites electronic transitions and probes vibrational transitions (and vice versa for 2DVE) whereas two-color 2DES pumps and probes electronic transitions. Many interesting studies have revealed the new information that can be accessed by investigating dramatically different transitions, both with 2DEV, 2DVE and other variations on pulse frequency combinations.[46]–[51]

Chapter 3 Experimental Implementation of Two-Dimensional Electronic Spectroscopy

Section 3.1 BRC Sample Preparation

The experiments described in this thesis were preformed on a mutant bacterial reaction center, W(M250)V, from *rhodobacter capsulatus,* which has a Trp in place of a Val at the M250 position. This mutation prevents the binding of Q_A, rendering the mutant unable to form the stable charge separated state $P^+Q_A^-$ which would persist for milliseconds before decaying to the ground state.[24] This mutation allows the BRC to return to the ground state between each excitation of our 1 kHz laser, thereby ensuring that each interaction with the laser pulse is independent. The W(M250)V BRC samples were grown by Philip D. Liable at Argonne National Laboratory and supplied to us by Christine Kirmaier, Dewey Holten, and Kaitlyn M. Faries at Washington University in St. Louis. The samples were stored in a 10 mM Tris buffer with 0.1% deriphat at a pH of 7.8. When they were not being used for experiments, the samples were stored at 77K in liquid nitrogen to prevent degradation.

Before each experiment, the BRC samples were treated to prevent the formation of long-lived states and reconcentrated as follows. Throughout the sample preparation procedure, samples were kept on ice to prevent damage. A complete step-by-step sample preparation procedure can be found in Appendix B.3 of the 2018 thesis by Policht [52]. Previous experiments performed by the Ogilvie lab required the BRC sample to have an OD of 0.3 at 800 nm with a 380 um pathlength. To achieve a similar OD in the higher energy Q_X band, we

increased the sample concentration by about 1.75 relative to the original procedure. For maximum clarity, the amounts and concentrations of all relevant reagents are compared in the table below. The other components of the sample preparation, including buffer, deriphat, and glycerol are used as described in the original procedure.

Table 3.1 Comparison of sample preparation procedure

	Policht 2018 [52]			Sechrist 2019		
Reagent	Volume (µL)	Concentration	Mol	Volume (µL)	Concentration	Mol
BRC in buffer	33.3	40 µM	1.3 nmol	61.3	38 µM	2.3 nmol
Sodium ascorbate in buffer	5	400 mM	2 µmol	8.75	400 mM	3.5 µmol
Terburtryn in ethanol	12.5	40 mM	0.5 nmol	21.9	40 mM	0.876 µmol

First the samples were thawed, then treated with excess sodium ascorbate. The purpose of the sodium ascorbate is to reduce the P_+ in the final charge separated state so that the BRC begins in the neutral ground state each time it is excited. The sample is then treated with terbutryn and allowed to sit for 10 minutes. The terbutryn prevents the formation of the long-lived charge separated state on the B branch, $P^+Q_B^-$, which has a small probability of forming following excitation of the BRC.[24] The sample is then centrifuged for 5 minutes at 10,000 g, which forms a pellet of unreacted terbutryn. The treated BRC is then decanted to remove the terbutryn pellet.

The BRC sample is then washed and reconcentrated by iteratively adding buffer and centrifuging the diluted sample. At the end of this process, the sample should have the desired final concentration. If the experiments are especially sensitive to scattering, an additional

filtration step can be added after the sample has been diluted with buffer and sodium ascorbate but before centrifuging. The sample can be pipetted into a syringe with a 1.2 µm pore size filter attached and slowly forced through the filter with the syringe plunger. This process is then repeated with a 0.2 µm pore size filter. This removes any aggregated BRC or other small particles. Beginning with a larger pore size ensures that the finer filter will not be clogged with large particles. The filtration step can be repeated before each wash step when the sample volume is at a maximum due to the added buffer. It should be noted that some sample will be lost during the syringe filtration, and therefore it may be necessary to begin the procedure with a higher volume of BRC stock solution. The syringe filtration was not used for the experiments described in this thesis.

The final volume of sample following these steps is typically between 15 and 25 µL. An equal volume of glycerol is added, bringing the sample volume up to 30 to 50 µL. A small volume of 3% deriphat in Tris buffer is added to bring the final concentration of deriphat in the sample to 0.1%. The deriphat is stored in a 3% solution in buffer, and may precipitate over time, so before adding deriphat to the sample, the 3% deriphat solution should be heated in warm water until any visible precipitate has dissolved.

Once all the reagents are added to the BRC sample vial, they should be mixed together thoroughly by flicking, shaking and rolling the vial manually. A final centrifuge step for 1 minute at 5000 g collects the sample at the bottom of the vial. Finally, 25 µL of the sample can be loaded into the sample cell which has a path length of 380 µm.

Section 3.2 Experimental Setup

We use two-color 2D experiments to investigate the effects of the initial charge separation on the BRC across the Q_X and Q_Y bands. By using a pump and probe in different frequency regimes, we can access new information about this complex photosynthetic system. This approach is enabled by the technical capabilities of the Laboratory for Ultrafast Multidimensional Optical Spectroscopy (LUMOS). The multispectral multidimensional spectrometer developed in LUMOS was described previously, and some of the most relevant figures and content from that paper will be replicated in this chapter.[53] In particular, we will focus exclusively on the pump-probe geometry and light sources in the visible and near-IR regimes.

The experimental configuration in LUMOS relies on two regenerative amplifiers seeded by a single Ti:Sapphire Mai Tai oscillator from Spectra Physics. One of the amplifiers is a Spitfire from Spectra Physics which generates 35 fs pulses with a power of 4.5 mJ at a 1 kHz repetition rate, centered at 800 nm. The other amplifier is a Solstice from Spectra Physics which generates 100 fs pulses with a power of 4.8 mJ at a 1 kHz repetition rate, centered at 800 nm. This setup allows us to access a wide range of time scales in experiments by using a pump and probe generated by different amplifiers, which can be delayed relative to each other. Long delays between the amplifiers can be controlled with a digital delay generator that offsets the amplifier pulses in steps of 12.5 ns. To access finer steps in the time delay, we use a physical translation stage to delay the seed to the Solstice with respect to the Spitfire amplifier. Using this approach, we can access timescales from femtoseconds to milliseconds. A similar dual amplifier design has been implemented in two other labs.[54]–[56]

The Solstice and Spitfire amplifiers in turn are used to generate a variety of pump and probe sources, as shown in figure 3.1.[53] The output from the Spitfire is split, with a portion of the power being directed to a nonlinear optical parametric amplifier (NOPA), which generates tunable visible pulses. Another portion is sent to a TOPAS White optical parametric amplifier from Light Conversion, and the output can be doubled to generate light in the UV regime. A small portion of the power from the Spitfire can also be used to produce a broadband white light continuum using a sapphire or calcium fluoride crystal. The Solstice is used to pump the TOPAS Twins, a commercial OPA that produces near-IR signal and idler beams. The signal beam generates the seed for a degenerate optical parametric amplifier (DOPA)[57] which is pumped by the second harmonic of 800 nm light from the Solstice, and produces a broadband spectrum in the visible and near-IR. The idler from the TOPAS Twins generates mid-IR light by difference frequency generation. Those light sources relevant to this thesis will be discussed in further

detail below.

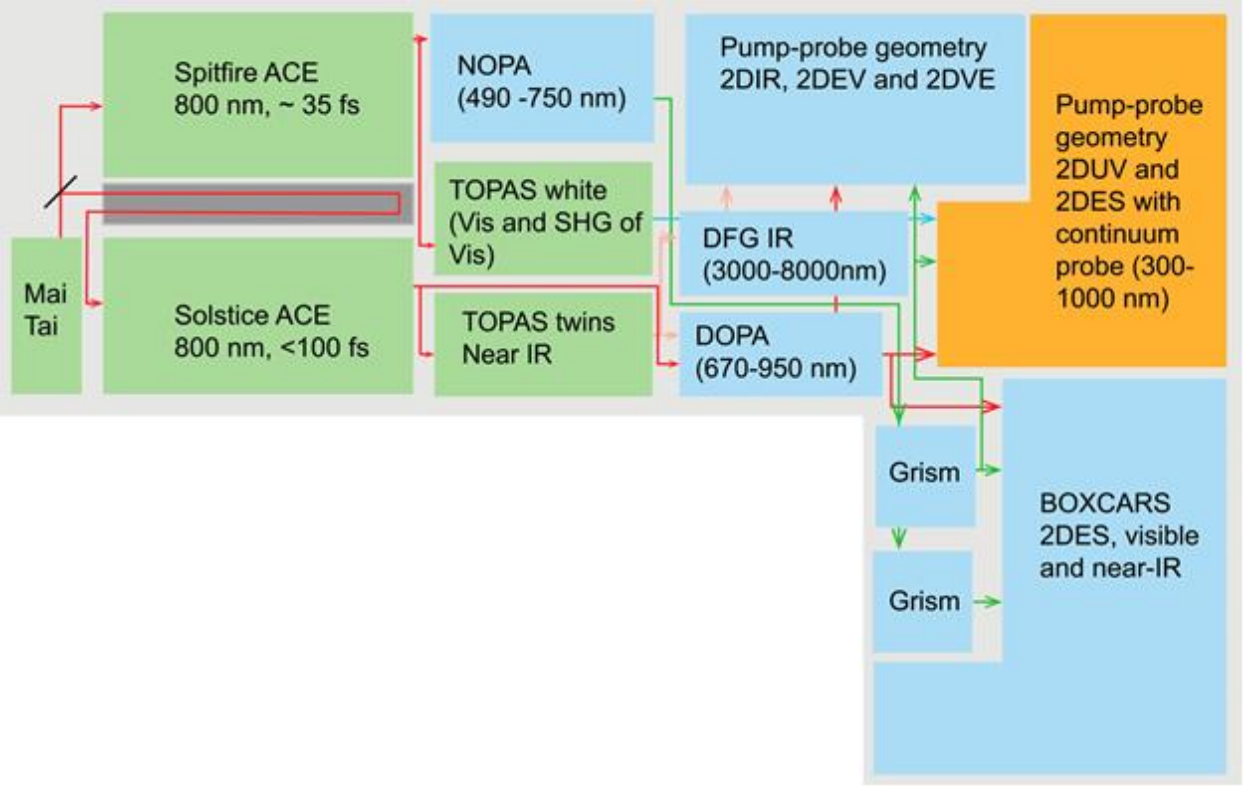

Figure 3.1 This figure is reproduced from Song et. al.[11] It shows the layout of the various light sources of the multispectral multidimensional spectrometer. Green regions indicate commercially purchased components, blue indicates previously developed home-built designs, and the orange region indicates techniques that are still being developed. The gray box between the Spitfire and Solstice shows the location of the long time delay line. The arrows show where the output of each light source is directed. Multiple arrows from a single light source indicate separate pump and probe beams.

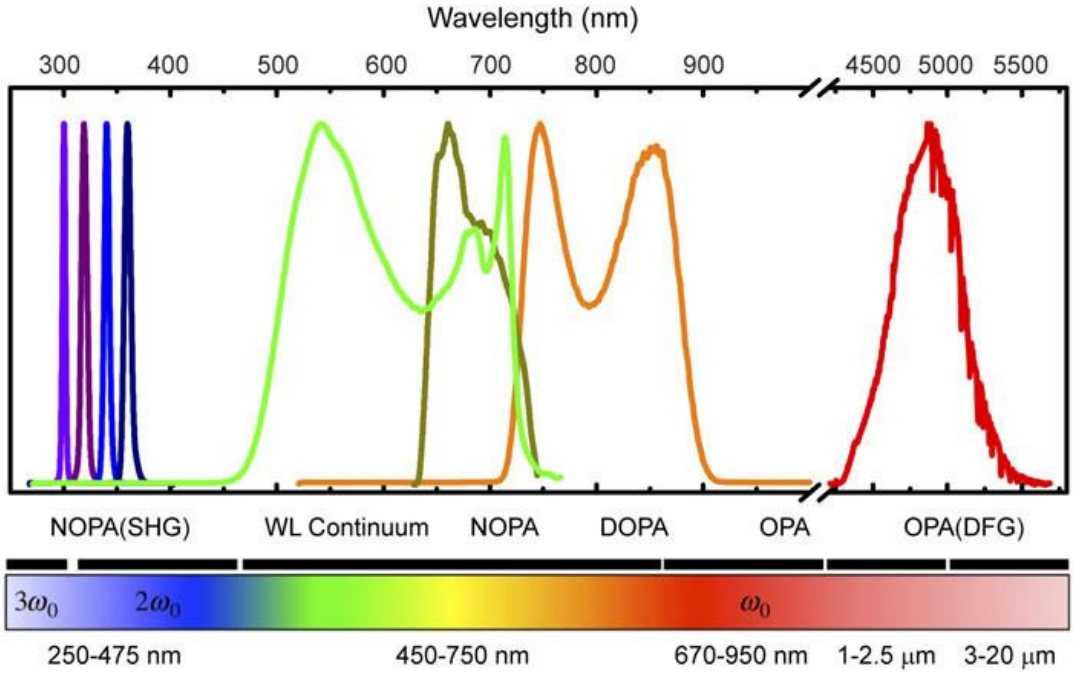

Figure 3.2 This figure is reproduced from Song et. al.[11] The spectra of each light source available in the multispectral multidimensional spectrometer is shown. Spectra span from the UV to the mid-IR.

The pump and probe beams are combined in the pump-probe geometry. There are several advantages to using the pump-probe geometry in these experiments. First, this geometry avoids the phasing problem that occurs in fully non-collinear geometries because the phase of the pump pulses can be fully controlled relative to each other, so absorptive spectra can be recorded directly without the need to determine an unknown phase.[35], [38], [39], [42], [58] Further, the pump-probe geometry is simply easier to align, especially when working with different frequency pump and probe beams due to the frequency dependence of dispersion and diffraction of the beams. Additionally, in the non-collinear geometry, the phase matching conditions become substantially more complicated for pump and probe light at different frequencies. The pump-probe geometry avoids these challenges altogether,[39], [58] and can readily use a continuum probe.[43]

A commercial pulse shaper, the Dazzler from Fastlite, is used to generate two collinear pump pulses with a well-defined time delay (t_1) between them. The Dazzler is an acousto-optic pulse shaper that can apply a different phase and amplitude modulation to each laser shot at 1 kHz rep rate, allowing it to produce a programmable train of pulses. Additionally, the Dazzler can be used to compress the pump pulses to a pulse width of ~10 fs using the SPEAR/CRT algorithm.[59] The results of a typical pulse compression detected using the second harmonic are shown in Figure 3.3.[12] Previous work by the Ogilvie group has demonstrated the capabilities of the Dazzler for implementing 2D electronic spectroscopy.[39], [43], [60] By independently controlling the phase of each pulse, we can take advantage of phase cycling to remove the pump background in the absorptive 2D spectra. Further, the Ogilvie group has demonstrated that pulse shaping can be used to isolate the rephasing and nonrephasing spectra, thereby supplying information that could not typically be obtained in the pump-probe geometry.[39]

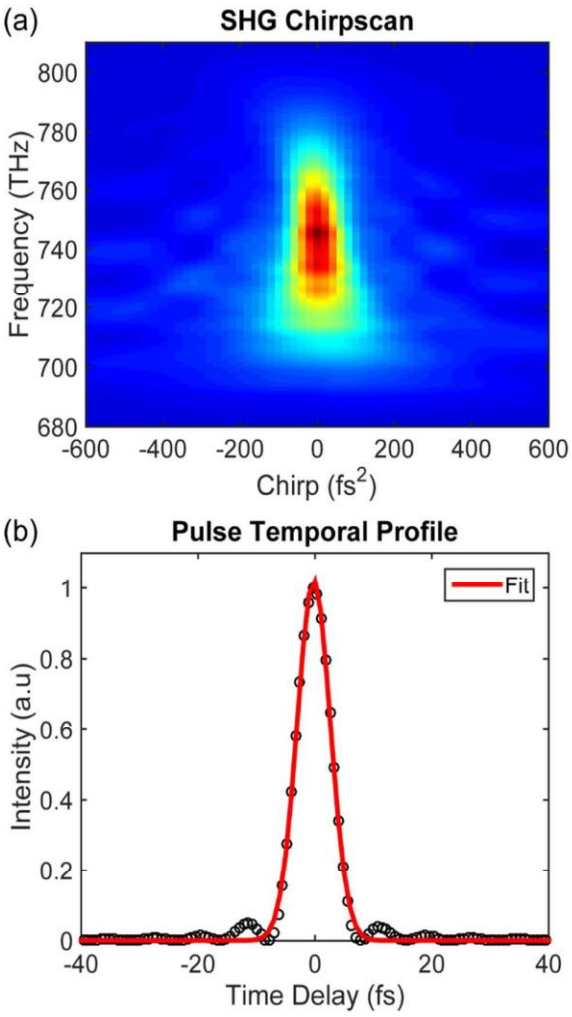

Figure 3.3 (a) The second harmonic of the DOPA with a range of applied chirp values. The narrow and uniform feature indicates that the pulses are well compressed. (b) A fit to the temporal profile of the DOPA pulse compressed to ~7 fs, generated based on the compression results.[12]

The pump source used in the experiments described here is a homebuilt degenerate optical parametric amplifier (DOPA) which is based on the design by Siddiqui et al.[57] The DOPA produces an output power of 8 μJ and covers a spectral range from about 680-920 nm. The DOPA pulses are compressed using chirped mirrors from LayerTec GmbH before being further compressed and shaped by the Dazzler. A typical DOPA spectrum is shown in Figure 3.4. Due to the design of the multispectral multidimensional spectrometer, we can easily switch

between the DOPA and NOPA pump beam paths using several mirrors on magnetic mounts. When switching between the DOPA and NOPA pumps, two lenses in a telescope after the Dazzler must also be switched so the optical coating matches the wavelength range of the current light source.

The probes for the experiments described in this thesis are broadband white light continua which allow us to detect energy transfer and charge separation processes in a broad spectral range. White light continua have been described and applied in a number of previous experiments.[43], [61]–[64] For the BRC experiments discussed here, we generate the white light continuum by pumping a 3 mm thick sapphire crystal with about 1 μJ of the 800nm light from the Spitfire regenerative amplifier. The resulting spectrum spans the visible spectral range from 460 to 700 nm as well as the near-IR from around 790 to 950 nm.[12] The desired spectral regime was selected by applying appropriate filters for visible and near-IR wavelengths. Typical white light spectra are shown in Figure 3.4. In both cases, the white light continua are significantly chirped. The resulting distortion of the spectra is corrected after data collection

using the procedure described below.[65]

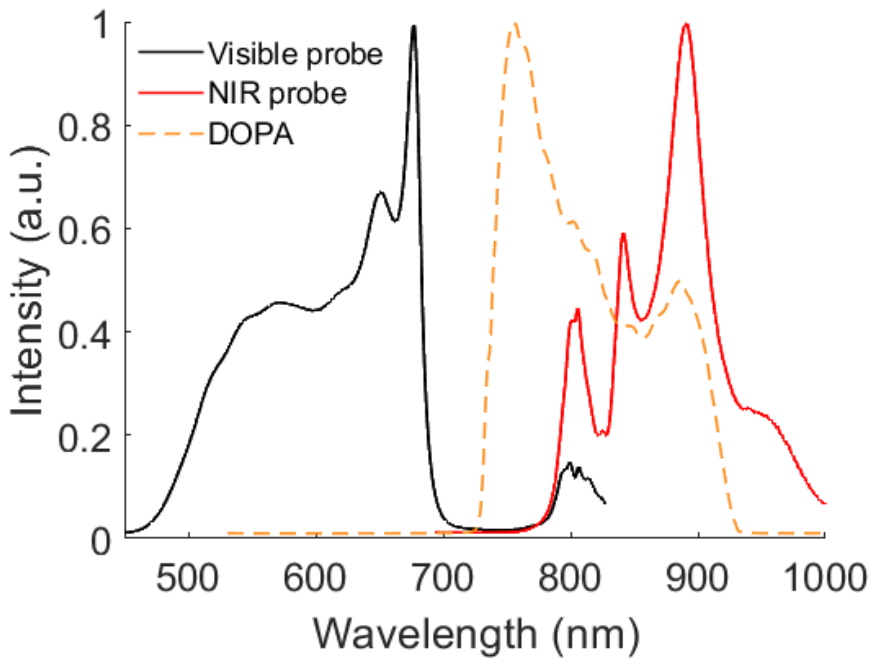

Figure 3.4 Representative pump and probe spectra are shown here. The solid spectra show the white light continua in the visible and near-IR regime. The dashed line shows the DOPA spectrum.

The delay between the pump and probe pulses (T) is set by a retroreflector on a delay stage which can scan delays of up to one nanosecond. The beams are focused and overlapped at the sample position at an angle of about two degrees, with polarization at the magic angle (~54.7°). The sample is cooled with liquid nitrogen to 77 K in a cryostat from Oxford Instruments. Probe light is collected directly using a Horiba Jobin Yvon (iHR320) spectrometer with a Pixis CCD camera from Princeton Instruments.[53]

Section 3.3 Data Processing

The white light continuum used as a probe in the experiments described here covers a broad range of frequencies, and possesses significant chirp, leading to a frequency dependent shift in the time overlap of the pump and probe pulses. This can significantly distort the

lineshapes and kinetics of the resulting data. In order to correct for this shift, we employ a method described previously.[65] We collect data to negative T values of 5 ps to ensure that signal appearing at negative times due to the chirp is included. We plot the T value corresponding to the rise of the signal as a function of detection frequency and fit these true T = 0 points to a third order polynomial. We then use this polynomial to generate a corrected T axis for each detection frequency point. For each point along the excitation frequency axis, we then interpolate the data along its corresponding corrected T axis to generate the corrected spectra. We identify the rise of the signal at a range of detection frequency points and fit these true T = 0 points to a third order polynomial. We then use this polynomial to generate a corrected T axis and interpolate the data along the T axis to generate the corrected spectra. We verified that the corrected spectra were accurate by checking that the frequency dependence of the rise of the signal at time zero was minimal.

Another challenge of performing broadband measurements is the dramatic difference in sample absorption between the Q_X and Q_Y bands. To achieve a reasonable signal to noise ratio, we typically use a BRC sample with an OD of about 0.3 in the wavelength regime of interest. In order to prepare a sample with an OD of 0.3 in the Q_X band, we had to accept a much higher OD of nearly 0.6 in the Q_Y band. A high sample OD can lead to various distortions in the 2D spectrum, as described in the 2015 paper by Spencer et al. Using the technique described in this same paper, we were able to approximately correct for these distortions [66]. We applied the following correction factor to the data:

$$S_{2D}(\omega_t, \omega_\tau, T) \approx \frac{A(\omega_\tau)\ln(10)/\gamma}{1-10^{-A(\omega_\tau)/\gamma}} \times 10^{A(\omega_t)/2\gamma} \times S_{2D}^{0}(\omega_t, \omega_\tau, T) \quad (2.1)$$

Here, S_{2D} is the corrected 2D spectrum, S_{2D}^{0} is the uncorrected 2D spectrum, and A is the linear absorption spectrum of the sample with the frequency axis defined by either the detection or excitation frequencies of the 2D data. The variable γ is related to the path length of the laser through the sample, and is given by

$$\gamma = \frac{(n - \sin^2\alpha - \sin^2\beta)^{\frac{1}{2}}}{n} \quad (2.2)$$

Here, 2α is the angle between the pump and probe beams, and 2β is the angle between the two pump beams. Both of these angles are taken to be zero for the pump-probe geometry. Although this is an approximation, the effect of a difference of several degrees in either α or β is negligible compared to the uncertainty in the index of refraction, n. We approximate the index of refraction as 1.4 for the 50% by volume glycerol:water solvent of our sample. Although this is the index of refraction for the solution at 20°C,[67] we expect that the temperature dependence of the index of refraction will not substantially affect the data correction. While data on the effect of freezing on the refractive index of glycerol is not readily available, the index of refraction of ice at -7°C is only 0.03 less than that of liquid water at 25°C.[68] Therefore, the index of refraction of the sample is expected to change by less than 0.1, and the effect on the overall correction to the data will be small.

Chapter 4 Multispectral Two-Dimensional Electronic Spectroscopy of the BRC

This chapter is based on the 2018 *Journal of Physical Chemistry Letters* paper by Arkaprabha Konar, Riley Sechrist, Yin Song, Veronica R. Policht, Philip D. Laible, David F. Bocian, Dewey Holten, Christine Kirmaier, and Jennifer P. Ogilvie titled "Electronic Interactions in the Bacterial Reaction Center Revealed by Two-Color 2D Electronic Spectroscopy" [12]. As the second author on this paper, I worked with Dr. Konar to collect the data shown below, prepared the BRC samples that were studied, and contributed to the interpretation and analysis of the data. Much of the text and figures in this chapter are taken directly from that paper, although some additional discussion is provided here.

Section 4.1 Background and Experimental Details

In this chapter we show results from BRC studies using excitation of the Q_Y band in the near-infrared and detection at higher frequencies in the Q_X region. The resulting two-color 2D spectra reveal a rich network of cross-peaks that reflect the electronic structure of the BRC and report on energy transfer and charge separation processes. Here, we will discuss the origin and qualitative kinetics of those cross-peaks. Our measurements are closely related to transient absorption experiments that have been performed over the past decade on the BRC using broad-band probes to detect transient changes in the Q_X region upon selective excitation in the Q_Y region.[19], [69] Several mechanisms and time scales pertaining to charge separation and energy transfer have been proposed based on those studies.[27], [70]

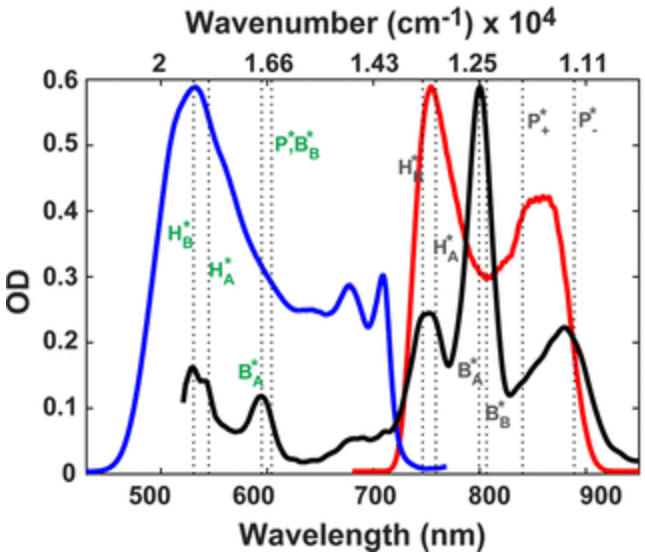

Figure 4.1 77 K absorption spectrum of the W(M250)V mutant (black) along with the broad-band pump (red) and the white-light continuum probe (blue) spectra. The Q_X[27] and Q_Y[1] transitions are labeled in green and black, respectively.

Figure 4.1 shows the 77 K absorption spectrum (black) of W(M250)V along with the broad-band pump (red) and probe spectra (blue). The absorption bands are labeled according to the absorption positions of the most prominent constituent chromophores in the Q_Y and Q_X regions. In the Q_Y region, the P_+* and P_-* transitions are indicated based on our previous assignment from fitting one-color 2DES data.[1] The B_A*, B_B*, H_A*, and H_B* transitions in the Q_Y band are named for the pigments on which the excitation is primarily localized. All of the Q_Y band assignments shown here are discussed in detail in previous work.[1] Also indicated are the Q_X assignments proposed by Huang et al.[27] The absorption bands of the bacteriochlorophyll in the Q_X region are not as well separated as those in the Q_Y, with the Q_X P* and B* band absorptions overlapping significantly at around 600 nm while the H_A* and H_B* transitions are slightly better separated at 543 and 530 nm,[18], [27] respectively. These assignments are used to interpret the results of the two-color experiments below.

The BRC spectrum shown in Figure 4.1 exhibits some unusual features. Most notably, the H and B Q_Y band peaks are less symmetric than expected. In addition, the P band is slightly weaker than usual relative to the other spectral features. This may indicate that the white light background used to collect this spectrum at 77K was inconsistent, or that some percentage of the sample was damaged or oxidized. However, further experiments with samples that did not exhibit these features in the linear absorption spectra gave similar 2D results, indicating that the charge conversion process was not significantly affected.

We used the multispectral multidimensional spectrometer described in Chapter 3 to perform 2DES experiments in the pump-probe geometry at the magic angle polarization (54.7°). Specifically, we used the two amplifiers, both operating at a 1 kHz repetition rate, to generate the DOPA pump and WLC probe pulses in the visible and near-IR respectively. The WLC was generated using approximately 1 μJ of power from the Spitfire focused on a 3 mm thick Sapphire plate to produce a spectrum spanning 460 – 730 nm. The pump was focused to a $1/e^2$ spot size of 245 μm and the probe was focused to 170 μm. The pump pulse was compressed to about 10 fs with a power at the sample position of 40 nJ, resulting in an estimated bleach rate of 15%. The M250V BRC sample was cooled with liquid nitrogen to 77K in an Oxford Instruments MicrostatN cryostat. The sample concentration was adjusted such that optical density of the Q_X peak corresponding to the H pigments was ~0.2 at 300 K.

Section 4.2 Results

In Figure 4.2, we present the two-color 2DES data of the BRC at 77 K at several waiting times following Q_Y excitation. The T = 20 fs 2D spectrum shown in Figure 4.2a is dominated by the broad excited-state absorption (ESA) from the Q_Y excited state that extends over the Q_X

detection region and has been characterized previously in transient absorption studies.[19], [70] In order to highlight the cross-peaks in the two-color 2D data, we subtract the ESA background corresponding to each excitation frequency for a given delay time, as described in the Appendix. We note that a similar ESA subtraction approach has previously been used in transient absorption experiments on the Photosystem II RC.[71] Background-subtracted real absorptive 2DES for several waiting times (20, 60, and 100 fs) are shown in Figure 4.2b. A representative 2D spectrum along with the BRC absorption regions and pump and probe spectra is shown in the Appendix. 2D spectra before ESA-subtraction and the corresponding ESA-subtracted spectra for additional T values are also shown in the appendix along with the fits to the broad ESA. In accordance with other 2DES studies and in contrast to transient absorption spectroscopy, the ground-state bleach (GSB) and stimulated emission (SE) contributions are positive while the ESA is negative. Given that the transitions of interest are in the Q_X region, we truncate the detection frequency axis to $\sim$15500 – 19300 cm^{-1}. On the 2D spectra, we indicate with vertical dotted lines the locations of Q_Y states previously assigned via global fitting of our one-color Q_Y 2DES data.[1] Proposed locations of the Q_X states from the literature are also indicated with horizontal dotted lines.[27] Positive contours in Figure 4.2 are plotted at 5, 7.5, 10, and 15% and in increments of 10% starting from 20%, while the negative contours are plotted in increments of 10% starting from 10%. The spectra for each T value are individually normalized to the maximum amplitude to highlight relative amplitude changes among the different cross-peaks. Significant cross-peak amplitude is detected at the H* Q_X frequencies corresponding to excitation of the H*, B*, and P* Q_Y transitions. We note that

alignment of the signal peak maxima with P^{-*} is poor due to the pump laser spectrum, which has considerably reduced amplitude at frequencies below ~11100 cm^{-1}.

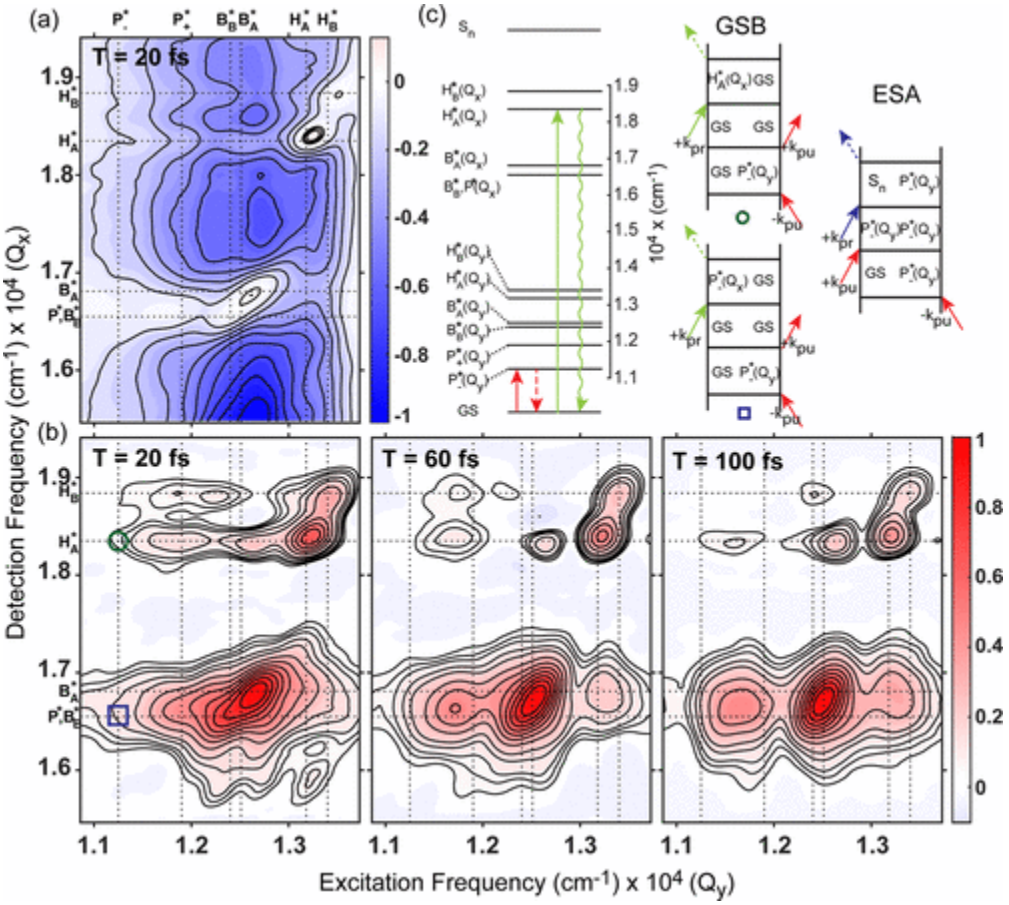

Figure 4.2 (a) Two-color 2D absorptive spectrum of BRC at 77 K at T = 20 fs. (b) ESA-subtracted 2D absorptive spectra for T = 20, 60, and 100 fs. (c) Wave-mixing diagrams showing a representative GSB pathway giving rise to a peak at $H_A^*(Q_X)$ upon exciting $P_-^*(Q_Y)$ (depicted by the green circle in the T = 20 fs spectrum). Also shown are double-sided Feynman diagrams depicting characteristic GSB and ESA pathways.

In Figure 4.2c, we depict representative Feynman diagrams for several major pathways that give rise to the observed spectral features in the two-color 2D spectra. These include the broad-band ESA that produces the negative background signal throughout this spectral region. More interesting are the positive GSB signals that indicate a common ground state between the Q_Y and Q_X transitions, consistent with the energy level structure shown in Figure 4.2c. The idea

of a common ground state does not necessarily imply strong electronic interactions of the chromophores associated with the transitions. The spectral overlap of the P* and B* transitions in the Q_X band prohibits clear resolution of the GSB cross-peaks involving Q_Y excitation of an arbitrary state and detection of the P* or B* Q_X transitions. However, the better separation of the H_A* and H_B* Q_X transitions enables resolution of the cross-peak amplitudes between the H* Q_X and all the Q_Y states of the BRC (Figure 4.2b).

Previous studies focused on the Q_Y region have documented ultrafast energy transfer between the P*, B*, and H* states. [13], [29], [69], [72], [73] More recently, 2DES studies have revealed H* → B*,[74], [75] B* → P*,[1], [76] B_A* → B_B*,[77] and P_+* → P_-*[1] energy transfer as a direct observable in below-diagonal cross-peaks in one-color 2D spectra. Energy transfer processes are also apparent in the two-color 2D spectra and account for the rapid decay within the first ~100 fs of many of the cross-peak features, particularly those involving excitation of H_A*(Q_Y) and H_B*(Q_Y).

The waiting time kinetics of the different cross-peaks at the relatively well-resolved H_A*(Q_X) and H_B*(Q_X) detection frequencies are shown in Figures 4.3a and 4.3b, respectively. The corresponding subtracted ESA contributions at these locations are shown in the Appendix. Several Feynman diagrams are necessary to understand the kinetics of the Q_Y–Q_X cross-peaks. In addition to the usual positive GSB and negative ESA contributions, an additional Feynman diagram is needed to account for the negative contribution due to excitation energy transfer (EET). Representative EET diagrams for the H_A*(Q_Y)/H_A*(Q_X) and P_+*(Q_Y)/H_A*(Q_X) cross-peaks are shown on the left side of Figure 4.3c and represent negative contributions to the GSB. These diagrams show the waiting time dependence of the excited-state population decaying to

the ground state following energy transfer. The right side of Figure 5.3c shows the positive GSB contributions due to a common ground state. The initial decay of the positive cross-peak amplitude, most evident in the $H_A^*(Q_Y)/H_A^*(Q_X)$ trace in Figure 4.3a and $H_B^*(Q_Y)/H_B^*(Q_X)$ in Figure 4.3b, can be understood as arising from the decay in the GSB signal as population on these states is returned to the ground state. The cross-peaks involving $P^*(Q_Y)$ excitations also show small energy transfer signals that can be understood from the GSB and EET diagrams depicted in the lower half of Figure 4.3c. The positive GSB signal that arises from the common ground state between $H^*(Q_X)$ and $P^*(Q_Y)$ is reduced when excited-state population transfers out of the $P^*(Q_Y)$ states.

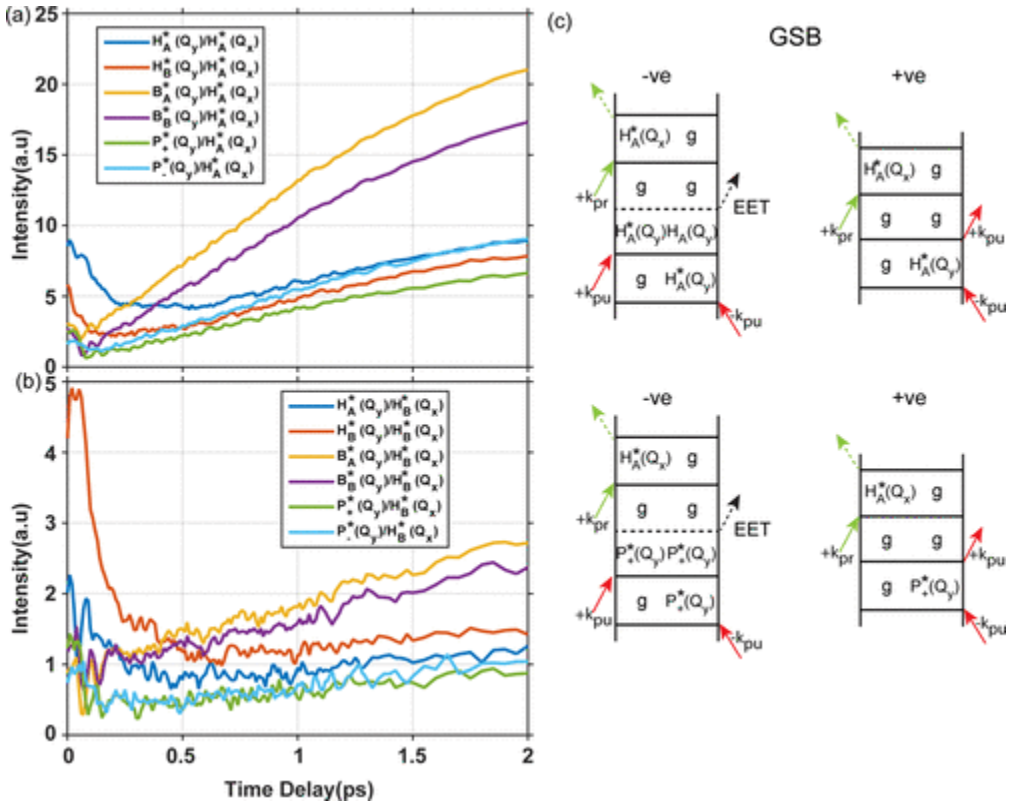

Figure 4.3 Kinetic plots corresponding to excitation at each of the six Q_y states and detection of (a) $H_A^*(Q_x)$ or (b) $H_B^*(Q_x)$ transitions for the ESA subtracted data. (c) Double-sided Feynman diagrams depicting the different rephasing contributions of the light–matter interactions involved in generation of the GSB signal.

The two-color 2D cross-peaks also clearly show the charge separation process, as shown in the 2D plots corresponding to the longer time delay (see the Appendix). Contrasting the kinetics for detection at $H_A^*(Q_X)$ and $H_B^*(Q_X)$ (Figure 4.3a,b, respectively), most of the cross-peak signals for $H_B^*(Q_X)$ remain relatively constant in amplitude after the initial decay, while the $H_A^*(Q_X)$ cross-peaks exhibit a rise on the ~2 ps time scale. This time scale has been attributed to formation of the charge-separated state $P^+H_A^-$.[1], [19], [78] The rise of the $H_A^*(Q_X)$ cross-peaks can be understood as an increase in the positive GSB signal due to depletion of the $H_A^*(Q_X)$ state that is no longer accessible after charge separation occurs. That is, because H_A is involved in the formation of the charge separated state, population can no longer form on the $H_A^*(Q_X)$ state, and the pathway depicted in the upper left of Figure 4.3c is inaccessible. In contrast, only a slight rise is seen in some of the $H_B^*(Q_X)$ cross-peaks. Because the H_B pigment is not involved in the charge separation process, no comparable increase in GSB signal is expected. It may be that the small rise is due in part to B-side electron transfer,[79] as well as Stark shifts of $H_B^*(Q_X)$ following charge separation.[80]

Section 4.3 Discussion

In addition to clear cross-peaks between the $H^*(Q_X)$ and the $P^*(Q_Y)$ and $B^*(Q_Y)$ states, the early waiting time 2D spectra show evidence for a cross-peak between $H_A^*(Q_Y)$ and $H_B^*(Q_X)$, indicating a common ground state. Given the weak coupling between H_A and H_B pigments, this is perhaps surprising.[13] We note that the $H_A^*(Q_X)$ cross-peaks are higher in amplitude than the $H_B^*(Qx)$ ones, which may reflect stronger coupling of H_A than H_B to the other BRC pigments. In addition, we note that the distinct cross-peaks in the T = 20 fs two-color 2D spectrum shown in Figure 4.2b support our previous assignment of P_+^* to 11900 cm^{-1} (840.3 nm) in the Q_Y

region.[1] The 2D spectra at later times show reduced cross-peak amplitude at P_+* excitation due to the rapid (∼25 fs) energy transfer to P_-*.[1] Previous theoretical and experimental studies have placed P_+* at a variety of different frequencies to the blue of our assignment. Specifically, experiments on *R. sphaeroides* at room temperature assign the value to 12121 cm^{-1} (825 nm)[72] using pump–probe spectroscopy, while low-temperature experiments (1.5–10 K) assign the P_+* position to between 12225 and 12821 cm^{-1} (818–780 nm).[15]–[17], [81] Theoretical work has predicted the P_+* frequency to be located at 12346 cm^{-1} (810 nm) and 12 285 cm^{-1} (814 nm) at 77 K and room temperature, respectively.[13] The low oscillator strength of P_+*, its coupling and proximity to other exciton states, and its rapid internal conversion have made it historically difficult to detect. The difference between our assignment and the previous values may be due to the different bacterial species being studied or because the higher dimensionality of our method enables detection and assignment of weak transitions.

Since the earliest studies of the BRC, the strength of coupling and accompanying excitation delocalization among the BRC hexamer has been central to proposed energy transfer and charge separation mechanisms.[13], [19], [29], [82] The couplings that have been reported for the BRC range from ∼400 to 750 cm^{-1} for the special pair, to several cm^{-1} between H and P and H_A and H_B.[13], [17], [82] The fact that we clearly resolve Q_Y/Q_X cross-peaks even among the most weakly coupled BRC transitions indicates that either the couplings are stronger than previously thought or two-color 2D spectroscopy is highly sensitive to coupling through a common ground state. The latter explanation seems the most likely. The presence of cross-peaks in one-color 2D spectroscopy at T = 0 indicates electronic coupling [34] and is typically interpreted as revealing strong (excitonic) coupling.[83] However, cross-peaks in 2D spectra

may have several components with different signs, including positively signed GSB and SE, as well as negatively signed ESA. In some cases, a lack of cross-peaks at T = 0 can be attributed to cancellation of GSB and ESA components rather than a lack of coupling. Such signal cancelations in 2DES are becoming more apparent with the increased use of fluorescence-detected 2DES,[84] for which GSB and ESA cross-peak components combine in a different manner.[85]–[87] We note that our one-color 2D data [1] in the Q_Y region at T = 11 fs shows little indication of any below-diagonal H–P cross-peaks, and the above-diagonal region is overwhelmed by ESA (see Figure 8 in the appendix). Although overlapping ESA signals are present in our two-color 2D data, the broad nature of the signals far from the excitation frequency allowed us to subtract the ESA and reveal the underlying GSB cross-peaks. This likely makes the two-color approach sensitive to weak coupling that is not readily apparent in one-color 2D spectra. The considerable structure of the ESA signals in the Q_Y region would complicate an ESA subtraction approach. In one-color 2D measurements, the detection of weak cross-peaks can be facilitated by polarization-dependent studies.[88], [89] In both one-color and two-color 2D spectroscopy, extracting the absolute electronic coupling strength from cross-peaks in 2D data will require careful modeling and proper weighting of the different signal contributions.

We note that GSB signals arising from a common ground state have been reported in pump–probe studies, where competing ESA signals have partially obscured the GSB contributions.[90] Unlike pump–probe spectroscopy, 2D spectroscopy resolves the excitation frequency, enabling resolution of individual GSB cross-peaks. Resolving individual GSB cross-peaks could be achieved with tunable narrow-band excitation in a series of pump–probe

experiments, but at the expense of time resolution, which could prove limiting in systems like the BRC with overlapping transitions and rapid <100 fs energy transfer.

Subsequent to the publication of these results in 2018, we discovered that we had incorrectly scanned the t_1 delay in this experiment. In a typical 2D experiment, data is collected at multiple t_1 points while the T waiting time is held fixed. Due to a misunderstanding about the data collection program, the t_1 delay was scanned by delaying the second pump pulse with respect to the first and third pulses, which effectively changed the waiting time in addition to the t_1 delay. This problem is most significant at early times when T is comparable to the t_1 delay, which is maximized at 120 fs. The error was corrected for all experiments presented in subsequent chapters, and a comparison of the results before and after the correction is shown in the appendix. We note that in particular the kinetics related to charge separation, which occur on the picosecond timescale, are not expected to be significantly affected by this error. The findings of this chapter are therefore still useful for developing a qualitative understanding of the BRC kinetics.

Section 4.4 Conclusions

In summary, we have shown that two-color 2DES is a sensitive approach for studying the electronic structure of the BRC via cross-peaks between Q_X and Q_Y transitions. With detection at significantly higher frequency than excitation, these cross-peaks reflect primarily the GSB signals arising from the common ground state shared by Q_X and Q_Y transitions. This approach enabled us to observe electronic interactions between excited states of the BRC, extending even to states previously considered to be largely localized on their respective A and B branches. Compared to one-color 2DES, where cross-peaks are often obscured by rapid energy

transfer or ESA signals, two-color 2DES offers a complementary and sensitive approach, capable of resolving weak couplings that have been reported to be in the <10 cm^{-1} range. The two-color approach should be particularly useful for probing the electronic structure and excited-state processes of multipigment systems containing transitions with varying degrees of spectral overlap in different spectral regions, as is common in natural and artificial light-harvesting systems.

Chapter 5 Kinetic Analysis

One of the challenges of 2DES is extracting useful insights from information-rich spectra. In order to obtain an accurate picture of the kinetics of energy transfer and charge separation in photosynthetic systems, 2DES data must be tested against a variety of relevant models using a computationally tractable approach. One possible solution is to use a global fitting approach that incorporates the excitation frequency dependence of the spectral information. In this chapter, we discuss the theoretical background for multiexcitation global fitting of 2D spectra,[91], [92] and then briefly discuss its application to 2DES data from the BRC Q_Y band.[1]

Several different methods have been used to quantify the kinetics of a system based on 2D data. One possibility is to use an approach that is analogous to global fitting of transient absorption (TA) data which reveals decay associated spectra (DAS) and their associated decay times. [92]–[95] When adapted to 2D data, this technique yields two-dimensional DAS with both excitation and detection frequency axes, with each 2D DAS associated with a decay time. [96]–[98] Similarly, one can use a sequential model and obtain 2D evolution associated spectra (EAS).[99]–[101] Alternatively, each frequency-frequency point in the 2D data set can be fit independently, yielding two-dimensional lifetime maps that can be used to interpret the kinetics associated with the spectral features.[102] However, none of these approaches takes advantage of the information about electronic structure that is inherent in the excitation-frequency information that is present in 2D spectra but lacking in TA spectra. For a system like the BRC, which has product states that do not depend strongly on the excitation frequency,

these methods fail to use the 2DES data as effectively as possible. The theory developed by Dostál et al. in 2016 takes advantage of the information content of 2D spectra to obtain species associated spectra (SAS) from 2DES data.[103] In the same year, Thyrhaug et al. applied this method with polarization control to the FMO complex to elucidate its electronic structure and the kinetics of energy transfer.[89] This approach was further generalized by Niedringhaus et al. to include reaction intermediates and test models of charge separation in the BRC based on 2DES data in the Q_Y region.[1] This technique will be discussed in this chapter, and then applied to broadband 2DES data in Chapter 6.

Section 5.1 Theory

When performing a global fit of transient absorption data, each distinct spectroscopic species is represented by a compartment in the model to be tested. Each compartment is associated with a time dependent concentration (c_i), a rate of transfer (k_i) and a wavelength-dependent difference spectrum (f_i). The experimental spectrum can be reconstructed using a linear combination of the difference spectra weighted by the concentrations.[92] For transient absorption experiments, this can be simply represented as

$$S(\lambda_{det}, t) = \sum_{i=1}^{n} c_i(t) f_i(\lambda_{det}) \tag{5.1}$$

A similar framework can be used for 2D experiments, with the key difference of incorporating the excitation wavelength dependence into the concentration. Note that we have not introduced excitation dependence into the difference spectra, as this would produce two-dimensional DAS, as in the 2D DAS approach. Instead, we use an approach similar to previous

treatments of temperature dependent data, where the excitation frequency dependence is included in the time dependent concentrations.[104]

$$S(\lambda_{det}, \lambda_{ex}, t) = \sum_{i=1}^{n} c_i(\lambda_{ex}, t) f_i(\lambda_{det}) \tag{5.2}$$

For a single excitation frequency this can be rewritten as a matrix in the form

$$\mathbf{S}_{(m\times p)} = \mathbf{C}_{(m\times n)}\mathbf{F}_{(n\times p)} \tag{5.3}$$

with the matrix dimensions given by m time points, n compartments, and p detection frequencies. With q excitation frequencies, we stack the matrices to give

$$\mathbf{S}_{(q\times(m\times p))} = \mathbf{C}_{(q\times(m\times n))}\mathbf{F}_{(n\times p))} \tag{5.4}$$

When the model accurately reflects the physical system, the basis spectra will correspond to the spectral signatures of actual chemical species of the system and the reconstructed spectrum will match the experimental data. In the terminology of spectral fitting, the basis spectra will be the Species Associated Difference Spectra (SADS).

The time dependence of the concentrations can be described with a differential equation

$$\frac{d}{dt} c_i(\lambda_{ex}, t) = \sum_{j=1}^{n} K_{ij} c_j(\lambda_{ex}, t) + a_i(\lambda_{ex}, t) \tag{5.5}$$

where K_{ij} is a matrix which defines the rate of population transfer between each of the n species. The term $a_i(\lambda_{ex}, t)$ contains information about the initial conditions, with

$$a_i(\lambda_{ex}, t) = a_0(\lambda_{ex}, t) I_p(\lambda_{ex}, t) \tag{5.6}$$

We can interpret a_i as the probability of exciting a particular species with the pump, and can therefore calculate it according to

$$a_i(\lambda_{ex}) = \left(1 - 10^{-\sigma_i(\lambda_{ex})}\right) I_p(\lambda_{ex}) \tag{5.7}$$

Here, σ_i is the contribution of each species (indicated by the subscript i) to the linear absorption spectra of the sample. The total linear absorption measurement can be written as the sum of the contributions of each species: $\sigma(\lambda) = \sum_i^n \sigma_i(\lambda)$. The second term, I_p, is related to the integral of the pump photon flux over the excitation wavelength.[91] In order to calculate a_i, the linear absorption lineshapes can be fit to calculate the relative contributions of the various species and extract their peak positions, width, and dipole strengths. It is possible to fit the linear absorption spectrum either before or during the optimization of the 2DES fitting.

The general solution to the time dependent differential equation of concentrations is

$$c(\lambda_{ex}, t) = e^{Kt} * a(\lambda_{ex}, t) \tag{5.8}$$

with * indicating a convolution. In order to evaluate the term e^{Kt}, which contains a nondiagonal matrix in the exponential, we can use an eigenvector-eigenvalue decomposition to diagonalize the matrix K. With this information, the time dependent concentrations can be calculated and the optimized SADS can be found by minimizing the Frobenius norm, $\|\mathbf{S} - \mathbf{CF}\|_F$, which is the sum of the squares of each matrix element. This will give n optimized one-dimensional basis spectra.

In some cases, it is advantageous to apply additional constraints to the SADS during the optimization. One useful approach is to constrain the SADS to have the lineshapes that are used for the initial conditions. This technique was applied by Dostal et al. to the FMO complex.[103], [105] While this approach avoids generating SADS that are inconsistent with the linear absorption lineshapes, not all basis spectra for the BRC will have SADS that can be accurately represented using these simple lineshapes. However, it is possible to take advantage of both

approaches by separating the basis spectra into two terms – those that can be represented by the linear absorption lineshapes and those that cannot. We can separate out these terms in both the concentration matrix and the SADS matrix from equation 5.4

$$\boldsymbol{S} = [\boldsymbol{C_1} \quad \boldsymbol{C_2}] \begin{bmatrix} \boldsymbol{F_1} \\ \boldsymbol{F_2} \end{bmatrix} \tag{5.9}$$

The columns of $\boldsymbol{C_1}$ will be the columns of $\boldsymbol{C}$ corresponding to the constrained spectra and the columns of $\boldsymbol{C_2}$ will be the columns of $\boldsymbol{C}$ corresponding to the unconstrained spectra. $\boldsymbol{F_2}$ contains the unconstrained SADS while $\boldsymbol{F_1}$ contains the SADS calculated from a linear combination of the linear absorption lineshapes:

$$\boldsymbol{F_1} = \boldsymbol{GL} \tag{5.10}$$

where the rows of $\boldsymbol{L}$ are spectra from the linear absorption fitting or another set of basis spectra that can be used to construct the SADS, and G is a square matrix of coefficients. In this way, it is possible to obtain a complete set of SADS with some SADS being deterimined independently by the nonlinear optimization and others being constained by the lineshapes of the spectra from the initial conditions.

This analysis scheme can be easily expanded to include multiple datasets, as long as the datasets depend on the same kinetic rates. The residuals for the fit to each dataset can be calculated separately, weighted relative to eachother, and then summed before passing it to the optimizer. In the case of 2DES data, datasets that cover different detection frequencies can be combined in this way. If the T axis and the excitation frequency axis are the same for both datasets, then it is not even necessary to calculate separate concentration matrices for the two datasets, as all the information can be contained within the same concentration matrix.[91]

Section 5.2 Additional considerations for fitting

In order to ensure the accuracy of the kinetic fitting, a number of important considerations should be taken into account. Several of them are described here.

Unless sufficient constraints are imposed, it is possible to generate fitting results that are not unique. Multiple sets of SADS and rates may satisfy the optimization scheme and reproduce the experimental spectra equally well. Therefore, additional information must be supplied to obtain results that are physically meaningful.[92], [106] This additional information might come from structural considerations, other fitting methods, or comparison with results from the literature. Each of these sources may provide information about the expected rates, number of compartments, or structure of the SADS. In order to compare with the more common transient absorption fitting results, one can restrict the excitation wavelength axis during the optimization to a very narrow region which mimics transient absorption data. In any case, multiple models should be tested and compared to achieve the most accurate result.[91]

As mentioned in the previous section, another decision that is important for obtaining reasonable optimization results is whether to fit the linear absorption data before or concurrently with the 2D data. If the linear spectrum is fit first, the rate constants will be the only nonlinear parameters in the 2DES fitting. If they are fit concurrently, the linear absorption parameters – peak position, width, and dipole strength – will also be nonlinear parameters in the 2DES fitting. The former approach is simpler, faster, and less likely to yield local minima. However, it treats the linear spectra and the 2D spectra as independent. The latter approach is slower and more difficult to implement, but it allows the optimization to be constrained by both datasets simultaneously. When using this latter approach, the residuals from the linear

absorption fitting and the 2DES fitting are weighted relative to each other, and this weighting factor must be chosen carefully to give reasonable results.

One particularly technical consideration relates to sources of error in the initial conditions. The initial conditions given in equation 5.7 depend on the relative optical density of the sample and the instrument response as a function of wavelength, so anything that affects the linear absorption measurement or pump spectrum at different wavelengths can impact the fitting. This includes such factors as the CCD quantum efficiency and any optics between the sample position and the CCD including the spectrometer grating. Any wavelength dependent factors should be corrected before calculating the initial conditions.

Section 5.3 Kinetic fitting of the Q_Y band

The approach described in section 6.1, has been applied to absorptive 2DES data of the M250V mutant of the BRC at 77K.[1] This initial study performed excitation and detection in the Q_Y band and was used to extract exciton energies and test charge separation models in the BRC. In this work, the initial excitation of H_A^*, H_B^*, B_A^*, B_B^*, P_-^*, and P_+^* is represented by SADS using lineshapes constrained in the method of Dostal et al.[103] The SADS of the charge separated state $P^+B_A^-$ is then calculated independently by linear least squares. In order to accurately represent the inhomogeneous broadening of the B_A and B_B features along the diagonal, the SADS for $B_{A(I)}$ and $B_{B(I)}$ are represented by the sum of a series of distributed Lorentzian peaks. The weighting of these peaks is determined by the initial conditions, and the homogeneous and inhomogeneous widths are optimized in the fitting. Likewise, a series of derivative lineshapes based on the Lorentzian peaks is used to approximate the Stark shift feature that appears in the

final charge separated state, $P^+H_A^-$. The value of the Stark shift was optimized independently in the fitting.

A full discussion of the results of this analysis can be found in [1], but a brief overview of the work will be given here to motivate the broadband 2DES study presented in Chapter 6. Two different kinetic models for charge separation were tested using this approach. In one model, charge separation proceeds via a single pathway, while in the second model two parallel pathways are allowed. The kinetic rates, SADS, and relative fits associated with each of the models were compared, and it was determined that the simpler single pathway model shown in Figure 5.1a gave the most physically reasonable results. The SADS produced by this fitting are shown in Figure 5.1b. The SADS for H_A^*, H_B^*, B_A^*, and B_B^* use the lineshape from the fit to the linear absorption spectrum, while the SADS for P_-^*, and P_+^* are determined from a fit to the data at the single excitation frequency of 11,900 cm^{-1}. The SADS from this single frequency excitation associated with the fastest time component (35 fs) was used for the upper P exciton, while the SADS associated with a 2 ps component was used for the lower P exciton. As shown in Figure 5.2, the multiexcitation global fitting approach was able to reliably reproduce the major features of the 2D spectra. Due to the good agreement with the inhomogeneous broadening in the B band and the Stark shift of $P^+H_A^-$, we were able to obtain the reasonable values of 207 and 135 cm^{-1} for the Stark shift of the B_A and B_B transitions respectively. Of particular note in this study was the assignment of the weak upper special pair exciton energy to 11,900 cm^{-1} which has been notoriously difficult to determine due to its small transition strength and its proximity to the strong B band.

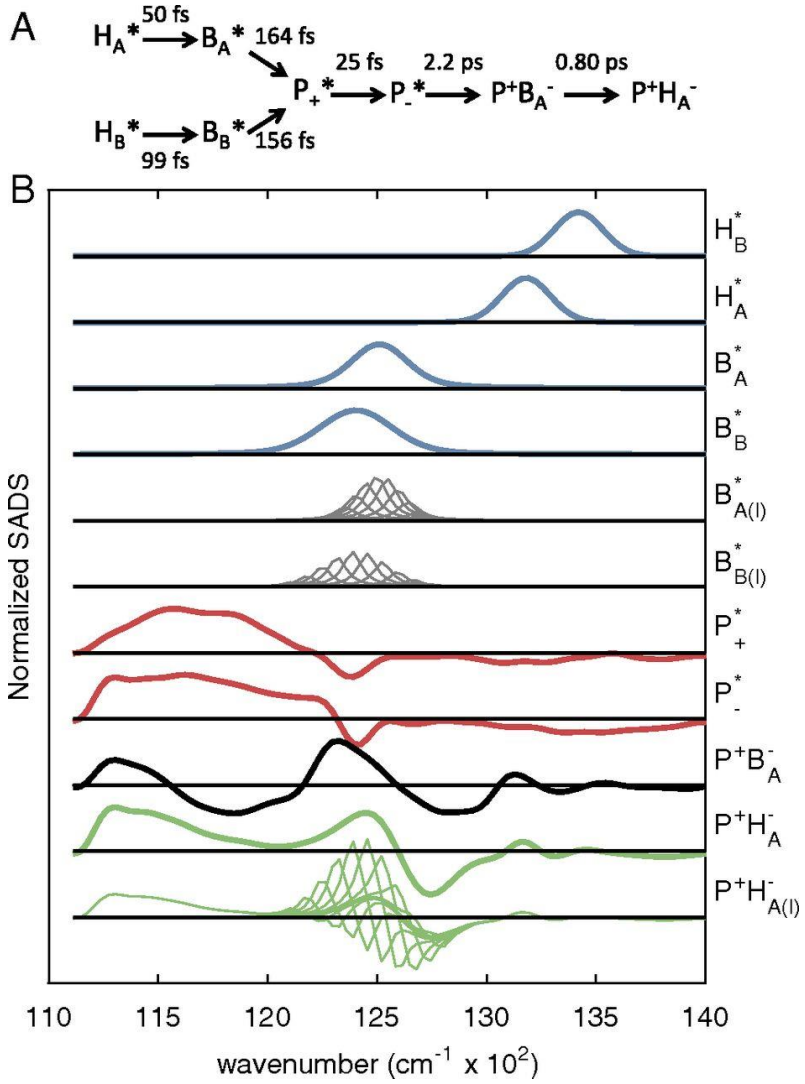

Figure 5.1 a) Kinetic model showing energy transfer and charge separation pathway. The rates were extracted from the kinetic analysis. b) SADS for the basis states used in the kinetic analysis. The $B^*_{A(I)}$ and $B^*_{A(I)}$ show a subset of the Lorentzian lineshapes included in the SADS.

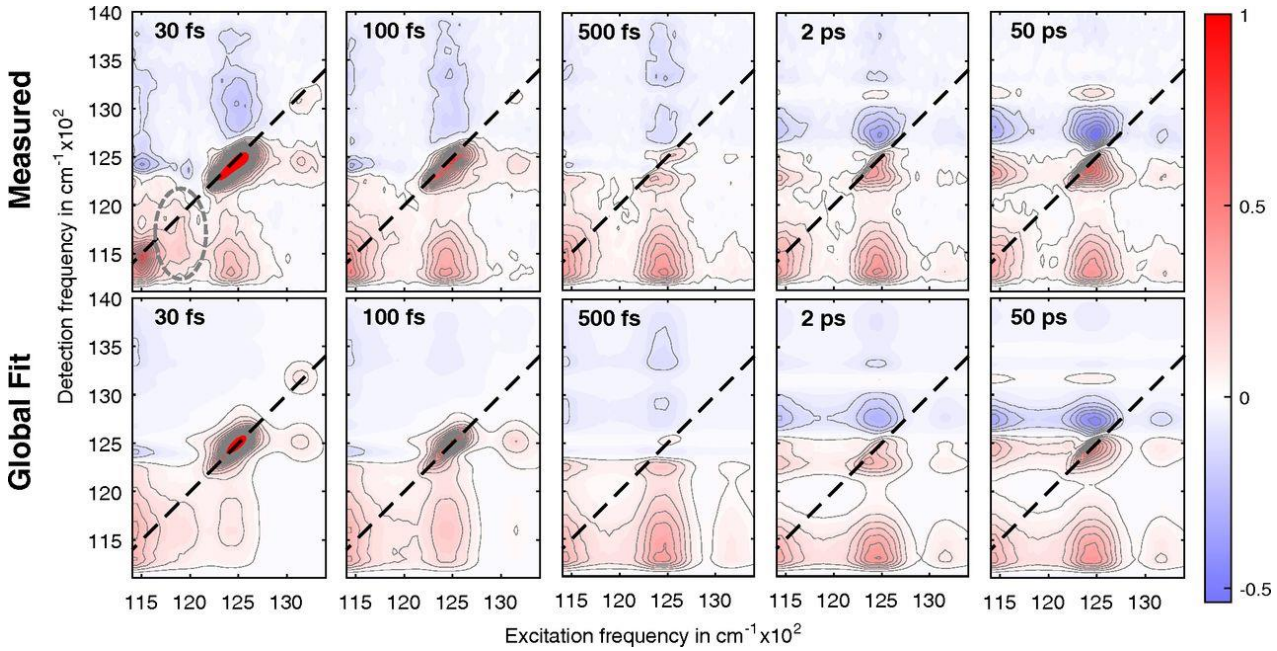

Figure 5.2 A comparison of the measured 2D data (top) and the fit to the data (bottom) at various T times. The major features of the spectrum are reproduced, including the inhomogeneous broadening of the diagonal B band peak and the Stark shift of the charge separated state at longer times. The dashed oval indicates a weak cross-peak arising from excitonic coupling between the special pair excitons. This cross-peak, as well as the kinetic fitting enabled assignment of the P_+* energy of 11,900 cm^{-1}.

Chapter 6 Kinetic Fitting of Broadband Probe 2DES Spectra of the BRC

The kinetic analysis described in Chapter 5 provided insight into the charge separation mechanism and determination of Q_Y exciton energies of the BRC. In this Chapter, we will extend this approach to incorporate data in which the Q_Y transitions of the BRC are once again excited, but both the Q_X and Q_Y bands are probed with a broadband continuum. This will allow us to describe the features of the charge separated states of the BRC across this broadband region and set the stage for future work to incorporate additional complimentary 2DES data sets that will further constrain models of the kinetics of energy conversion in the BRC.

We obtained a broadband 2DES dataset using the methods described in Chapter 3. Two types of data sets were collected using the same BRC sample, with a DOPA pump and a white light continuum probe. For the first data set, the visible region of the white light continuum was selected by a filter to create a visible probe beam. For the second data set, the near-IR region was selected instead. The pump and probe spectra are shown in Chapter 3. After dividing out the probe along each detection axis, these data sets were scaled relative to each other such that overlapping features had the same amplitude. The portion of the visible spectra that

overlapped with the near-IR spectra was then truncated and the data sets were combined to create a continuous broadband spectrum, as shown in Figure 6.1.

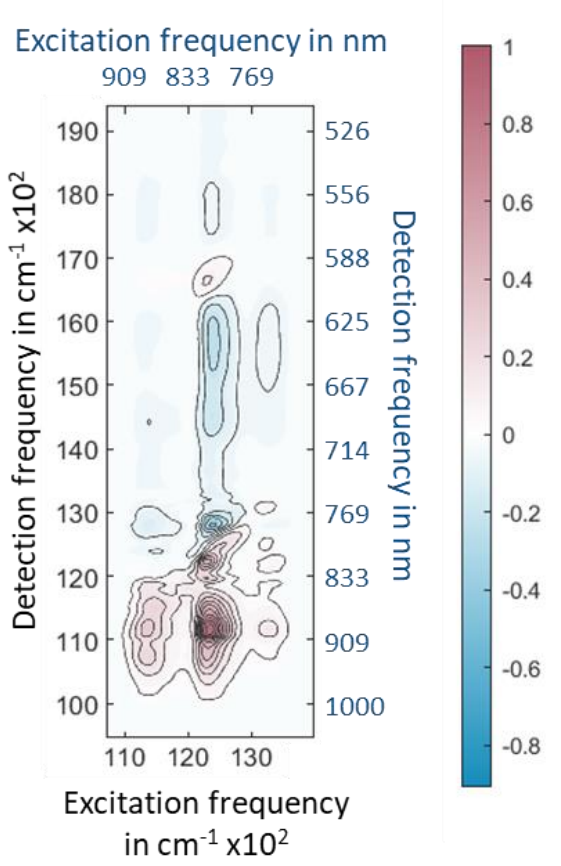

Figure 6.1 Broadband 2DES spectrum at T = 100 fs, created using combined visible and near-IR data sets.

The overall technique for performing the multiexcitation global fitting over this broadband spectrum is similar to that used for the Q_Y band alone, with some additional considerations. The same kinetic model is applied, with the population of each compartment giving rise to features in both the Q_X and Q_Y regions. Therefore, each SADS represents the

spectral contribution of both the Q_X and Q_Y transitions for a given state, and must also take into account other contributions in this wavelength region such as ESA signals.

Section 6.1 Accounting for Excited State Absorption

In the Q_Y band, ESA features appear above the diagonal, but are weaker and separated from the GSB signals, and were therefore not included in the previous study. In the Q_X band, however, ESA signals dominate much of the spectrum and significantly obscure the underlying GSB features. A physically realistic model of the Q_X band signatures must therefore take into account the ESA contributions. One could imagine using an approach like the one described in Chapter 4, in which the negative ESA contributions are fit with a polynomial and subtracted from the data, leaving behind the GSB features. While that technique was valuable for revealing the underlying GSB signatures and making qualitative assertions about the electronic structure, there is a significant risk that such an approach would contaminate the GSB kinetics. Therefore, to allow for a quantitative analysis of the kinetics we adopt a different approach.

A straightforward way to include ESA signatures without compromising the GSB kinetic is to include the ESA signatures in the SADS for each state. This approach relies on the assumption that the ESA signatures for each of the exciton states will exhibit the same kinetics as the exciton populations. Because the concentrations rather than the SADS contain all the time dependence when calculating a fit to the 2D spectrum, this ensures that the kinetics will not be artificially altered. However, this means that ESA features must be added to each SADS

in a way that does not compromise the information about the spectral features that we want to extract from that SADS.

For the H_A and H_B excitons, we want to take advantage of the relatively large separation of the H_A and H_B features in the Q_X band to obtain information about the peak positions and constrain the 2D fit based on the linear absorption fit. In the Q_Y band, we accomplish this by representing the GSB features of the H_A and H_B SADS using Gaussian peaks obtained from fitting the BRC linear absorption spectrum. A similar approach was used in the Q_X band. However, due to the broad features and overlapping contributions in the Q_X band, further work is required to obtain a reasonable fit to these features in the linear absorption spectrum. As a first approximation, the central frequency of the Q_X band GSB Gaussians were set based on the assignments of Huang et al.[27], which appear to give an acceptable fit to the Q_X peak positions in the linear absorption spectra and 2D data. The ESA features were added as broad negative Gaussians. The central frequencies and amplitudes of these Gaussians were fit as a ratio of the corresponding GSB Gaussian values. Likewise, the positions of the ESA Gaussians were offset by a constant with respect to the Q_Y GSB Gaussian central frequency. The SADS constructed by the addition of these three Gaussians can be seen in the top two traces of Figure 6.2.

Some different considerations were necessary to incorporate ESA signatures into the SADS for B_A and B_B. We found that the ESA features in the B band were not well-described by Gaussians but exhibited considerably more complex structure. Additionally, to obtain a reasonable fit to the data in the Q_Y band, it is necessary to account for the strong inhomogeneous broadening of the B Q_Y band features that we identified in our previous work.[1] Therefore, we constructed the B_A and B_B SADS using the inhomogeneous Lorentzian

substates based on the linear absorption fit in the Q_Y band, as described previously [1], but added a narrow negative Gaussian to produce the ESA feature that appears just above the diagonal in the Q_Y region. The spectral features along the rest of the detection axis were generated by fitting the data at the single excitation frequencies of 12400 cm^{-1} for B_B and 12510 cm^{-1} for B_A. This approach assumes that no states other than B_B and B_A are excited at these excitation frequencies. The amplitude of these lineshapes was scaled according to the contribution of each associated exciton population, thus ensuring an appropriate relative amplitude of each of the spectral features.

The SADS for the remaining states, which give rise to the spectra at longer times, already incorporate ESA features without further modifications. The P_+^* and P_-^* SADS are based on the linear least squares fits to the data at the excitation frequencies of 11900 cm^{-1} and 11250 cm^{-1} respectively. The charge separated state $P^+B_A^-$ is also calculated by linear least squares. The final charge separated state, $P^+H_A^-$, incorporates the Lorentzian lineshapes representing the Stark shift as described previously.[1] The other spectral features are represented by taking a slice along the detection axis at long times when the system has uniformly reached the $P^+H_A^-$ state.

Section 6.2 Results

The SADS produced from this analysis are shown in Figure 6.2 below. The Q_X features in the B_A^* and B_B^* SADS show up approximately at the expected locations assigned by Huang et al., allowing for a small shift due to the uneven ESA background.[27] The SADS for the charge separated intermediate, $P^+B_A^-$, has been extended into the Q_X band. A negative contribution at 16500 - 16800 cm^{-1} indicates the loss of GSB from P_+^*, P_-^*, B_A^*, and B_B^* upon formation of $P^+B_A^-$.

A very weak negative feature is also present at the detection frequency of H_A^*. In the Q_Y band, the $P^+B_A^-$ SADS shows the derivative lineshapes present in the result found by Niedringhaus et al., except for the region from approximately 12500 to 12800 cm^{-1} where a positive feature is now present. This appears at the same location as the derivative lineshape created by adding

the inhomogeneously broadened ESA contribution to B_A^* and B_B^*, and is likely due to the addition of the ESA.

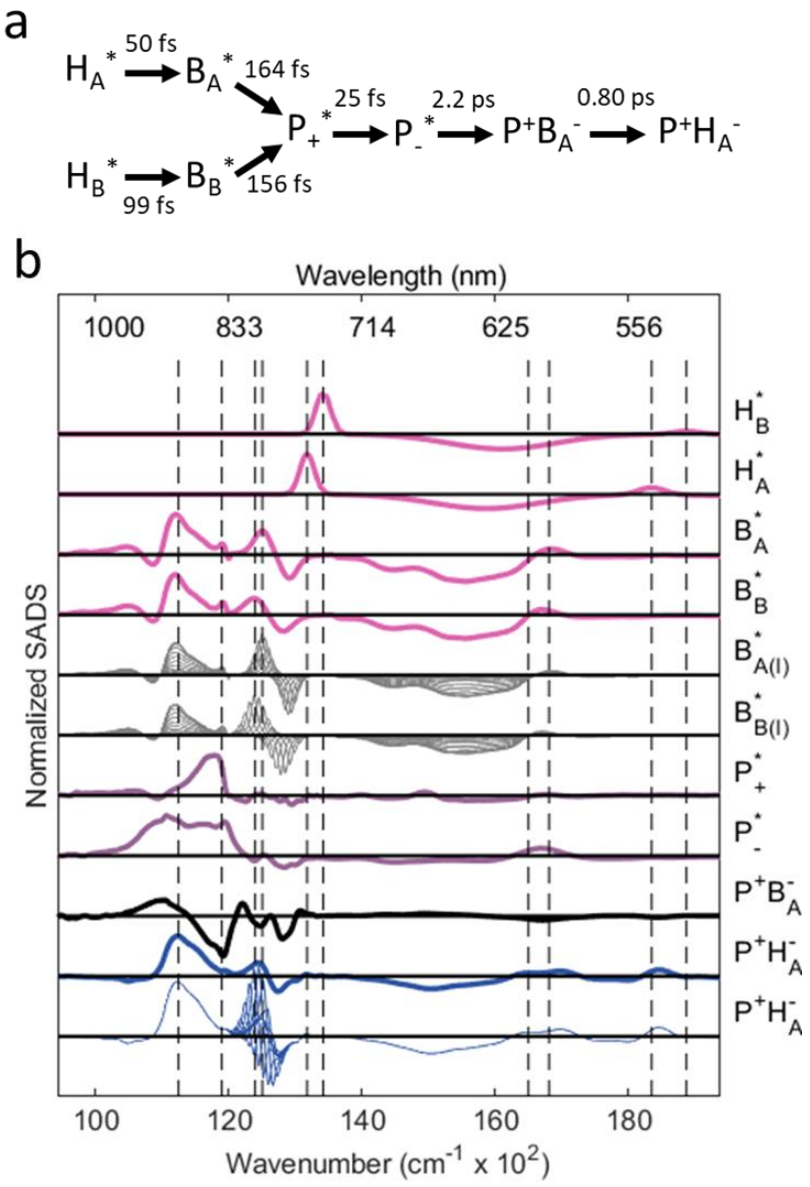

Figure 6.2 a) The single-pathway kinetic model with associated rates used in both the Q_Y band and broadband global kinetic fitting. b) Species Associated Difference Spectra (SADS) for the excitonic states and charge separated states used in the kinetic fitting scheme. The source of each of the SADS is discussed in the text. The vertical dashed lines indicate the expected exciton locations. The positions in the Q_Y band are based on the results of the Q_Y band multiexcitation global kinetic analysis[1] while the results in the Q_X band are set by the assignments of Huang et

al.[27] The $B^*_{A(I)}$, $B^*_{B(I)}$, and $P^+H^-_{A(I)}$ SADS show a subset of the states used to construct those SADS.

Together, the SADS and concentrations are used to calculate the fit to the 2D spectra at each T point using the single charge separation pathway model and kinetic rates determined previously (Figure 6.2). A comparison of the fit to the measured data is shown in Figure 6.3. Here, we see that the major features of the measured 2D data that appear across the broad detection axis are largely accounted for in the fit. In particular, the ESA features appear at the correct location and the Q_X band GSB signals are accounted for in the fit. However, several inconsistencies are also present. At early times, the ESA just above the diagonal in the B band is much narrower in the fit than in the measured data. The data also shows a diagonal elongation of the Q_X band features upon excitation of B_A and B_B, which is not reflected in the fit. Both of these discrepancies could be resolved by further improvements to the inhomogeneously broadened substate lineshapes in these regions. Nevertheless, the current model lays the

foundation for further improvements by incorporating the additional features of the broadband visible to near-IR detection axis.

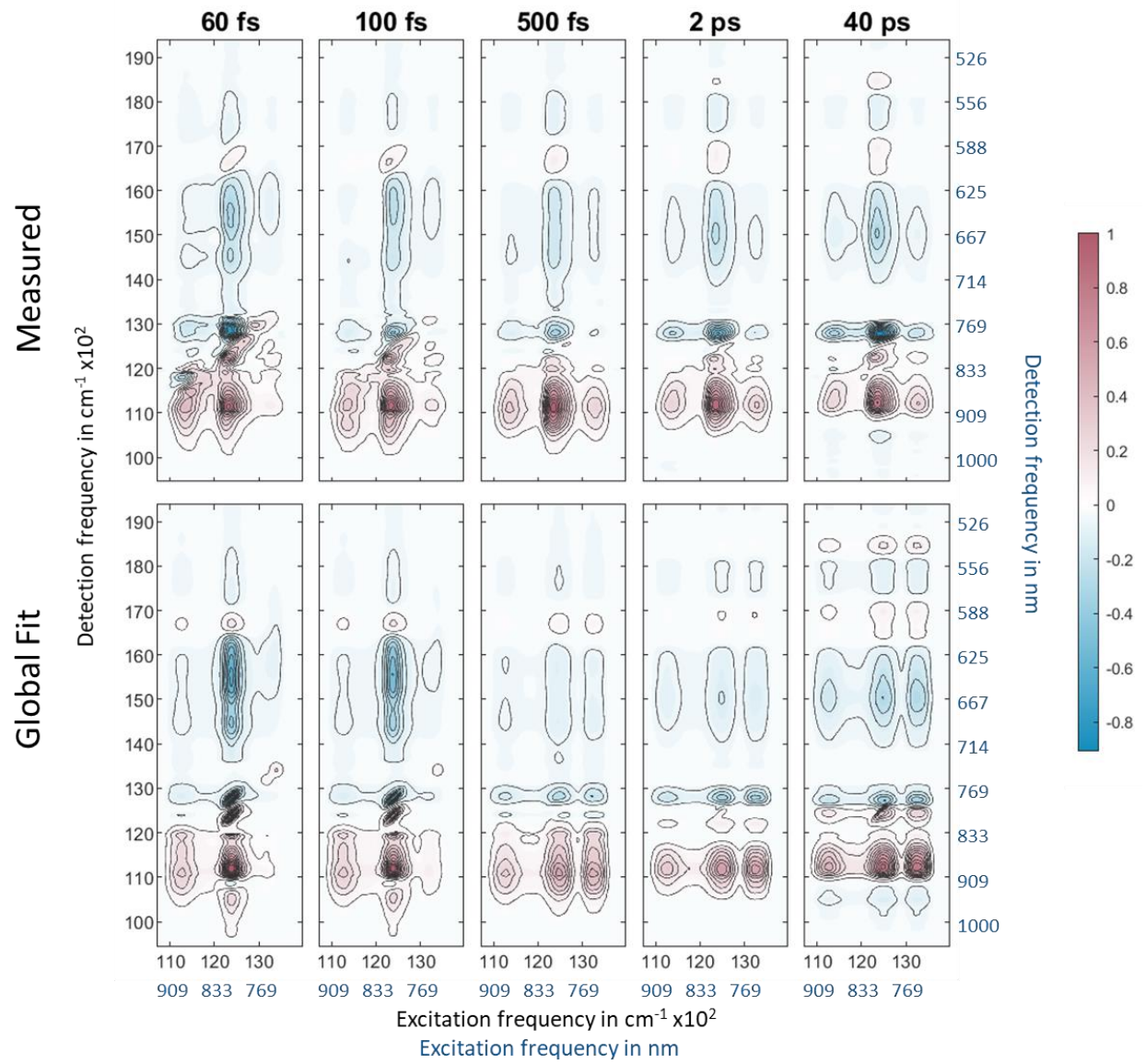

Figure 6.3 A comparison of the measured 2D spectra (top) and the fit to the data (bottom) for a series of waiting time points.

We can more easily compare the quality of the fit to the data by looking at slices along the detection axis at particular excitation frequencies, as shown in Figure 6.4. These slices reveal that at early times, the ESA at the B_A and B_B excitation frequencies is significantly

overestimated. This could be in part due to overestimating the initial population of the B_A^* and B_B^* excitonic states, although in that case we would expect the fit to be uniformly overestimated across the detection axis. Additionally, the fit at 13200 cm^{-1} excitation, corresponding to excitation of a combination of H_A^* and H_B^*, overestimates the population in the final state compared to the measured data. Both of these discrepancies could be explained by an additional loss pathway from the H_A^* and H_B^* states. This would result in less energy transfer from H_A^* and H_B^* to B_A^* and B_B^* in the first 100 fs, and would therefore reduce the amplitude of the B_A^* and B_B^* features at early times. This change would not significantly affect the amplitude of the P_+^* and P_-^* features on the same timescale, due to the longer energy transfer time from H_A^* and H_B^* to P_+^*. Adding a pathway for excitation of H_A^* and H_B^* to decay would also reduce the amplitude of the $P^+H_A^-$ state at longer times following excitation of H_A^* and H_B^*. The addition of a loss pathway to the kinetic model could account for the largest discrepancies we observe in the fit. However, the presence of such a pathway would be surprising, as the charge conversion process occurs with near unity quantum efficiency, so nearly every excitation of H_A^* and H_B^* should result in the final charge separated state without significant loss.[3] In order to fully understand these discrepancies it will be necessary to

explore additional models that allow for loss from H_A^* and H_B^*, and further refine the extracted rate kinetics to ensure that the physical process of charge conversion is accurately represented.

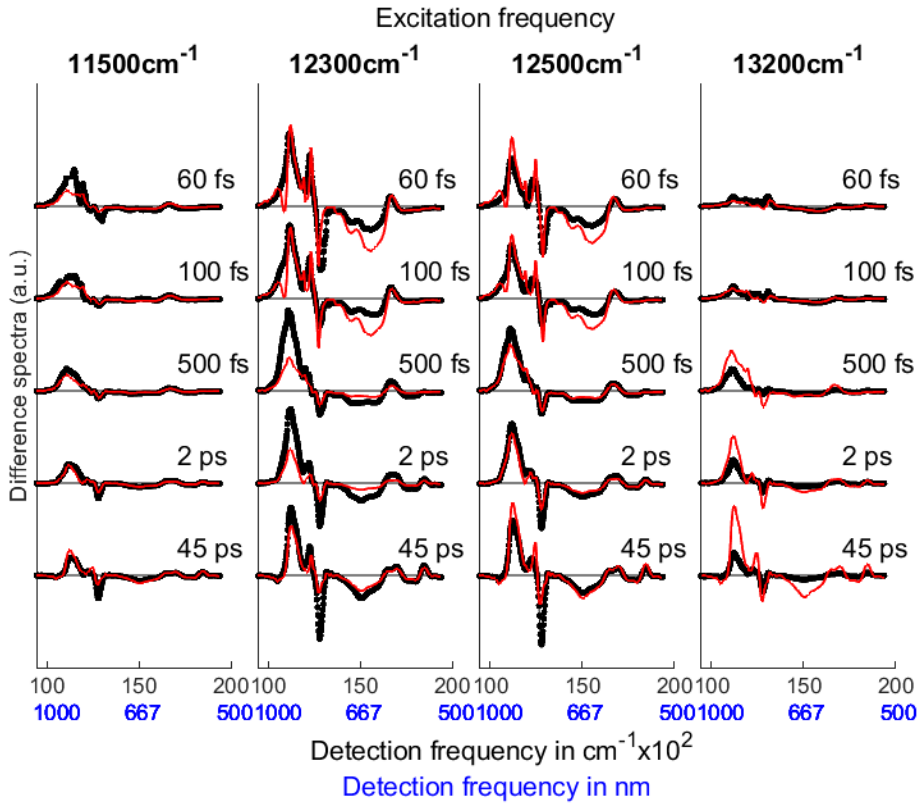

Figure 6.4 Detection axis slices of 2DES data (black) and fits to the data (red) for several excitation frequencies and waiting times.

Section 6.3 Future Work

In this chapter, we have combined both Q_X and Q_Y band spectra in the multiexcitation global fitting analysis and more fully characterized the broadband charge separated states. However, further work is necessary to take full advantage of this progress. In this work, only the Q_Y band linear absorption spectra was used to calculate peak positions in the 2D data. By performing a complete fit to the linear absorption spectrum in the Q_X band, the H_A^* and H_B^* SADS could be further constrained, and transition frequencies for these excitonic states could

be extracted from the fit. This would require identifying and fitting all the features that contribute to the linear absorption spectrum of the BRC in the Q_X region, including vibronic progressions, the carotenoid absorption, and any wavelength-dependent background. Unfortunately, this is a significant task which would require introducing further constraints to produce a unique fit despite the broad overlapping features in the Q_X band.

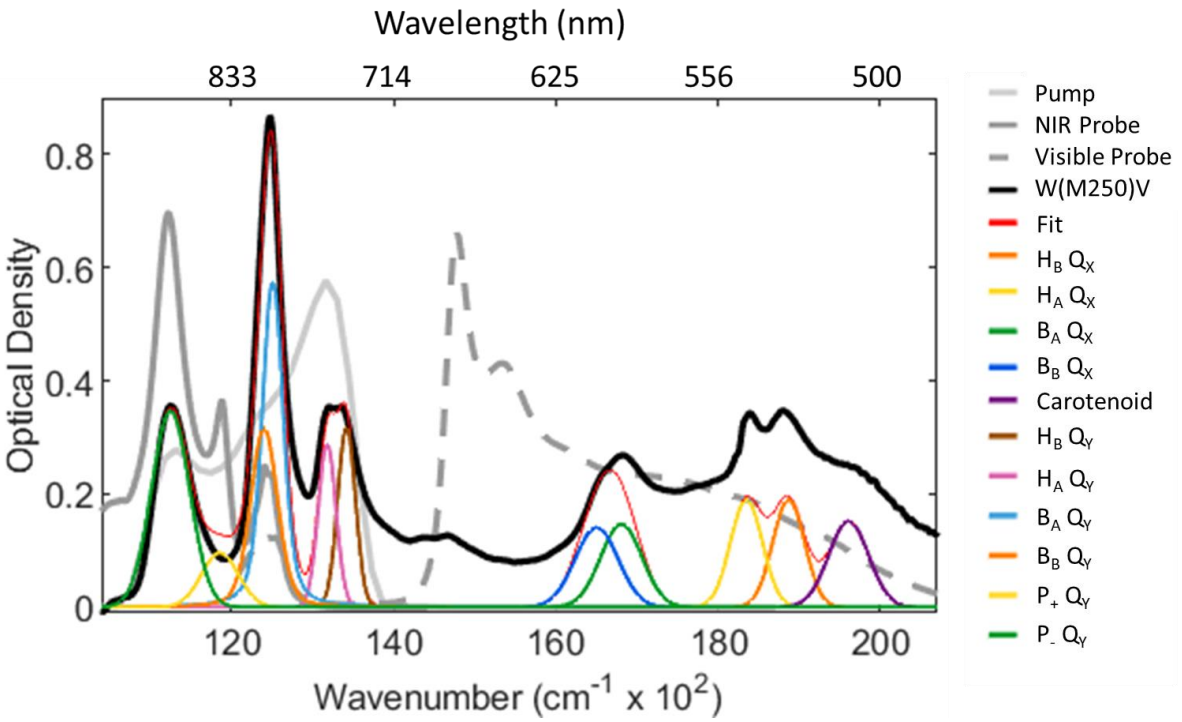

Figure 6.5 Linear absorption spectrum of the BRC and the fit to the spectrum, along with the pump and probe spectra. Each excitonic state is represented by a Gaussian to produce a fit to the linear absorption spectrum. Although the fit matches the experimental spectrum reasonably well in the Q_Y band, the broad overlapping features in the Q_X band make producing a unique fit to the data much more challenging. Further work is needed to accurately represent the spectral contributions to the Q_X band linear absorption spectrum.

In addition, a number of inconsistencies between the measured data and the fit persist. A more complete understanding of the source of these inconsistencies will require investigation of other kinetic models. In particular, it may be necessary to revisit the treatment of the inhomogeneously broadened B substates to ensure that the initial excitation and population

transfer reflect the experimental observations. The corrections to the data described in Section 3.3 should prevent errors due to the high OD of the sample, which would otherwise affect the calculated initial population, particularly in the B band. However, in order to observe the weak signals in the Q_X band, we had to excite the sample with relatively strong pump pulses, leading to excitation of an estimated 33% of the BRCs. It is possible that a non-negligible population of the BRCs was doubly excited, which could lead to altered initial population kinetics that are not accounted for in our model. Future experiments investigating the pump power dependence of these results could resolve this issue, although the weak Q_X signals make this an experimentally challenging task.

A major complicating factor in fitting the Q_X band is the strong overlapping ESA signature that obscures the GSB features. Experiments that have similar kinetics but different ESA contributions would provide complementary information that could be used to isolate the underlying GSB kinetics. Fluorescence-detected 2D shows particular promise for reducing ESA signals and may allow us to obtain a more complete picture of the spectral signatures and kinetics of the BRC and other systems of interest.[85], [107] Although further investigation is required to describe the discrepancies we see between the fit and the data and to extract additional information from the analysis presented here, this analysis should provide a useful starting point for the combined analysis of additional datasets.

Chapter 7 Conclusions

Section 7.1 Summary

In this thesis, we have presented the results of 2DES of the M250V BRC mutant at 77K. Using 2DES allows us to probe the electronic structure of this photosynthetic pigment-protein complex while avoiding the spectral congestion that is a common barrier in linear spectroscopy, and achieve high time and frequency resolution to follow its energy conversion kinetics. In Chapter 3, we discussed the results of a qualitative interpretation of two-color 2DES using a near-IR pump to excite the BRC Q_Y band, and a visible probe to investigate the Q_X band. We subtracted the overlapping ESA in this region, and observed an extensive network of cross-peaks between the Q_X and Q_Y transitions. Due to the large energy difference between these transitions and their appearance at early times, these features are consistent with GSB signals arising due to the existence of a common ground state between the Q_X and Q_Y transitions rather than energy transfer between them. The GSB peaks in the 2D spectra at early waiting times further validated our assignment of the upper special pair exciton energy that has been a subject of considerable debate in the literature. We have shown that two-color 2DES is a valuable tool for probing electronic coupling between states, and can be used in combination with one-color 2DES to compare regions with different degrees of spectral overlap between transitions of interest.

For a quantitative analysis of the kinetics of the BRC, we used data across a broadband detection region from the Q_Y in the near-IR to the Q_X in the visible spectral region. The full dataset was fit using a consistent kinetic scheme described previously.[1] Although the Q_X band features are obscured by ESA, we were able to describe the ESA using a combination of

Gaussian features derived from the Q_Y band linear absorption spectrum and linear least squares fits at individual excitation frequencies for specific excitonic states. Through multiexcitation global fitting to a single charge separation pathway model, this allowed us to extract the spectral signatures of the charge separated states spanning the Q_Y and Q_X bands. The calculated 2D spectra from this approach capture the main features of the experimental spectra, helping validate the single charge separation pathway model and associated rates, while also providing information about the Q_X transition frequencies. Several notable discrepancies remain between the measured data and the calculated 2D spectra that require further exploration.

Section 7.2 Future Directions

Further analysis of the broadband 2DES data and follow-up experiments will provide additional insight into the electronic structure and charge separation mechanisms of the BRC:

- *Simultaneous fitting of linear absorption spectrum in Q_X*: The kinetic fitting of the broadband 2DES spectra depends on the fit to the linear absorption spectrum in the Q_Y regime. A logical extension would be to set the positions of the H_A and H_B excitonic GSB contributions based on the linear absorption spectrum fit, especially since H_A and H_B are well separated from the bacteriochlorophyll contributions in the Q_X band. There is a significant background on the linear absorption spectrum in this region that will need to be considered in order to obtain an accurate fit.
- *Comparison of multiple kinetic models*: The kinetic fitting method described in Chapter 5 can be a valuable tool for discriminating between different models and identifying which is a most accurate reflection of the physical system. Further, exploration of different kinetic pathways and methods of producing inhomogeneous lineshapes will

likely shed light on the shortcomings of the model used in Chapter 5 and reveal more accurate representations that produce better fits to the data.

- *Testing and refining excitonic models of the BRC*: While multiexcitation global fitting determines the exciton energies, true understanding of the structure-function relationship of the BRC requires knowledge of the pigment site energies and couplings that produce the excitonic states of the system. The broadband 2DES data presented in this thesis as well as future polarization-dependent 2DES studies will provide an extensive data set for simulations that can test and refine exciton models.
- *2DES with a mid-IR probe*: We have extended the detection axis across the near-IR and visible spectral range, which provided more information to use in the kinetic fitting. The technical capabilities of the Laboratory for Ultrafast Multidimensional Optical Spectroscopy allow us to also collect data using a near-IR pump and mid-IR probe.[53] We could therefore extend the detection axis even further into the mid-IR and obtain an extreme broadband dataset dependent on the same underlying kinetics and take advantage of mid-IR spectral signatures of charge separation.[108] Using such a dataset for simultaneous kinetic fitting like we described here would necessarily require a careful application of constraints to accurately fit the data across the entire detection axis. However, a mid-IR dataset would provide useful complementary information to further constrain models of charge separation and provide rich spectral signatures to validate excitonic models of the BRC.
- *Fluorescence-detected 2DES*: One of the principal challenges of fitting data in the Q_X band of the BRC is the overlapping ESA features. Our group has implemented

fluorescence-detected 2DES.[87], [109], [110] Fluorescence-detected 2DES has different ESA pathways compared to traditional 2DES and has been shown to cleanly reveal GSB features with little contributions from ESA.[107] It may therefore be a valuable source of complementary information about the underlying GSB energies and kinetics. By either fitting fluorescence-detected data simultaneously with 2DES data, or simply using the insight gained by fluorescence-detected data to inform the fitting of 2DES data, it may be possible to overcome many of the current barriers to fully incorporating the Q_X band data.

- *New BRC mutants*: An exciting new development in work on the BRC is the creation of a BRC mutant in which electron transfer occurs almost entirely on the B branch.[23] 2DES studies on such a mutant could reveal critical insight into the effect of inhomogeneous broadening and the Stark shift observed in the final charge separated state. Those features were of particular interest in modelling the Q_Y band of the M250V BRC, and a comparison of these effects in a mutant with B band transfer could help to quantify and identify conclusively the source of these features and their dependence on the A or B branch.
- *Application to other systems*: The kinetic fitting scheme described here has been applied to the BRC, but it is certainly applicable to a wide range of systems. In particular, the insight gained into managing overlapping signals may be particularly valuable when applying this approach to other photosynthetic systems that have more spectral congestion than the BRC Q_Y band. It would be relatively straightforward to apply this approach to other species of the BRC, such as *Rhodobacter sphaeroides*, which has been

used for a wide variety of spectroscopic experiments and most likely has a very similar kinetic scheme. However, one can imagine applying this kinetic fitting scheme to nearly any photosynthetic system with a well defined set of excitonic states, so long as the spectral features are sufficiently well-resolved.

APPENDICES

Appendix A. Comparison of Data Before and After Time Delay Correction

Section 4.3 describes an error in the pulse delay sequence that caused changes in the t_1 time delay to also cause changes in the T time delay. This error affected the data presented in Chapter 4. This appendix presents a comparison of this data with data collected after correcting this error. The ESA from the collected data was subtracted using the same method as the original Chapter 4 data. As illustrated in the comparison below, some of the peak shapes are altered in the corrected data. Some of these differences can be attributed to the different structure of the probe pulses used in the different experiments. The existence of the network of cross-peaks made apparent upon subtraction of the dominant ESA signal is consistent across both data sets, confirming the main finding reported in the paper upon which Chapter 4 is based.[12]

The pump, probe, and linear absorption spectra from both experiments are shown in Figure A.1.

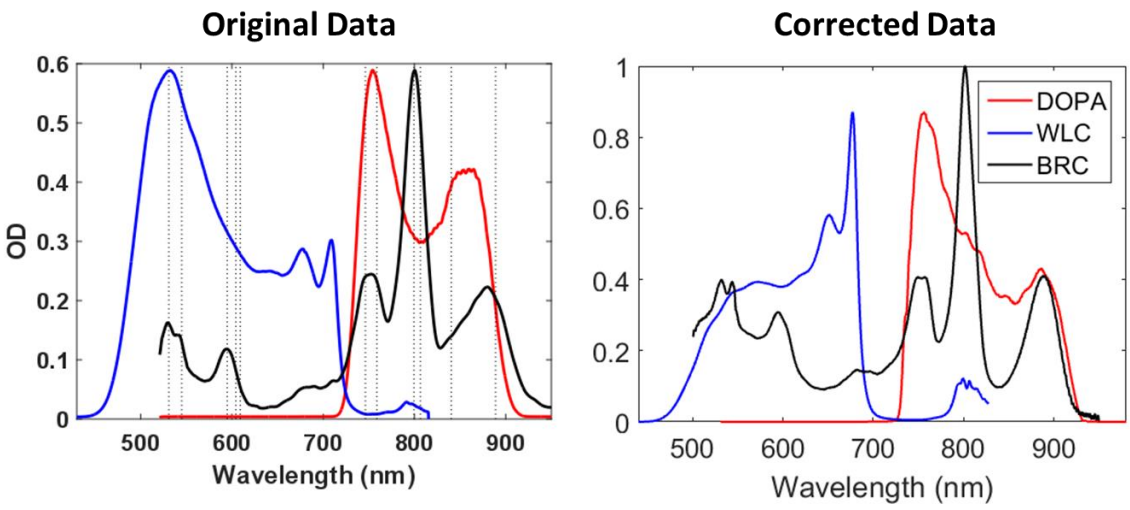

Figure A.1 (left) Linear absorption spectrum (black), pump (red), and probe (blue) used to collect the data presented in Chapter 4. (right) Linear absorption spectrum (black), pump (red), and probe (blue) used to collect data after correcting the time delay error.

Figure A.2 shows the T = 20 fs spectra for the original data and the equivalent spectrum from the corrected data. The cross peaks at excitation of P and detection of H in the corrected data are less prominent than in the original data, although this could be explained by the lower probe amplitude in the H Q_X band in the corrected data. The lineshapes of the corrected data are also different, which could be due to the mixing of T points in the original data. The corrected data is also noisier due to the probe amplitude, which could also be distorting the peak shapes.

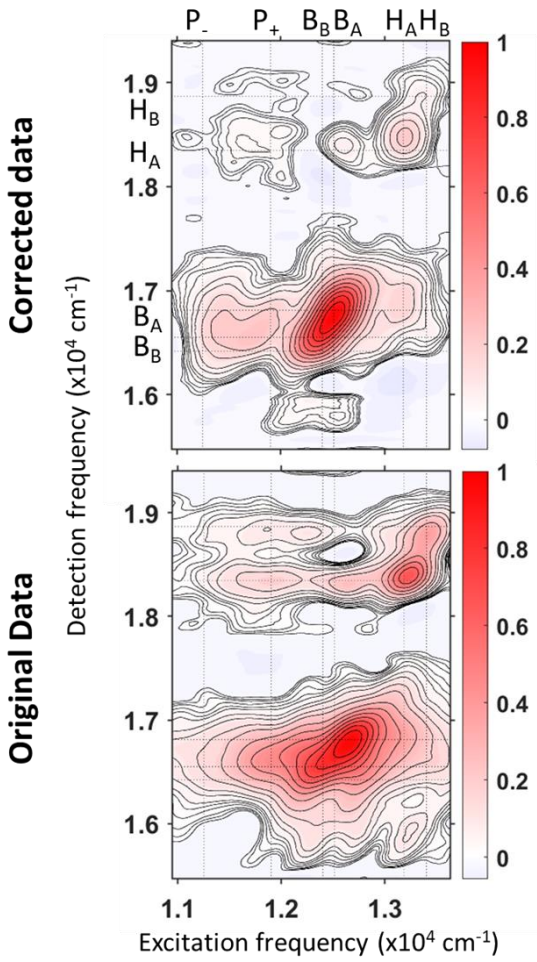

Figure A.2 Comparison of 2D spectra at T = 20 fs for corrected data and original data. The expected exciton locations are marked with gray dotted lines at the Q_Y frequencies assigned by Niedringhaus et al,[1] and the Q_X frequencies assigned by Huang et al.[27]

To more directly compare the peak amplitudes, Figure A.3 shows only the H_A and H_B Q_X detection region of the 2D spectrum. The spectrum is normalized to the maximum value of the GSB at H_A Q_Y excitation and H_A Q_X detection. In this figure, it is clear that the relative amplitudes of the peaks in this region are consistent between the original data and the corrected data, suggesting that differences in the pump and probe spectra are responsible for the differences in the absolute amplitude of these features.

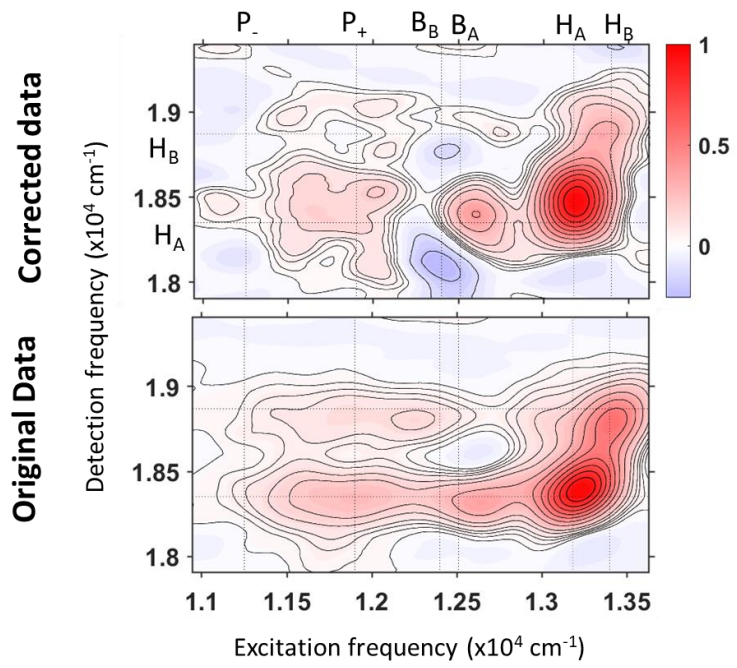

Figure A.3 2D spectra showing the HA and HB detection region for the corrected data (top) and the original data (bottom). The expected exciton locations are marked with gray dotted lines at the Q_Y frequencies assigned by Niedringhaus et al,[1] and the Q_X frequencies assigned by Huang et al.[27]

In Chapter 4, we discussed the qualitative kinetics of the H_A and H_B Q_X GSB. A comparison of the kinetics is shown below. Although the signal to noise ratio of the corrected data is lower due to the lower amplitude of the probe in this region of the spectrum, the same general features are present. There are also small differences in the kinetic traces at very early times, which is likely due to differences in the chirp correction, which could result in small shifts in time zero between different data sets. It is also notable that in the corrected data, the features excited at B_A and B_B have kinetic traces that are nearly overlapping, while in the original data, the B_A traces have a higher intensity. A similar trend is visible in the kinetics of the ESA contribution that was subtracted out.

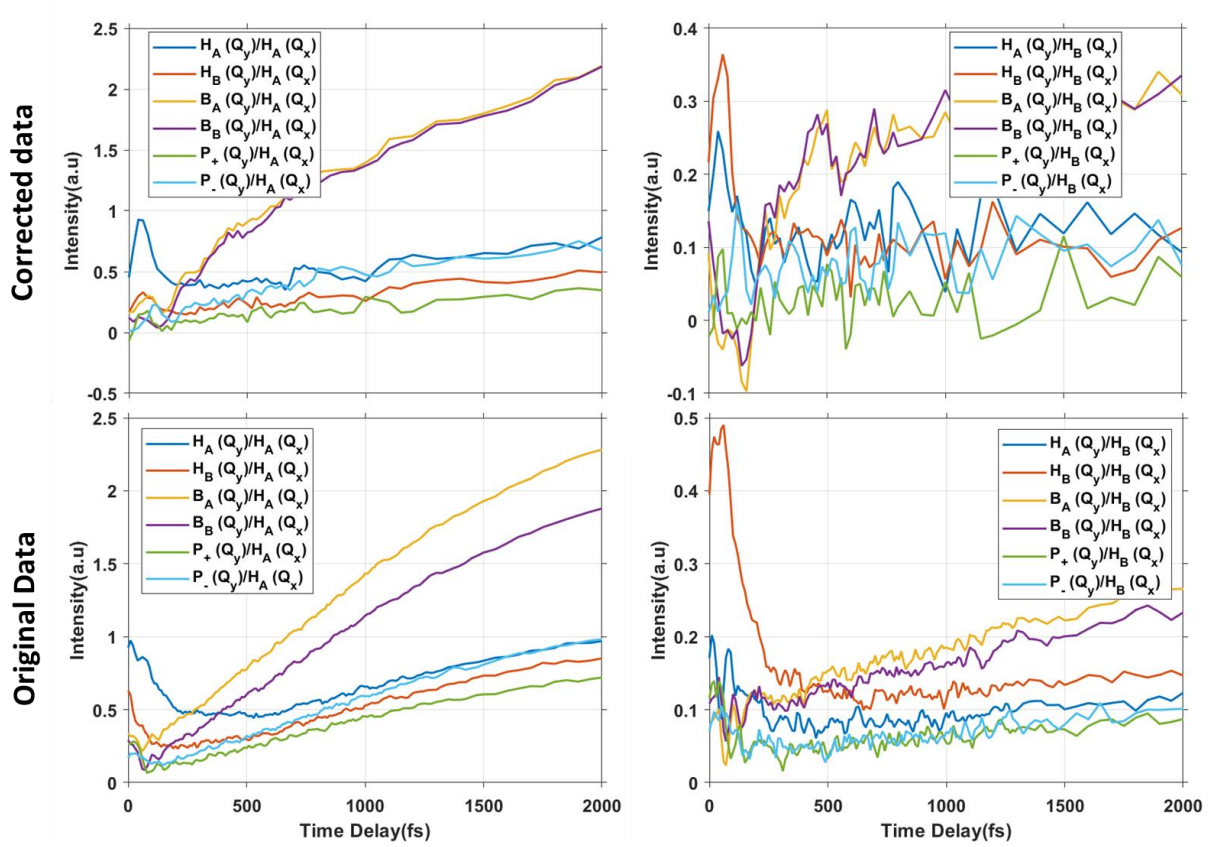

Figure A.4 Kinetic traces of the corrected data (top) and the original data (bottom) at selected exciton positions indicated in the legend. All the traces in the figure on the left were detected at $H_A(Q_X)$ and all the traces on the right were deteced at $H_B(Q_X)$.

For comparison, the kinetics of the subtracted ESA background is also shown. The ESA features in both data sets have similar trends. Although most of the ESA traces show only weak T dependence, the traces of the peaks excited at B_A and B_B show much stronger kinetics on similar time scales similar to the GSB, which motivated the more rigorous consideration of ESA contributions addressed in Chapter 6.

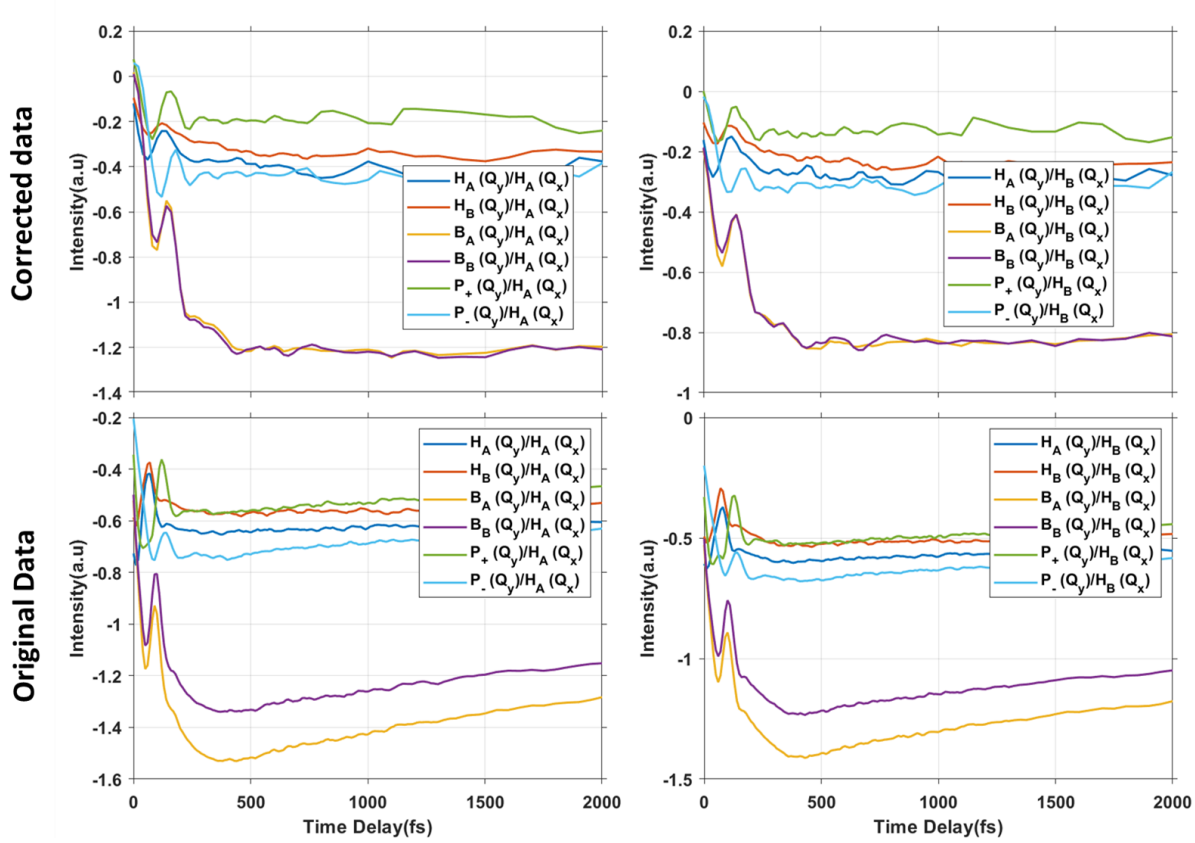

Figure A.5 Kinetic traces of the subtracted ESA from the corrected data (top) and the original data (bottom) at selected exciton positions indicated in the legend. All the traces in the figure on the left were detected at $H_A(Q_X)$ and all the traces on the right were deteced at $H_B(Q_X)$.

Appendix B. Subtraction of Excited State Absorption Kinetics

This Appendix is reproduced from the Supporting Information from Konar et al.[12]

The raw absorptive 2D spectrum displays negative excited state absorption (ESA) and positive ground state bleach (GSB) signals. In this section, we are primarily interested in the origin and kinetics of the GSB cross-peaks. The ESA signals arise from higher lying transitions accessed from the Qy excited states, while the GSB signals arise from the bleaching of the Qx transitions. The ESA signals are much stronger than the GSB signals and therefore obscure the actual magnitude of the GSB signals as shown in Figure 0.2. The ESA signals are generally very broad and can be approximated by fitting to a lower order polynomial. We identified regions of the ESA spectrum at the edges (15465 – 15600 cm-1), (19,100 – 19400 cm-1) and between 17,700 – 17,805 cm-1 that are not contaminated by GSB signals and fit slices along the detection axis for each excitation frequency to a second order polynomial. This process is repeated for all the waiting time values. The ESA subtracted 2D absorptive plots for several waiting times are shown in Figure 0.3 and the corresponding 2D plots constructed from the polynomial background fits are shown in Figure 0.4. Representative plots showing the raw data (blue) along with the polynomial fit to the ESA background (red) and the ESA subtracted data (yellow) at T = 150 fs are shown in Figure 0.5. The regions used for fitting are highlighted with gray squares.

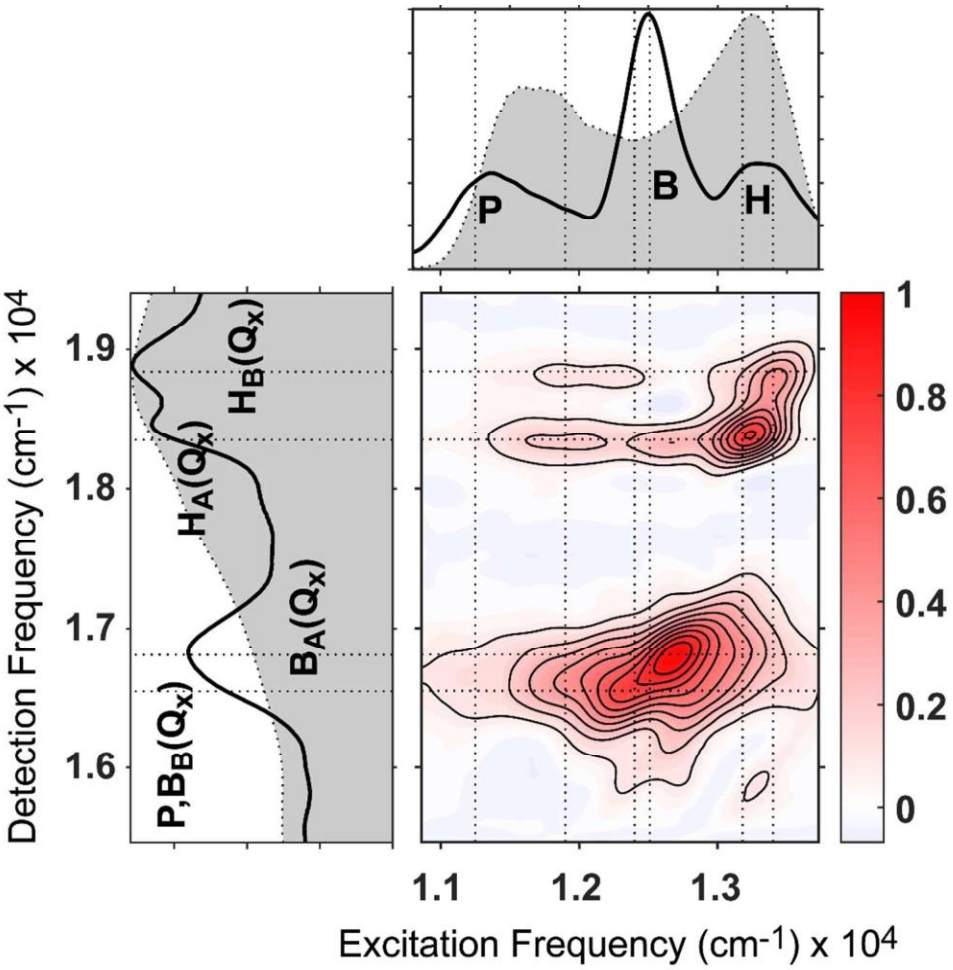

Figure B.1 ESA subtracted 2D absorptive spectrum at T = 10 fs showing the entire excitation and part of detection range along with the 77 K absorption spectrum of W(M250)V highlighting the Q_Y and Q_X transitions. The pump and probe spectrum are plotted as gray area. Dotted lines mark the positions of the excited Q_Y[1] and Q_X[27] states.

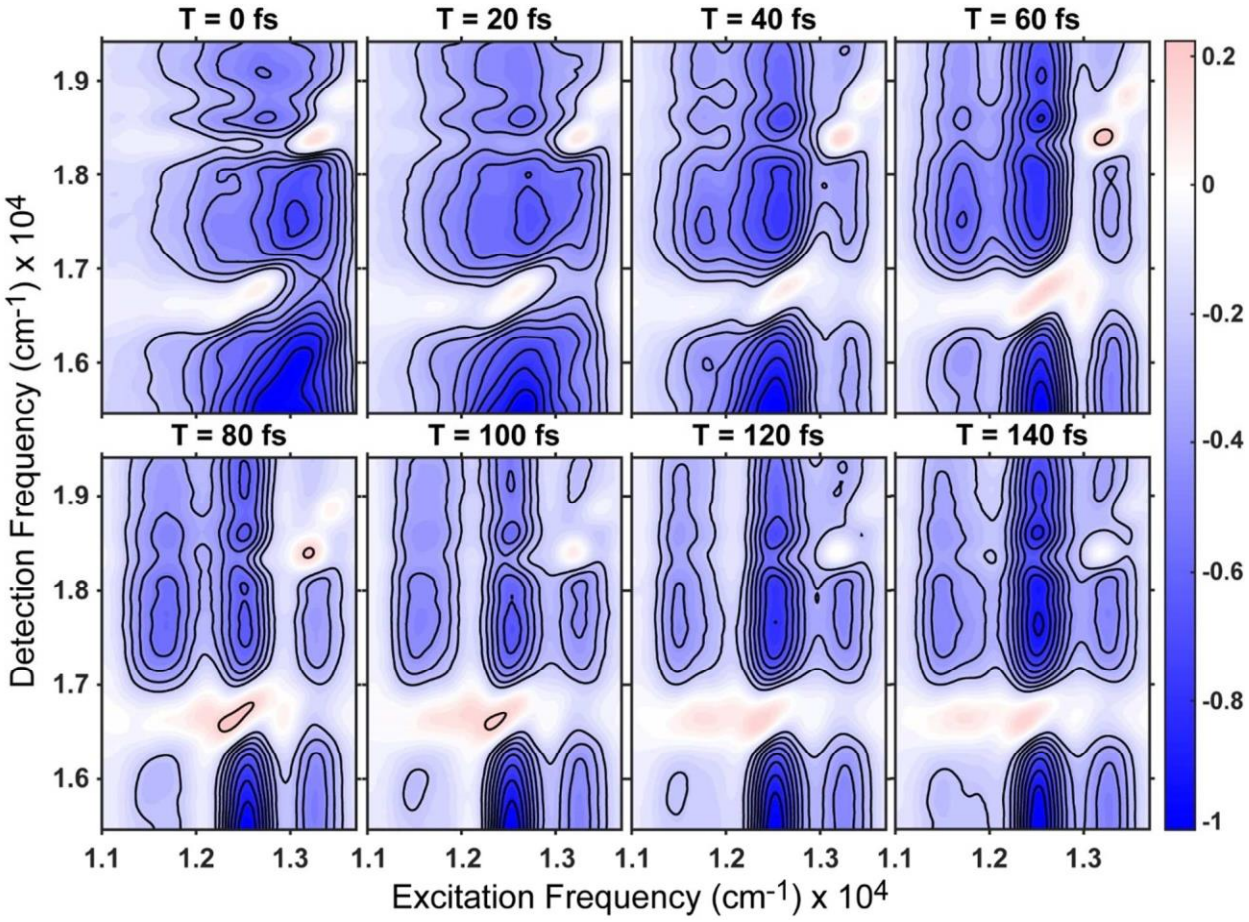

Figure B.2 Raw 2D absorptive spectra for T = 0 to 140 fs in steps of 20 fs showing the strong ESA background (negative signal) overlapped with the weak Q_X GSB (positive) signals. Contours are drawn at 10% intervals starting at 10%.

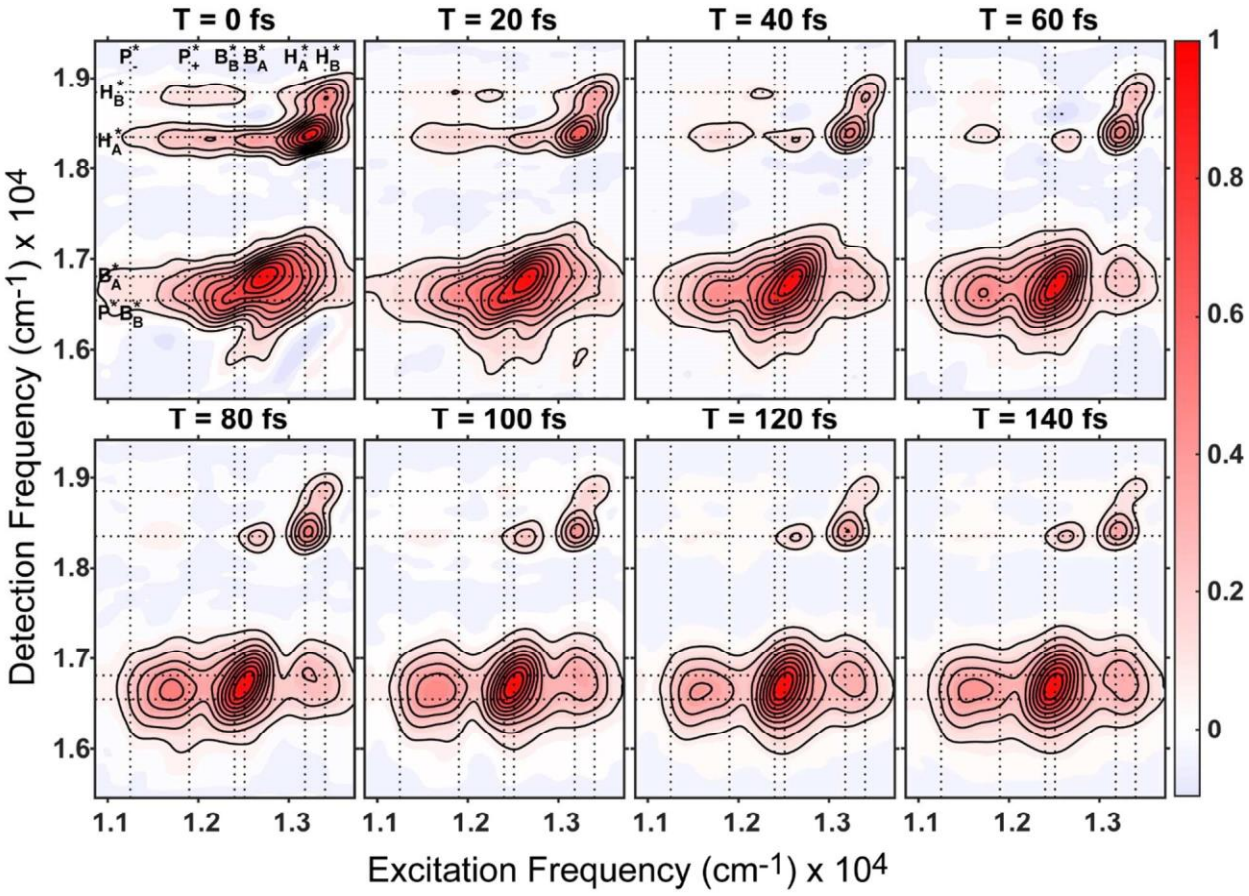

Figure B.3 ESA subtracted 2D absorptive spectra for T = 0 to 140 fs in steps of 20 fs showing Qx GSB signals along with the cross peaks. Contours are drawn at 10% intervals starting at 10%.

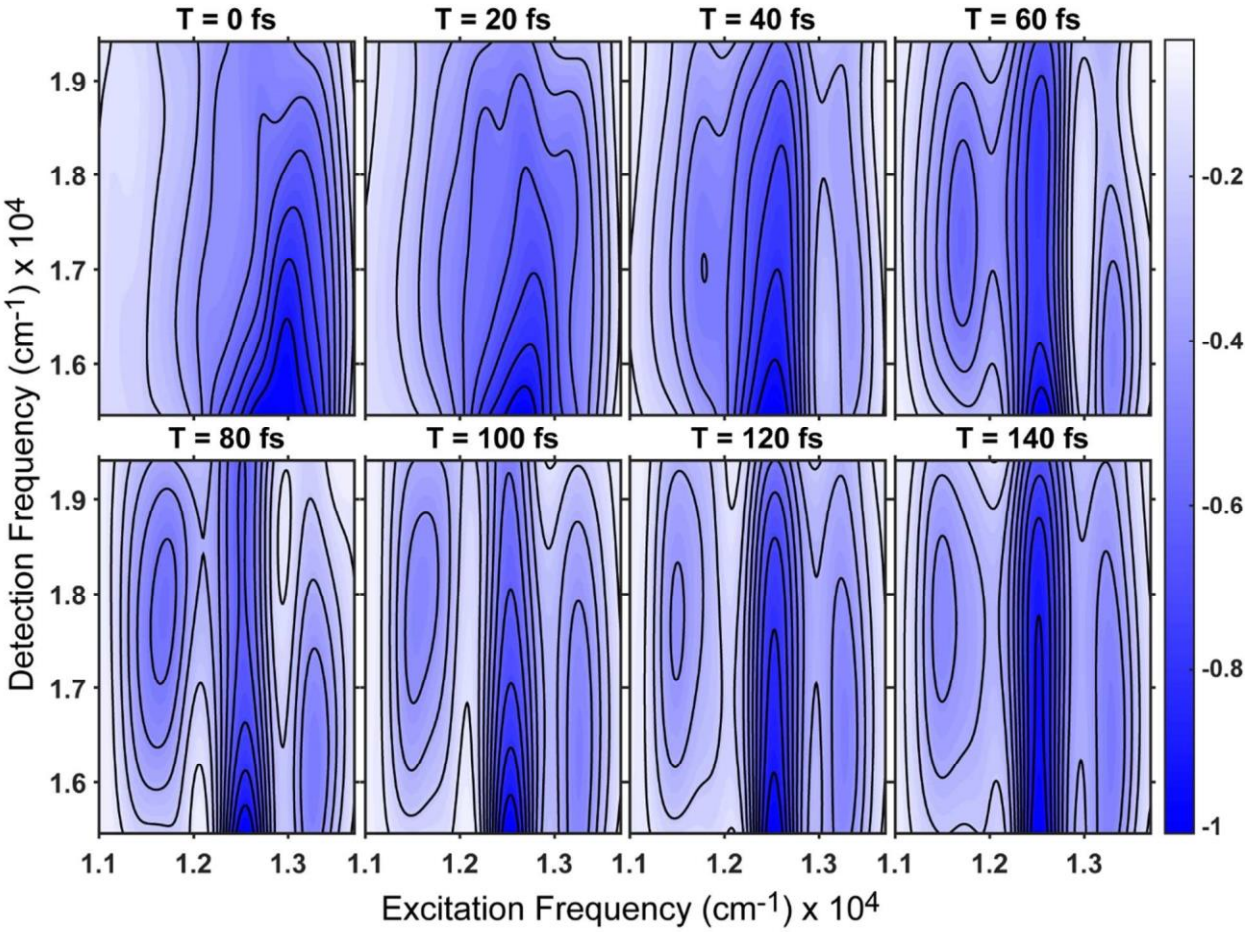

Figure B.4 2D maps constructed using the polynomial fits to the broad ESA background for T = 0 to 140 fs.

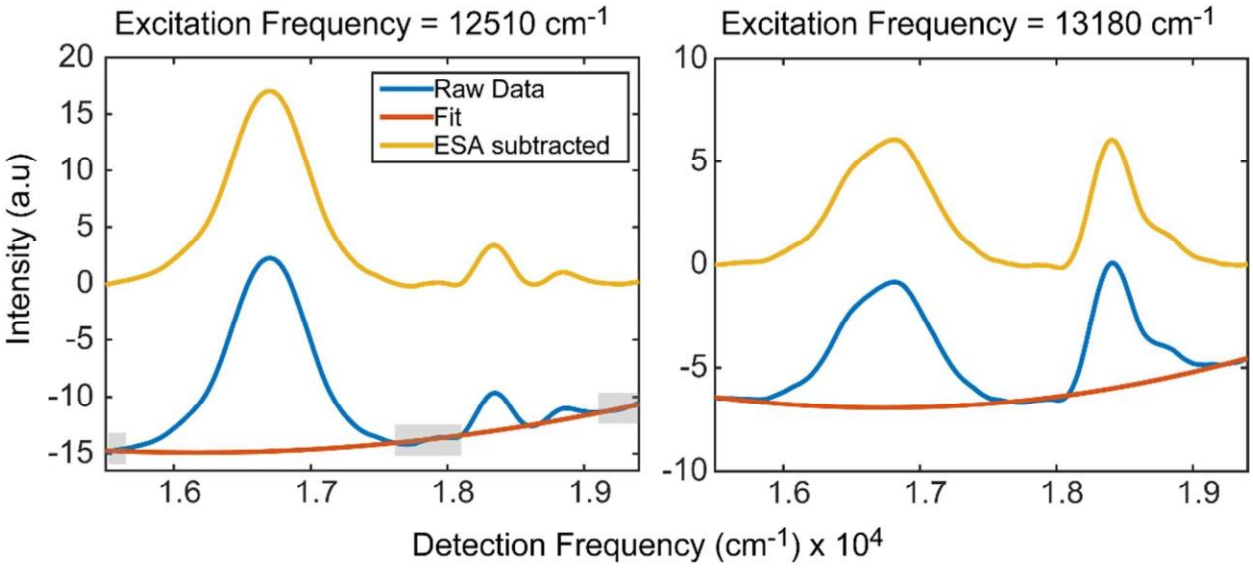

Figure B.5 Slices of the raw absorptive data along the detection axis (blue) shown with the polynomial fit to the background (red) and the subtracted data (yellow) for excitation frequencies corresponding to B^* (left) and H^* (right) at T = 150 fs. The gray boxes denote the frequency regions used to fit to the second order polynomial.

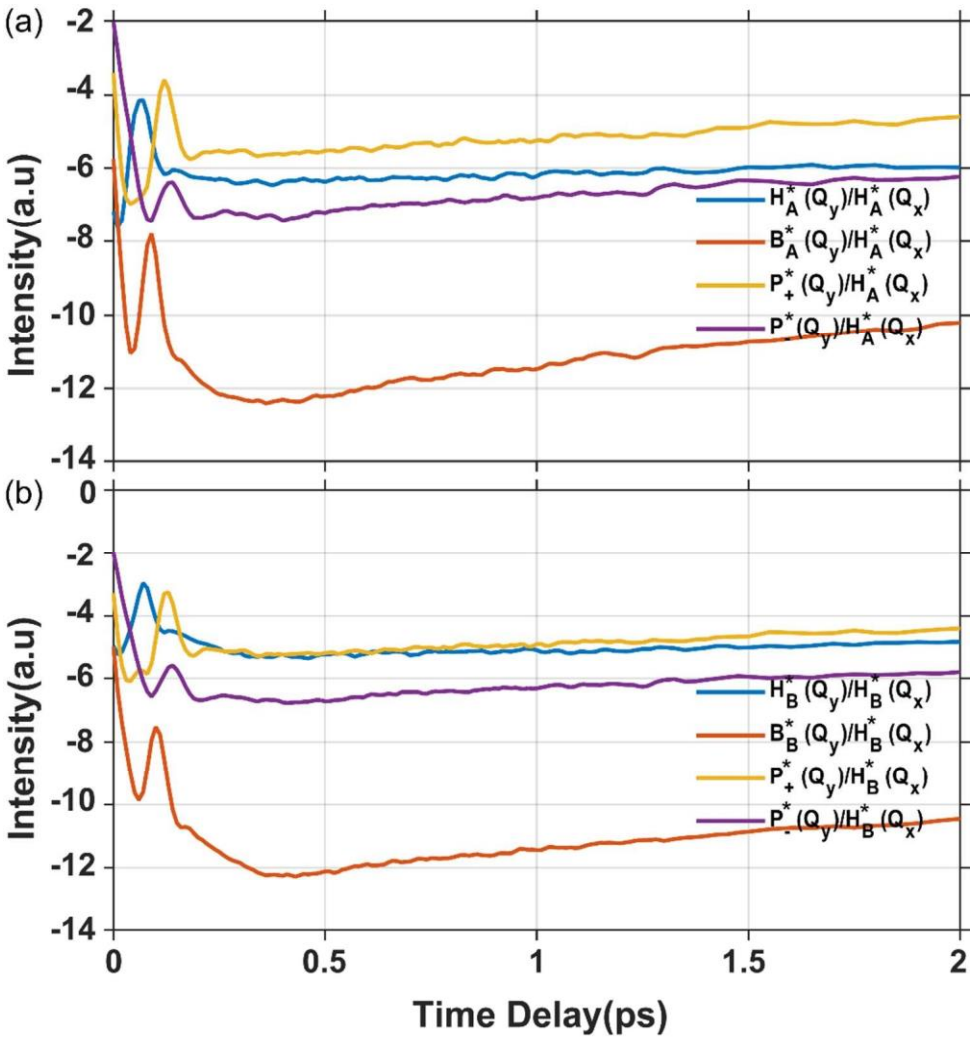

Figure B.6 Kinetic traces constructed from the fit to the ESA background signal corresponding to excitation of the Q_Y transitions of the various excitons while detecting (a) $H^*(Q_X)$ and (b) $H^*(Q_X)$ transitions.

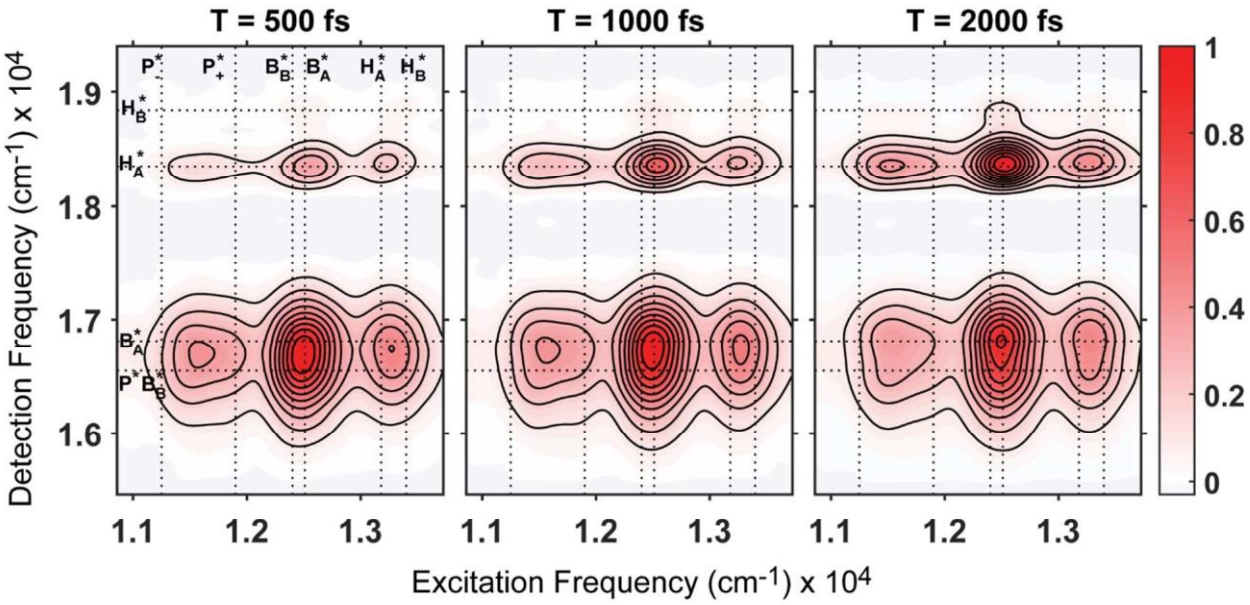

Figure B.7 ESA subtracted 2D absorptive spectra for T = 500, 1000 and 2000 fs showing Q_X GSB signals generated during charge separation. Contours are drawn at 10% intervals starting at 10%.

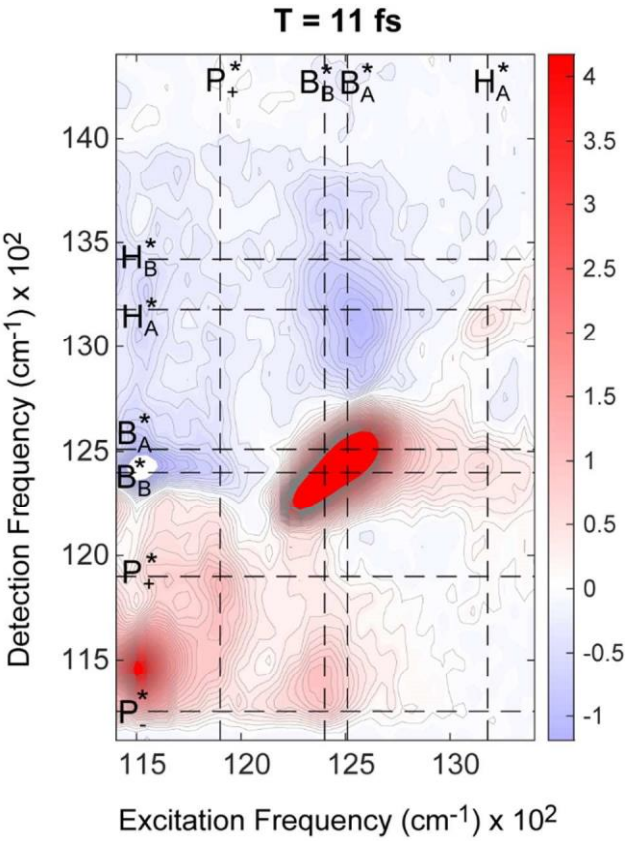

Figure B.8 Real absorptive 2D plot corresponding to Q_Y band excitation and detection at T = 11 fs. Contours are plotted in 1% increments up to 50% to show all minor features. No clear cross peak between H^* and P_+^* or P_-^* is visible. The expected cross-peak locations occur at the intersection of the dotted lines that mark the positions of the excited $Q_Y[1]$ and $Q_X[27]$ states.

Bibliography

[1] A. Niedringhaus *et al.*, "Primary processes in the bacterial reaction center probed by two-dimensional electronic spectroscopy," *PNAS*, vol. 115, no. 14, pp. 3563–3568, 2018, doi: 10.1073/pnas.1721927115.

[2] M. F. Hohmann-Marriott and R. E. Blankenship, "Evolution of photosynthesis," *Annu. Rev. Plant Biol.*, vol. 62, pp. 515–48, 2011, doi: 10.1016/S0167-7306(08)60146-5.

[3] R. E. Blankenship, *Molecular Mechanisms of Photosynthesis*, 2nd ed. St. Louis, Missouri: Wiley Blackwell, 2014.

[4] G. D. Scholes, G. R. Fleming, A. Olaya-Castro, and R. Van Grondelle, "Lessons from nature about solar light harvesting," *Nat. Chem.*, vol. 3, no. 10, pp. 763–774, 2011, doi: 10.1038/nchem.1145.

[5] I. McConnell, G. Li, and G. W. Brudvig, "Energy conversion in natural and artificial photosynthesis," *Chem. Biol.*, vol. 17, no. 5, pp. 434–447, 2010, doi: 10.1016/j.chembiol.2010.05.005.

[6] J. P. Hart, *Evolving the Three Sisters: The Changing Histories of Maize, Bean, and Squash in New York and the Greater Northeast*, New York S. New York: The University of the State of New York, 2008.

[7] T. Mirkovic, E. E. Ostroumov, J. M. Anna, R. Van Grondelle, Govindjee, and G. D. Scholes, "Light absorption and energy transfer in the antenna complexes of photosynthetic organisms," *Chem. Rev.*, vol. 117, no. 2, pp. 249–293, 2017, doi: 10.1021/acs.chemrev.6b00002.

[8] M. K. Şener, J. D. Olsen, C. N. Hunter, and K. Schulten, "Atomic-level structural and functional model of a bacterial photosynthetic membrane vesicle," *Proc. Natl. Acad. Sci. U. S. A.*, vol. 104, no. 40, pp. 15723–15728, 2007, doi: 10.1073/pnas.0706861104.

[9] M. H. B. Stowell, T. M. McPhillips, D. C. Rees, S. M. Soltis, E. Abresch, and G. Feher, "Light-induced structural changes in photosynthetic reaction center: Implications for mechanism of electron-proton transfer," *Science (80-.).*, vol. 276, no. 5313, pp. 812–816, 1997, doi: 10.1126/science.276.5313.812.

[10] M. Gouterman, G. H. Wagnière, and L. C. Snyder, "Spectra of porphyrins. Part II. Four orbital model," *J. Mol. Spectrosc.*, vol. 11, no. 1–6, pp. 108–127, 1963, doi: 10.1016/0022-2852(63)90011-0.

[11] J. R. Reimers, Z. L. Cai, R. Kobayashi, M. Rätsep, A. Freiberg, and E. Krausz, "Assignment of the Q-Bands of the Chlorophylls: Coherence Loss via Q x-Q y Mixing," *Sci. Rep.*, vol. 3, 2013, doi: 10.1038/srep02761.

[12] A. Konar *et al.*, "Electronic Interactions in the Bacterial Reaction Center Revealed by Two-Color 2D Electronic Spectroscopy," *J. Phys. Chem. Lett.*, vol. 9, no. 18, pp. 5219–5225, 2018, doi: 10.1021/acs.jpclett.8b02394.

[13] X. J. Jordanides, G. D. Scholes, and G. R. Fleming, “The Mechanism of Energy Transfer in the Bacterial Photosynthetic Reaction Center,” *J. Phys. Chem. B*, vol. 105, no. 8, pp. 1652–1669, 2001, doi: 10.1021/jp003572e.
[14] J. Breton and A. Vermeglio, *The Photosynthetic Bacterial Reaction Center*. New York: Springer, 1988.
[15] S. R. Meech, A. J. Hoff, and D. A. Wiersma, “Role of charge-transfer states in bacterial photosynthesis,” *Proc. Natl. Acad. Sci. U. S. A.*, vol. 83, no. 24, pp. 9464–9468, 1986, doi: 10.1073/pnas.83.24.9464.
[16] G. Hartwich, H. Scheer, V. Aust, and A. Angerhofer, “Absorption and ADMR studies on bacterial photosynthetic reaction centres with modified pigments,” *BBA - Bioenerg.*, vol. 1230, no. 3, pp. 97–113, 1995, doi: 10.1016/0005-2728(95)00038-K.
[17] O. Rancova, R. Jankowiak, A. Kell, M. Jassas, and D. Abramavicius, “Band Structure of the Rhodobacter sphaeroides Photosynthetic Reaction Center from Low-Temperature Absorption and Hole-Burned Spectra,” *J. Phys. Chem. B*, vol. 120, no. 25, pp. 5601–5616, 2016, doi: 10.1021/acs.jpcb.6b02595.
[18] C. Kirmaier and D. Holten, “Primary photochemistry of reaction centers from the photosynthetic purple bacteria,” *Photosynth. Res.*, vol. 13, no. 3, pp. 225–260, 1987, doi: 10.1007/BF00029401.
[19] W. Zinth and J. Wachtveitl, “The first picoseconds in bacterial photosynthesis - Ultrafast electron transfer for the efficient conversion of light energy,” *ChemPhysChem*, vol. 6, no. 5, pp. 871–880, 2005, doi: 10.1002/cphc.200400458.
[20] L. M. Yoder, A. G. Cole, and R. J. Sension, “Structure and function in the isolated reaction center complex of Photosystem II: Energy and charge transfer dynamics and mechanism,” *Photosynth. Res.*, vol. 72, no. 2, pp. 147–158, 2002, doi: 10.1023/A:1016180616774.
[21] U. Ermler, G. Fritzsch, S. K. Buchanan, and H. Michel, “Structure of the photosynthetic reaction centre from Rhodobacter sphaeroides at 2.65 å resolution: cofactors and protein-cofactor interactions,” *Structure*, vol. 2, no. 10, pp. 925–936, 1994, doi: 10.1016/S0969-2126(94)00094-8.
[22] J. Deisenhofer, O. Epp, K. Miki, R. Huber, and H. Michel, “Structure of the protein subunits in the photosynthetic reaction center of,” *Nature*, vol. 318, no. 6047, pp. 618–624, 1985, [Online]. Available: https://www.nature.com/articles/318618a0.pdf%0Ahttp://www4.utsouthwestern.edu/MichaelyLab/Nature318-618.pdf.
[23] P. D. Laible *et al.*, “Switching sides—Reengineered primary charge separation in the bacterial photosynthetic reaction center,” *Proc. Natl. Acad. Sci. U. S. A.*, vol. 117, no. 2, pp. 865–871, 2020, doi: 10.1073/pnas.1916119117.
[24] P. D. Laible, C. Kirmaier, C. S. M. Udawatte, S. J. Hofman, D. Holten, and D. K. Hanson, “Quinone reduction via secondary B-branch electron transfer in mutant bacterial reaction centers,” *Biochemistry*, vol. 42, no. 6, pp. 1718–1730, 2003, doi: 10.1021/bi026959b.
[25] N. Y. Kiang, J. Siefert, Govindjee, and R. E. Blankenship, “Spectral Signatures of Photosynthesis. I. Review of Earth Organisms.pdf,” *Astrobiology*, vol. 7, no. 1, pp. 222–251, 2007.

[26] M. E. Van Brederode, J. P. Ridge, I. H. M. Van Stokkum, F. Van Mourik, M. R. Jones, and R. Van Grondelle, “On the efficiency of energy transfer and the different pathways of electron transfer in mutant reaction centers of Rhodobacter sphaeroides,” *Photosynth. Res.*, vol. 55, no. 2–3, pp. 141–146, 1998, doi: 10.1023/a:1005925917867.

[27] L. Huang, N. Ponomarenko, G. P. Wiederrecht, and D. M. Tiede, “Cofactor-specific photochemical function resolved by ultrafast spectroscopy in photosynthetic reaction center crystals,” *Proc. Natl. Acad. Sci.*, vol. 109, no. 13, pp. 4851–4856, 2012, doi: 10.1073/pnas.1116862109.

[28] S. Lin, J. Jackson, A. K. W. Taguchi, and N. W. Woodbury, “Excitation Wavelength Dependent Spectral Evolution in Rhodobacter sphaeroides R-26 Reaction Centers at Low Temperatures The Qy Transition Region,” *J. Phys. Chem. B*, vol. 102, pp. 4016–4022, 1998.

[29] M. H. Vos, J. Breton, and J. L. Martin, “Electronic energy transfer within the hexamer cofactor system of bacterial reaction centers,” *J. Phys. Chem. B*, vol. 101, no. 47, pp. 9820–9832, 1997, doi: 10.1021/jp971486h.

[30] H. Zhou and S. G. Boxer, “Probing excited-state electron transfer by resonance stark spectroscopy. 2. Theory and application,” *J. Phys. Chem. B*, vol. 102, no. 45, pp. 9148–9160, 1998, doi: 10.1021/jp982044o.

[31] S. Mukamel, *Principles of Nonlinear Optics and Spectroscopy*. New York: Oxford University Press, 1995.

[32] A. Tokmakoff, “Nonlinear Spectroscopy.” MIT OpenCourseWare, 2009.

[33] P. Hamm, “Principles of Nonlinear Optical Spectroscopy: A Practical Approach.” pp. 1–74, 2005, doi: 10.1021/ja965513d.

[34] D. M. Jonas, “Two-Dimensional Femtosecond Spectroscopy,” *Annu. Rev. Phys. Chem.*, vol. 54, pp. 425–463, 2003, doi: 10.1146/annurev.physchem.54.011002.103907.

[35] K. L. M. Lewis and J. P. Ogilvie, “Probing photosynthetic energy and charge transfer with two-dimensional electronic spectroscopy,” *J. Phys. Chem. Lett.*, vol. 3, no. 4, pp. 503–510, 2012, doi: 10.1021/jz201592v.

[36] F. D. Fuller and J. P. Ogilvie, “Experimental implementations of two-dimensional fourier transform electronic spectroscopy,” *Annu. Rev. Phys. Chem.*, vol. 66, pp. 667–690, 2015, doi: 10.1146/annurev-physchem-040513-103623.

[37] F. D. Fuller, D. E. Wilcox, and J. P. Ogilvie, “Pulse shaping based two-dimensional electronic spectroscopy in a background free geometry,” *Opt. Express*, vol. 22, no. 1, p. 1018, 2014, doi: 10.1364/oe.22.001018.

[38] S. H. Shim, D. B. Strasfeld, Y. L. Ling, and M. T. Zanni, “Automated 2D IR spectroscopy using mid-IR pulse shaping and applications to membrane peptides,” *Opt. InfoBase Conf. Pap.*, vol. 104, no. 36, 2007, doi: 10.1364/ls.2007.lwg2.

[39] J. A. Myers, K. L. M. Lewis, P. F. Tekavec, and J. P. Ogilvie, “Two-color two-dimensional Fourier transform electronic spectroscopy with a pulse-shaper,” *Opt. Express*, vol. 16, no. 22, pp. 17420–17428, 2008, doi: 10.1364/oe.16.017420.

[40] S. M. G. Faeder and D. M. Jonas, “Two-dimensional electronic correlation and relaxation spectra: Theory and model calculations,” *J. Phys. Chem. A*, vol. 103, no. 49, pp. 10489–10505, 1999, doi: 10.1021/jp9925738.

[41] E. M. Grumstrup, S.-H. Shim, M. A. Montgomery, N. H. Damrauer, and M. T. Zanni, “Facile

collection of two-dimensional electronic spectra using femtosecond pulse-shaping Technology," *Opt. Express*, vol. 15, no. 25, p. 16681, 2007, doi: 10.1364/oe.15.016681.
[42] S. H. Shim and M. T. Zanni, "How to turn your pump-probe instrument into a multidimensional spectrometer: 2D IR and Vis spectroscopies via pulse shaping," *Phys. Chem. Chem. Phys.*, vol. 11, no. 5, pp. 748–761, 2009, doi: 10.1039/b813817f.
[43] P. F. Tekavec, J. A. Myers, K. L. M. Lewis, and J. P. Ogilvie, "Two-dimensional electronic spectroscopy with a continuum probe," *Opt. Lett.*, vol. 34, no. 9, p. 1390, 2009, doi: 10.1364/ol.34.001390.
[44] S. S. Senlik, V. R. Policht, and J. P. Ogilvie, "Two-Color Nonlinear Spectroscopy for the Rapid Acquisition of Coherent Dynamics," *J. Phys. Chem. Lett.*, vol. 6, pp. 2413–2420, 2015, doi: 10.1021/acs.jpclett.5b00861.
[45] P. Tyagi *et al.*, "Two-color two-dimensional electronic spectroscopy using dual acousto-optic pulse shapers for complete amplitude, phase, and polarization control of femtosecond laser pulses," *J. Phys. Chem. A*, vol. 117, no. 29, pp. 6264–6269, 2013, doi: 10.1021/jp400603r.
[46] Z. Lin *et al.*, "Modulating unimolecular charge transfer by exciting bridge vibrations," *J. Am. Chem. Soc.*, vol. 131, no. 50, pp. 18060–18062, 2009, doi: 10.1021/ja907041t.
[47] T. L. Courtney, Z. W. Fox, K. M. Slenkamp, and M. Khalil, "Two-dimensional vibrational-electronic spectroscopy," *J. Chem. Phys.*, vol. 143, no. 15, 2015, doi: 10.1063/1.4932983.
[48] M. Delor, I. V. Sazanovich, M. Torie, and J. A. Weinstein, "Probing and exploiting the interplay beteen nuclear and electronic motion in charge transfer processes," *Acc. Chem. Res.*, vol. 48, no. 4, pp. 1131–1139, 2015, doi: 10.1021/ar500420c.
[49] T. A. A. Oliver, N. H. C. Lewis, and R. Graham, "Correlating the motion of electrons and nuclei with two-dimensional electronic–vibrational spectroscopy," *PNAS*, vol. 111, no. 28, pp. 10061–10066, 2014, doi: 10.5452/ma-ax7dd.
[50] T. L. Courtney, Z. W. Fox, L. Estergreen, and M. Khalil, "Measuring Coherently Coupled Intramolecular Vibrational and Charge-Transfer Dynamics with Two-Dimensional Vibrational − Electronic Spectroscopy," *J. Phys. Chem. Lett*, vol. 6, pp. 1286–1292, 2015.
[51] J. D. Gaynor, T. L. Courtney, M. Balasubramanian, and M. Khalil, "Fourier transform two-dimensional electronic-vibrational spectroscopy using an octave-spanning mid-IR probe," *Opt. Lett.*, vol. 41, no. 12, pp. 2895–2898, 2016, doi: 10.1364/UP.2016.UTu4A.7.
[52] V. R. Policht, "Observations of Coherence in Bacterial Reaction Centers Using Two-Dimensional Electronic Spectroscopy," University of Michigan, 2018.
[53] Y. Song *et al.*, "Multispectral multidimensional spectrometer spanning the ultraviolet to the mid-infrared," *Rev. Sci. Instrum.*, vol. 90, no. 1, 2019, doi: 10.1063/1.5055244.
[54] J. Bredenbeck, J. Helbing, and P. Hamm, "Continuous scanning from picoseconds to microseconds in time resolved linear and nonlinear spectroscopy," *Rev. Sci. Instrum.*, vol. 75, no. 11, pp. 4462–4466, 2004, doi: 10.1063/1.1793891.
[55] R. Kania *et al.*, "Investigating the vibrational dynamics of a 17e- metallocarbonyl intermediate using ultrafast two dimensional infrared spectroscopy," *Phys. Chem. Chem. Phys.*, vol. 12, no. 5, pp. 1051–1063, 2010, doi: 10.1039/b919194a.
[56] A. I. Stewart *et al.*, "Structure and vibrational dynamics of model compounds of the [FeFe]-hydrogenase enzyme system via ultrafast two-dimensional infrared spectroscopy," *J. Phys. Chem. B*, vol. 112, no. 32, pp. 10023–10032, 2008, doi:

10.1021/jp803338d.
[57] A. M. Siddiqui, G. Cirmi, D. Brida, G. Cerullo, and F. X. Kärtner, “Generation of sub 7-fs pulses at 800 nm from a degenerate optical parametric amplifier,” *Opt. InfoBase Conf. Pap.*, vol. 34, no. 22, pp. 3592–3594, 2010, doi: 10.1364/cleo.2010.cthz1.
[58] L. P. DeFlores, R. A. Nicodemus, and A. Tokmakoff, “Two-dimensional Fourier transform spectroscopy in the pump-probe geometry,” *Opt. Lett.*, vol. 32, no. 20, p. 2966, 2007, doi: 10.1364/ol.32.002966.
[59] D. E. Wilcox and J. P. Ogilvie, “Comparison of pulse compression methods using only a pulse shaper,” *J. Opt. Soc. Am. B*, vol. 31, no. 7, p. 1544, 2014, doi: 10.1364/josab.31.001544.
[60] P. F. Tekavec, J. A. Myers, K. L. M. Lewis, F. D. Fuller, and J. P. Ogilvie, “Effects of chirp on two-dimensional Fourier transform electronic spectra,” *Opt. Express*, vol. 18, no. 11, p. 11015, 2010, doi: 10.1364/oe.18.011015.
[61] E. Riedle *et al.*, “Generation of 10 to 50 fs pulses tunable through all of the visible and the NIR,” *Appl. Phys. B Lasers Opt.*, vol. 71, no. 3, pp. 457–465, 2000, doi: 10.1007/s003400000351.
[62] M. Kullmann, S. Ruetzel, J. Buback, P. Nuernberger, and T. Brixner, “Reaction dynamics of a molecular switch unveiled by coherent two-dimensional electronic spectroscopy,” *J. Am. Chem. Soc.*, vol. 133, no. 33, pp. 13074–13080, 2011, doi: 10.1021/ja2032037.
[63] K. L. Wells, Z. Zhang, J. R. Rouxel, and H. S. Tan, “Measuring the spectral diffusion of chlorophyll a using two-dimensional electronic spectroscopy,” *J. Phys. Chem. B*, vol. 117, no. 8, pp. 2294–2299, 2013, doi: 10.1021/jp310154y.
[64] N. M. Kearns, R. D. Mehlenbacher, A. C. Jones, and M. T. Zanni, “Broadband 2D electronic spectrometer using white light and pulse shaping: noise and signal evaluation at 1 and 100 kHz,” *Opt. Express*, vol. 25, no. 7, p. 7869, 2017, doi: 10.1364/oe.25.007869.
[65] P. A. Tekavec, K. L. M. Lewis, F. D. Fuller, J. A. Myers, and J. P. Ogilvie, “Toward broad bandwidth 2-d electronic spectroscopy: Correction of chirp from a continuum probe,” *IEEE J. Sel. Top. Quantum Electron.*, vol. 18, no. 1, pp. 210–217, 2012, doi: 10.1109/JSTQE.2011.2109941.
[66] A. P. Spencer, H. Li, S. T. Cundiff, and D. M. Jonas, “Pulse Propagation Effects in Optical 2D Fourier-Transform Spectroscopy: Theory,” *J. Phys. Chem. A*, vol. 119, no. 17, pp. 3936–3960, 2015, doi: 10.1021/acs.jpca.5b00001.
[67] K. Takamura, H. Fischer, and N. R. Morrow, “Physical properties of aqueous glycerol solutions,” *J. Pet. Sci. Eng.*, vol. 98–99, pp. 50–60, 2012, doi: 10.1016/j.petrol.2012.09.003.
[68] M. Polyanskiy, “Refractiveindex.info database,” 2008. https://refractiveindex.info/?shelf=3d&book=crystals&page=ice (accessed Dec. 15, 2020).
[69] P. N. Dominguez *et al.*, “Primary reactions in photosynthetic reaction centers of Rhodobacter sphaeroides - Time constants of the initial electron transfer,” *Chem. Phys. Lett.*, vol. 601, pp. 103–109, 2014, doi: 10.1016/j.cplett.2014.03.085.
[70] J. Zhu, I. H. M. Van Stokkum, L. Paparelli, M. R. Jones, and M. L. Groot, “Early bacteriopheophytin reduction in charge separation in reaction centers of Rhodobacter sphaeroides,” *Biophys. J.*, vol. 104, no. 11, pp. 2493–2502, 2013, doi:

10.1016/j.bpj.2013.04.026.
[71] S. R. Greenfield, M. Seibert, and M. R. Wasielewski, “Direct measurement of the effective rate constant for primary charge separation in isolated photosystem II reaction centers,” *J. Phys. Chem. B*, vol. 101, no. 13, pp. 2251–2255, 1997, doi: 10.1021/jp962982t.
[72] D. C. Arnett, C. C. Moser, P. L. Dutton, and N. F. Scherer, “The first events in photosynthesis: Electronic coupling and energy transfer dynamics in the photosynthetic reaction center from rhodobacter sphaeroides,” *J. Phys. Chem. B*, vol. 103, no. 11, pp. 2014–2032, 1999, doi: 10.1021/jp984464j.
[73] D. Y. Parkinson, H. Lee, and G. R. Fleming, “Measuring electronic coupling in the reaction center of purple photosynthetic bacteria by two-color, three-pulse photon echo peak shift spectroscopy,” *J. Phys. Chem. B*, vol. 111, no. 25, pp. 7449–7456, 2007, doi: 10.1021/jp070029q.
[74] S. Westenhoff *et al.*, “Coherent picosecond exciton dynamics in a photosynthetic reaction center, Supplementary material,” *J. Am. Chem. Soc.*, vol. 134, no. 40, pp. 16484–7, 2012, doi: 10.1021/ja3065478.
[75] D. Paleček, P. Edlund, S. Westenhoff, and D. Zigmantas, “Quantum coherence as a witness of vibronically hot energy transfer in bacterial reaction center,” *Sci. Adv.*, vol. 3, no. 9, 2017, doi: 10.1126/sciadv.1603141.
[76] M. L. Flanagan, P. D. Long, P. D. Dahlberg, B. S. Rolczynski, S. C. Massey, and G. S. Engel, “Mutations to R. sphaeroides Reaction Center Perturb Energy Levels and Vibronic Coupling but Not Observed Energy Transfer Rates,” *J. Phys. Chem. A*, vol. 120, no. 9, pp. 1479–1487, 2016, doi: 10.1021/acs.jpca.5b08366.
[77] G. S. Schlau-Cohen, E. De Re, R. J. Cogdell, and G. R. Fleming, “Determination of excited-state energies and dynamics in the B band of the bacterial reaction center with 2D electronic spectroscopy,” *J. Phys. Chem. Lett.*, vol. 3, no. 17, pp. 2487–2492, 2012, doi: 10.1021/jz300841u.
[78] H. van Amerongen, L. Valkunas, and R. van Grondelle, *Photosynthetic Excitons*. Singapore: World Scientific, 2000.
[79] K. M. Faries *et al.*, “High throughput engineering to revitalize a vestigial electron transfer pathway in bacterial photosynthetic reaction centers,” *J. Biol. Chem.*, vol. 287, no. 11, pp. 8507–8514, 2012, doi: 10.1074/jbc.M111.326447.
[80] M. A. Steffen, K. Lao, and S. G. Boxer, “Dielectric asymmetry in the photosynthetic reaction center,” *Science (80-.).*, vol. 264, pp. 810–816, 1994, doi: 10.1126/science.264.5160.810.
[81] J. Breton and A. Vermeglio, “The photosynthetic bacterial reaction center,” *Biochem. Educ.*, vol. 21, no. 4, p. 222, 1993, doi: 10.1016/0307-4412(93)90111-c.
[82] P. O. J. Scherer and S. F. Fischer, “On the stark effect for bacterial photosynthetic reaction centers,” *Chem. Phys. Lett.*, vol. 131, no. 1–2, pp. 153–159, 1986, doi: 10.1016/0009-2614(86)80534-6.
[83] M. Schröter, M. J. P. Alcocer, R. J. Cogdell, O. Kühn, and D. Zigmantas, “Origin of the Two Bands in the B800 Ring and Their Involvement in the Energy Transfer Network of Allochromatium vinosum,” *J. Phys. Chem. Lett.*, vol. 9, no. 6, pp. 1340–1345, 2018, doi: 10.1021/acs.jpclett.8b00438.
[84] W. Wagner, C. Li, J. Semmlow, and W. S. Warren, “Rapid phase-cycled two-dimensional

optical spectroscopy in fluorescence and transmission mode," *Opt. Express*, vol. 13, no. 10, pp. 3697–3706, 2005, doi: 10.1364/opex.13.003697.

[85] G. A. Lott, A. Perdomo-Ortiz, J. K. Utterback, J. R. Widom, A. Aspuru-Guzik, and A. H. Marcus, "Conformation of self-assembled porphyrin dimers in liposome vesicles by phase-modulation 2D fluorescence spectroscopy," *Proc. Natl. Acad. Sci. USA*, vol. 108, no. 40, pp. 16521–16526, 2011, doi: 10.1073/pnas.1017308108.

[86] K. J. Karki *et al.*, "Unexpectedly large delocalization of the initial excitation in photosynthetic light harvesting," *arXiv*, vol. 2, pp. 1–10, 2018.

[87] V. Tiwari, Y. A. Matutes, A. T. Gardiner, T. L. C. Jansen, R. J. Cogdell, and J. P. Ogilvie, "Spatially-resolved fluorescence-detected two-dimensional electronic spectroscopy probes varying excitonic structure in photosynthetic bacteria," *Nat. Commun.*, vol. 9, no. 1, 2018, doi: 10.1038/s41467-018-06619-x.

[88] E. L. Read *et al.*, "Cross-peak-specific two-dimensional electronic spectroscopy," *Proc. Natl. Acad. Sci. USA*, vol. 104, pp. 14203–14208, 2007.

[89] E. Thyrhaug, K. Žídek, J. Dostál, D. Bína, and D. Zigmantas, "Exciton Structure and Energy Transfer in the Fenna-Matthews-Olson Complex," *J. Phys. Chem. Lett.*, vol. 7, no. 9, pp. 1653–1660, 2016, doi: 10.1021/acs.jpclett.6b00534.

[90] S. I. E. Vulto, S. Neerken, R. J. W. Louwe, M. A. de Baat, J. Amesz, and T. J. Aartsma, "Excited-state structure and dynamics in FMO antenna complexes from photosynthetic green sulfur bacteria," *J. Phys. Chem. B*, vol. 102, no. 51, pp. 10630–10635, 1998, doi: 10.1021/jp983003v.

[91] A. Niedringhaus, "Probing Ultrafast Dynamics of Bacterial Reaction Centers Using Two-Dimensional Electronic Spectroscopy," University of Michigan, 2017.

[92] I. H. M. Van Stokkum, D. S. Larsen, and R. Van Grondelle, "Global and target analysis of time-resolved spectra," *Biochim. Biophys. Acta - Bioenerg.*, vol. 1657, no. 2–3, pp. 82–104, 2004, doi: 10.1016/j.bbabio.2004.04.011.

[93] A. R. Holzwarth and M. G. Müller, "Energetics and kinetics of radical pairs in reaction centers from Rhodobacter sphaeroides. A femtosecond transient absorption study," *Biochemistry*, vol. 35, no. 36, pp. 11820–11831, 1996, doi: 10.1021/bi9607012.

[94] I. H. M. Van Stokkum, L. M. P. Beekman, M. R. Jones, M. E. Van Brederode, and R. Van Grondelle, "Primary electron transfer kinetics in membrane-bound Rhodobacter sphaeroides reaction centers: A global and target analysis," *Biochemistry*, vol. 36, no. 38, pp. 11360–11368, 1997, doi: 10.1021/bi9707943.

[95] A. L. M. Haffa *et al.*, "The dependence of the initial electron-transfer rate on driving force in Rhodobacter sphaeroides reaction centers," *J. Phys. Chem. B*, vol. 106, no. 29, pp. 7376–7384, 2002, doi: 10.1021/jp0257552.

[96] A. Gelzinis *et al.*, "Mapping energy transfer channels in fucoxanthin-chlorophyll protein complex," *Biochim. Biophys. Acta*, vol. 1847, pp. 241–247, 2015.

[97] J. Alster, H. Lokstein, J. Dostál, A. Uchida, and D. Zigmantas, "2D spectroscopy study of water-soluble chlorophyll-binding protein from lepidium virginicum," *J. Phys. Chem. B*, vol. 118, no. 13, pp. 3524–3531, 2014, doi: 10.1021/jp411174t.

[98] F. Milota *et al.*, "Vibronic and vibrational coherences in two-dimensional electronic spectra of supramolecular J-aggregates," *J. Phys. Chem. A*, vol. 117, no. 29, pp. 6007–6014, 2013, doi: 10.1021/jp3119605.

[99] M. Maiuri *et al.*, “Ultra-broadband 2D electronic spectroscopy of carotenoid-bacteriochlorophyll interactions in the LH1 complex of a purple bacterium,” *J. Chem. Phys.*, vol. 142, no. 21, 2015, doi: 10.1063/1.4919056.

[100] E. E. Ostroumov, R. M. Mulvaney, J. M. Anna, R. J. Cogdell, and G. D. Scholes, “Energy transfer pathways in light-harvesting complexes of purple bacteria as revealed by global kinetic analysis of two-dimensional transient spectra,” *J. Phys. Chem. B*, vol. 117, no. 38, pp. 11349–11362, 2013, doi: 10.1021/jp403028x.

[101] F. Ma, E. Romero, M. R. Jones, V. I. Novoderezhkin, and R. van Grondelle, “Both electronic and vibrational coherences are involved in primary electron transfer in bacterial reaction center,” *Nat. Commun.*, vol. 10, no. 1, 2019, doi: 10.1038/s41467-019-08751-8.

[102] J. A. Myers, K. L. M. Lewis, F. D. Fuller, P. F. Tekavec, C. F. Yocum, and J. P. Ogilvie, “Two-dimensional electronic spectroscopy of the D1-D2-cyt b559 photosystem II reaction center complex,” *J. Phys. Chem. Lett.*, vol. 1, no. 19, pp. 2774–2780, 2010, doi: 10.1021/jz100972z.

[103] J. Dostál, B. Benešová, and T. Brixner, “Two-dimensional electronic spectroscopy can fully characterize the population transfer in molecular systems,” *J. Chem. Phys.*, vol. 145, no. 12, 2016, doi: 10.1063/1.4962577.

[104] J. F. Nagle, “Solving complex photocycle kinetics. Theory and direct method,” *Biophys. J.*, vol. 59, no. 2, pp. 476–487, 1991, doi: 10.1016/S0006-3495(91)82241-X.

[105] E. Thyrhaug, K. Žídek, J. Dostál, D. Bína, and D. Zigmantas, “Exciton Structure and Energy Transfer in the Fenna-Matthews-Olson Complex,” *J. Phys. Chem. Lett.*, vol. 7, no. 9, pp. 1653–1660, 2016, doi: 10.1021/acs.jpclett.6b00534.

[106] C. Ruckebusch, M. Sliwa, P. Pernot, A. de Juan, and R. Tauler, “Comprehensive data analysis of femtosecond transient absorption spectra: A review,” *J. Photochem. Photobiol. C Photochem. Rev.*, vol. 13, no. 1, pp. 1–27, 2012, doi: 10.1016/j.jphotochemrev.2011.10.002.

[107] T. Kunsel *et al.*, “Simulating Fluorescence-Detected Two-Dimensional Electronic Spectroscopy of Multichromophoric Systems,” *J. Phys. Chem. B*, vol. 123, no. 2, pp. 394–406, 2019, doi: 10.1021/acs.jpcb.8b10176.

[108] N. P. Pawlowicz, R. Van Grondelle, I. H. M. Van Stokkum, J. Breton, M. R. Jones, and M. L. Groot, “Identification of the first steps in charge separation in bacterial photosynthetic reaction centers of Rhodobacter sphaeroides by ultrafast mid-infrared spectroscopy: Electron transfer and protein dynamics,” *Biophys. J.*, vol. 95, no. 3, pp. 1268–1284, 2008, doi: 10.1529/biophysj.108.130880.

[109] D. Agathangelou, A. Javed, F. Sessa, X. Solinas, M. Joffre, and J. P. Ogilvie, “Phase-Modulated Rapid-Scanning Fluorescence- Detected Two-Dimensional Electronic Spectroscopy,” *arXiv*, pp. 1–24, 2021.

[110] V. Tiwari *et al.*, “Strongly coupled bacteriochlorin dyad studied using phase-modulated fluorescence-detected two-dimensional electronic spectroscopy,” *Opt. Express*, vol. 26, no. 17, p. 22327, 2018, doi: 10.1364/oe.26.022327.